Abstract

A “Spicy” Molecular Mechanism of TRPA1 Hyperactivation Conferred by a Disease Mutant and Insights into C-terminal Regulatory Components

Avnika P Bali

2024

Roughly one third of Americans suffer from chronic pain and inflammation, yet so far little progress has been made to develop new pain remedies beyond non-steroidal anti-inflammatory agents and opioids, which often harbor deleterious side-effects. The identification and mechanistic analysis of pain-initiating receptors in peripheral nociceptor neurons is therefore an attractive approach to develop new analgesic and anti-inflammatory therapeutics. Transient receptor potential (TRP) ion channels are the largest group of receptors expressed in nociceptor neurons and are capable of transducing noxious thermal and chemical stimuli into cation influx that triggers pain signaling. My thesis work focuses on one such TRP channel, TRP “Ankyrin” 1 (TRPA1). In this dissertation, I describe a novel mechanism we uncovered for TRPA1 gain-of-function via a R919* truncation mutation associated with CRAMPT syndrome. Using functional and biochemical assays, we reveal that the R919* mutant co-assembles with WT TRPA1 into functional heteromeric channels. The R919* mutant hyperactivates channels by enhancing their agonist sensitivity and calcium permeability, which could account for the observed neuronal hypersensitivity-hyperexcitability symptoms. This work reveals important structural characteristics of TRPA1, and uncovers how TRPA1 can contribute to disease states in different tissue systems. During my doctoral studies I have also laid the groundwork for determining crucial regulatory processes at the distal disordered C-terminus (DDC), a region of TRPA1 spanning 41 amino acids

that is structurally unresolved and largely overlooked in our field. I find that a cluster of highly conserved acidic residues within the DDC are crucial to TRPA1 activity, plasma membrane trafficking, and Ca^{2+}- mediated regulation. Our lab has identified a novel calmodulin (CaM) binding site within the TRPA1 DDC, and I posit that CaM binding may modulate other conserved residues within the DDC to facilitate functional regulation of TRPA1. In all, the work put forth in this dissertation paves multiple avenues toward unveiling long-sought mechanisms of TRPA1 regulation and illuminating new strategies for treating TRPA1-related pathologies.

A “Spicy” Molecular Mechanism of TRPA1 Hyperactivation Conferred by a Disease Mutant and Insights into C-terminal Regulatory Components

A Dissertation
Presented to the Faculty of the Graduate School
of
Yale University
In Candidacy for the Degree of
Doctor of Philosophy

By
Avnika P. Bali

Dissertation Director: Candice Paulsen

May 2024

Acknowledgement

I am deeply grateful for all of the mentors, colleagues, friends, and family who have shaped my experience in graduate school and supported me through its many challenges.

First and foremost, I must thank Dr. Candice Paulsen for being not only an excellent research advisor, but also a staunch advocate and role model for me and my fellow labmates. I joined Candie's lab when it was only a year old, and from the start Candie welcomed me to the group with open arms. Over the years, I have admired Candie's infectious excitement about science and her firmly optimistic outlook in a field where success is not always immediate or easy. Leading by example, Candie has taught me how to push myself and maximize my own productivity, how to plan experiments efficiently and effectively, and to always focus on the positives throughout the scientific process. I am so grateful to have had Candie's guidance and unwavering support during graduate school, and will aspire to emulate her kind of mentorship toward my own future mentees. I will also take with me many fond memories of Candie and I listening to 2000's punk rock and Broadway classics in lab during the post-COVID shutdown months and our epic Paulsen lab karaoke numbers!

I would also like to thank my thesis committee members Dr. Tony Koleske and Dr. Christian Schlieker for all their advice and scientific feedback throughout my graduate studies. Having Tony and Christian's critical eye on my research projects has undoubtedly strengthened my work and made me a better scientist. I must also express my heartfelt gratitude to my undergraduate mentors at Miami University who were instrumental in getting me to a PhD program at Yale in the first place. In particular, I thank my wonderful undergraduate research advisor Dr. Gary Lorigan and my mentor and "writer / editor extraordinaire" Dr. Paul Urayama for their ongoing encouragement and guidance.

Next, I would like to thank my fellow labmates in the Paulsen lab who made the day-to-day experience of working in a research lab so much more enjoyable and enriching. I must first

shout out Dr. Justin “Colonel” Sanders, who joined the lab a year before me, and has been a constant friend and great colleague over the past 5.5 years. I would also like to thank Dr. Mary Kehinde Taiwo, Camila Garcia, Isabel Romov, and Gregory Quevedo, who have each in their own way brought new energy to our group and make our lab a wonderful environment to work in. I am so deeply grateful our former postgraduate associate Samantha Schaefer, who was not only a vital part of the CRAMPT project but also a wonderful friend. I would also like to thank Alice Zhang, my very first undergraduate mentee, for being an amazing addition to our lab and whose hard work also greatly strengthened the CRAMPT project. I have been lucky to have had many wonderful mentees who have taught me so much about the joys of being a mentor, including KG Montes, Adnan Alladin, Ke Lin, Jae-Hee Bae, and many others. Finally, a huge thanks to Carol Martin for her administrative and technical assistance that helps our lab run smoothly. I’m so proud of and thankful for all the members of our Paulsen lab squad – past and present, for building an inclusive and supportive team atmosphere during my graduate studies.

My PhD experience would have been incomplete without dear friends both in New Haven and in my home state of Ohio. Thank you so much to my OG girl squad Gwendolyn Thomas, Meeta Bharadwaj and Morgan Nguyen for being my besties through college and beyond, and commiserating in the grind that comes with our respective professions. At Yale, one of the most enjoyable experiences I’ve had was getting to be part of the Yale Citations – Yale’s oldest, finest, most attractive, and ONLY graduate and professional school acapella group! Getting to sing with this amazing group of fellow grad students and friends has been an absolute pleasure, and has kept me sane through the twists and turns of graduate research. I will seriously miss being a part of the Citations and will cherish all the friendships I made there. Finally, I owe a huge thank you to my amazing graduate school roommates Claire Cody and Arita Acharya, who made New Haven feel like a home away from home. It is not often that people in grad school choose to live together for 5+ years, and I am so lucky that the 3 of us found each other out of all the other people on that first year Facebook page – I seriously could not have asked for better ‘froomies’!

I must also offer a very special thanks to my partner (in crime!) Andrew Rodriguez, who's love, kindness, and uncanny ability to make me smile even when I'm at my lowest points has made the last 3 years nothing short of magical. Andy has been my rock through some of the most challenging times in graduate school and has generally made me a happier and more contented person. Through Andy I have also been fortunate to know the wonderful Kasicki-Rodriguez family who immediately welcomed me into their lives and have been a second family to me.

And finally, I need to thank my family. To all my extended family in India and abroad - आपके प्यार और आशीर्वाद के लिए आप सभी का बहुत बहुत धन्यवाद. To know that I have a whole entourage of people rooting for me on the other side of the world has always been a comfort to me.

To my maternal grandfather, Nana, thank you for always being a warm and gentle presence throughout my life. I have so many cherished memories of us doing sudokus and crossword puzzles together, and I know now you are watching over me as I grow as a scientist and continue the legacy of solving complex puzzles. To my maternal grandmother, Nani, thank you for showering me in love and unending kindness. I am so happy I've gotten to spend more time with you during my graduate school years, and someday I aspire to match your skill in card games! To my paternal grandparents Amma and Baba – I am eternally grateful to you both for everything you've done for our family, and for making our lives a thousand-fold better by living with us here in the USA. I am so lucky to have grown up with and learned so much from you both. Baba – thank you for being an inspiring example for nourishing one's passions even as one gets older, and for living a life of genuine honesty and loyalty to oneself and to others. To Amma, thank you for always being my steadfast companion in all things fun and lighthearted, for cultivating my love for stories and imagination, and for filling every second of our time together with joy, laughter, and unconditional love. To my "baby" brother Amritesh, thank you for making

my life exponentially more fun and interesting, for bringing a fresh energy and humor to our family, and for always coaxing out my youthful side, no matter how ‘grown up’ I become.

Finally, to my Mom and Dad – thank you for everything. Thank you for bringing out the best in me both as a scientist and as a human being. Dad, thank you for being everything a girl could want in a father. You are my biggest cheerleader, wise counselor, fellow night owl, running buddy, science geek, and foodie companion. I see so many of your traits and personality in the person I have become, and I often feel as though in this whole universe you are the one who truly understands me best. And to my Mom, thank you for being my ultimate role model, and everything I aspire to be. Navigating your career as a woman in STEM in a foreign country while also raising two kids and running the household could not have been easy at all, but for many years I have watched you persist, work hard, and conquer every challenge. Not only do you inspire me, but you are also my closest friend and confidant. I could not have made it this far without having such a strong support system, and I have been truly blessed to have an incredible family and community to give me strength throughout my PhD years and beyond.

Table of Contents

Chapter 1: TRP Channelopathies and their Patho-mechanisms

This chapter is a literature review of functionally characterized TRP channelopathies that have been identified in the human population. An adapted version of this review is in preparation to be submitted in the journal *Channels* (invited).

1.1 Introduction: TRP Channels as Polymodal Sensors and Gatekeepers

In 1969, a defective light sensing phenotype was first discovered in *Drosophila* mutants, and was termed 'transient receptor potential' after the mutants' short duration of response to light[1]. In the late 1980s and 90s, these mutations were traced to the *Trp* gene encoding a photoreceptive cation channel [2,3]. Thus, the field of transient receptor potential (TRP) channel biology was born - homologous channels were subsequently found in various organisms, with 28 mammalian TRP genes identified to date. Recombinant expression of TRP proteins *in vitro*, combined with electrophysiology in heterologous cell types and targeted gene editing in animal models have since allowed us to characterize different mammalian TRP channel properties and contextualize their physiological roles. More recently, the 'resolution revolution' in cryo-electron microscopy (cryo-EM) ushered in a new era in which multiple TRP structures have been solved at atomic resolution, illuminating functional and regulatory mechanisms within these channels.

Mammalian TRP channels fall into six subfamilies based on sequence homology: TRP canonical (TRPC; TRPC1–7), TRP polycystin (TRPP; TRPP2, TRPP3, TRPP5), TRP melastatin (TRPM; TRPM1–8), TRP mucolipin (TRPML; TRPML1–3), TRP vanilloid (TRPV; TRPV1–6), and TRP ankyrin (TRPA; TRPA1). Generally speaking, TRP channels serve as multifunctional cellular sensors capable of polymodal activation. Environmental and endogenous stimuli that directly activate TRP channels include chemical ligands, temperature, pressure, mechanical tension, voltage, and pH[4,5]. Upon activation, TRP channels permeate cations such as Na^+, Ca^{2+}, Mg^{2+}, and K^+. The relative permeability of each cation varies for each TRP channel depending on its

pore properties. On a structural level, TRP channels assemble as tetramers, with each individual TRP protein made up of 6 transmembrane helices, with the 5th and 6th helix helices forming the pore region. Canonically, TRP channels assemble as homotetramers, though many TRPs can assemble with related or even non-TRP channels to form heteromers with distinct functional properties [6]. All TRP channels also have cytoplasmic-facing N- and C-termini that vary in length and contain different structural domains, even amongst subfamily members. These soluble domains include ankyrin repeats, coiled-coils, enzymatic domains, protein partner binding sites, and intrinsically disordered regions. Often the N-and C- termini of TRP channels act as regulatory integrators that can initiate and modulate channel activity.

Mutations in some TRP channel genes have been linked to numerous diseases and disorders in human patients, spanning multiple tissue types and systems within the body (**Figure 1)**. Studying the patho-mechanisms of these channelopathies not only informs therapeutic solutions for patients harboring such mutations, but also provides valuable insight into critical components of channel function and reveals physiological pathways in which these channels participate. In this section, I summarize and describe reported TRP channelopathies (e.g. mutations in channel genes directly linked to disease pathogenesis), and their proposed molecular and cellular patho-mechanisms. Our focus will be on mutations that have been functionally characterized. While only a subset of TRP family members have associated channelopathies, most *Trp* genes have natural variants and polymorphisms which pose an increased risk of certain diseases but are not singlehandedly responsible for disease phenotypes. Details on risk factors related to TRP channels can be found in other reviews and publications [7,8].

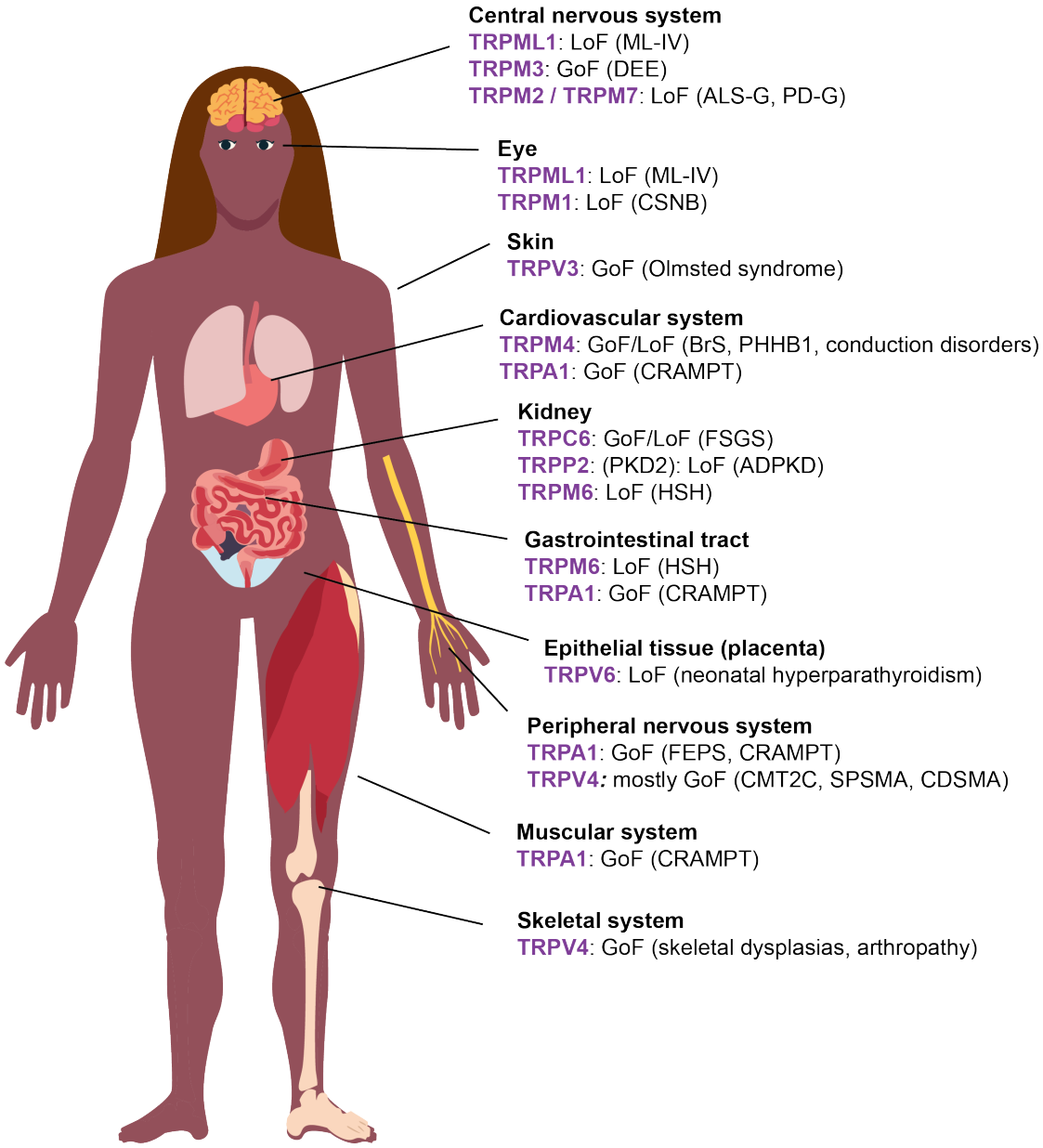

Figure 1: Known channelopathic mutations of TRP channels and their affected tissues. Functional effects of mutations designated as gain-of-function (GoF) or loss-of-function (LoF). Specific channelopathies associated with each channel are listed in parentheses. See text for abbreviations

1.2 TRP Channelopathies

i. TRPCs:

The TRPC channel family is made up of 7 members: TRPC1-7, each with differing expression profiles throughout the body. Contrary to other mammalian species, TRPC2 is a pseudogene in humans, and is therefore not expressed. The remaining TRPCs are classified into the following distinct subfamilies based on sequence homology and functional similarities: TRPC1, TRPC4/5, and TRPC3/6/7 [9]. Members within the TRPC family are known to form heterotetramers [10,11], which can additionally determine their role in physiological processes. Each member of the TRPC family is activated downstream from receptors in the PLC-pathway through complex and distinct mechanisms. Endogenous activators and/or regulators of TRPCs include diacylglycerols (DAG), IP3 receptors, intracellular Ca^{2+}, STIM1, and PIP2 [10,11,12,13,14] .

TRPC6: The most well-studied channelopathic mutations within the TRPC family have been identified in TRPC6. These mutations underlie focal and segmental glomerulosclerosis (FSGS), a disease characterized by impairment or loss of podocyte function in the kidneys, leading to proteinuria (leakage of proteins into the urine) and ultimately progressing to end-stage kidney disease. Multiple TRPC6 mutations have been identified in cases of autosomal dominant, mostly adult-onset, FSGS. The first of these was in 2005 identifying a missense mutation P112Q as the underlying cause of FSGS in a large New Zealand family[15]. This mutant channel exhibited enhanced plasma membrane localization compared to WT, as well as larger calcium influx upon direct activation with DAG and indirect stimulation with Angiotensin II, a known player in the progression of renal disease. Subsequently, a screen of 71 family pedigrees with hereditary FSGS revealed new heterozygous mutations with distinct functional profiles (N143S, S270T, K874*, R895C and E897K)[16], hinting at multiple viable molecular mechanisms for TRPC6-driven renal pathology. Since these initial studies, over 25 FSGS-associated TRPC6 mutations have been reported. The majority of these mutations cause gain of function via distinct mechanisms, such as increasing basal channel activity (ie: G109S, N110H, Q889K, R895C, and E897K) [17],

enhancing calcium influx upon activation (N143S, H218L and A404V, Q134P) [17-19], delaying calcium inactivation (M132T, S270T and K874*) [20,21], and increasing plasma membrane localization (R68W and P112Q) [15,22].

Thus far, missense channel mutations are located exclusively on the cytoplasmic face of the channel, clustering at either the N-terminal ankyrin-repeat domain, or at conserved C-terminal motifs (**Figure 2A**). Cryo-EM studies of the cytoplasmic domain of TRPC6 show that for some N-terminal point mutations, disruption of inter-subunit interactions are a likely cause for abnormal channel function (**Figure 2B**). Structures also reveal a tight and cytosol-inaccessible interface between the N-terminal ankyrin repeats and the vertical C-terminal coiled-coil (**Figure 2C**). This interaction site is a hotspot of FSGS mutations (P112Q, G109S, N110H, M132T, Q134P, R175Q/W, and N143S on ankyrin repeat domains (ARDs) 1 and 2 and Q889K, R895L/C, and E897K on the C-terminal coiled-coil), suggesting that these mutations intrinsically perturb dynamics between AR1 and the coiled coil leading to altered gating of the channel [23]. Recent structures of TRPC6 solved in high-calcium states reveal that these mutations may also reduce the structural packing at cytosolic calcium binding sites, disrupting the ability of calcium to inhibit channel activity [24].

The link between TRPC6 dysfunction and FSGS pathogenesis is not fully clear. From early studies, TRPC6 within kidney podocytes localizes to the cell body, major processes and the foot processes, which form the sieve-like slit diaphragm responsible for filtration [16]. One widely accepted mechanism is that hyperactivation of TRPC6 leads to Ca^{2+} overload, injury and apoptosis of podocytes, and eventually to proteinuria[25,26]. Consistent with this hypothesis, larger increases to channel currents lead to more aggressive phenotypes [20]. However, loss-of-function TRPC6 mutations have also been linked to FSGS, indicating that some basal level of TRPC6 activity is required for normal renal function, and thus either hypo- or hyper-activation of TRPC6 can have severe consequences. Notably, patients with LoF mutations in TRPC6 have remarkably early onset of FSGS (0-7 years old), whereas most patients with GoF mutations first present

symptoms in adolescence or early adulthood [17]. TRPC6 is also expressed in a variety of non-renal tissues, including the brain, heart, lung, ovary, and vasculature which are not grossly affected by TRPC6 mutations, suggesting a more complex patho-mechanism involving other podocyte-specific protein partners. For instance, TRPC6 is known to directly interact with podocyte slit diaphragm proteins nephrin and podocin, which not only modulate its activity [27,28] but also induce actin cytoskeleton reorganization and altered podocyte morphology, which may go awry in disease states [29]. Importantly, nephrin, which generally suppresses TRPC6 activity, exhibits decreased binding to FSGS TRPC6 mutants P112Q, N143S, S270T, R895C, and E897K[27]. Other in vitro studies demonstrate activation of calcineurin-NFAT signaling pathway downstream of hyperactive TRPC6 mutants when WT is co-expressed to mimic the heterozygous genotype in patients[30-32], which may also promote actin reorganization in podocytes and reduce their glomerular filter barrier function.

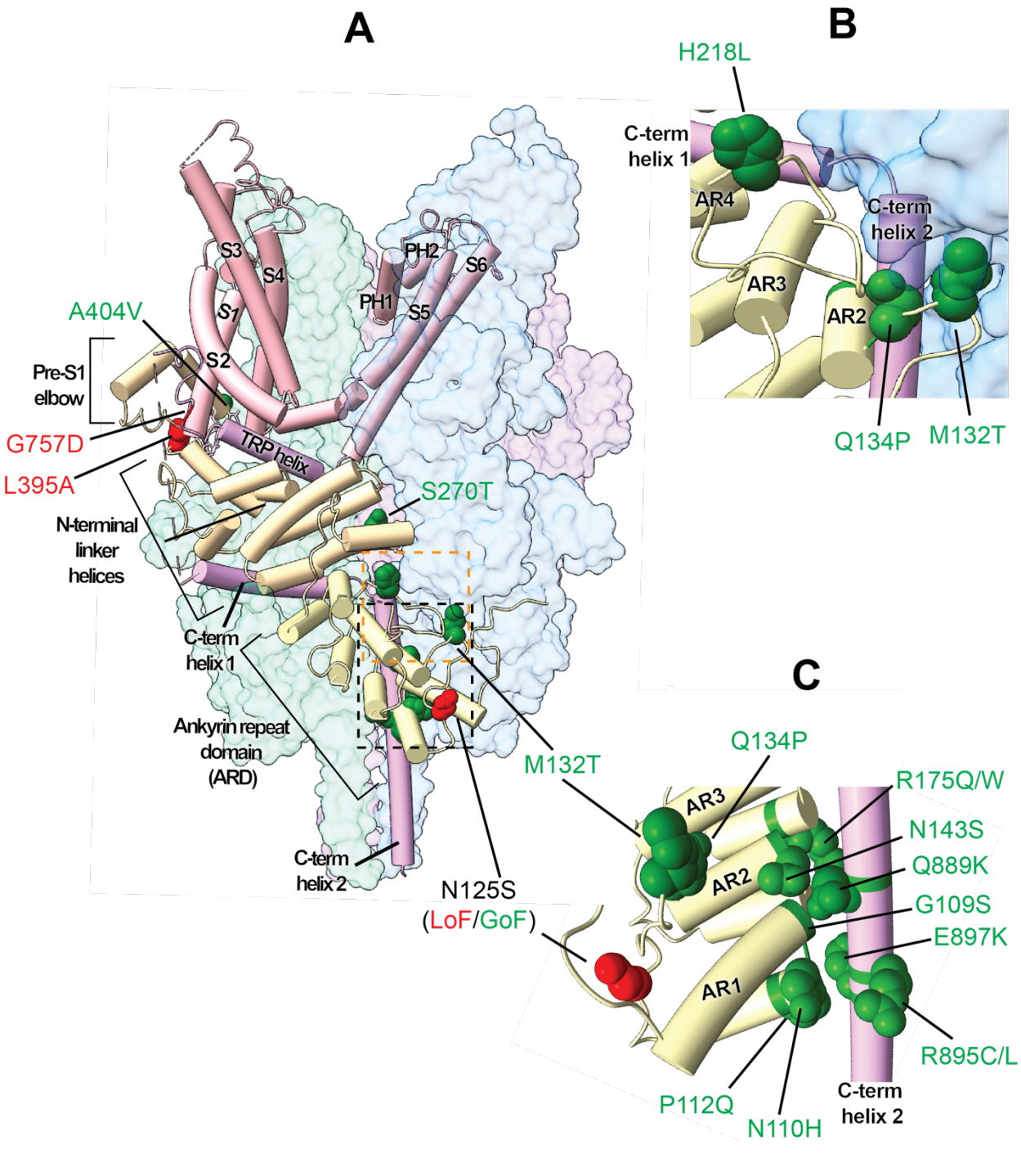

Figure 2: Mutations causing FSGS mapped onto TRPC6 cryo-EM structure (PDB: 6UX8). A: TRPC6 full tetramer with monomer tube helices colored and structural domains and disease mutations labeled (GoF= green and LoF = red). Surface densities of neighboring 3 subunits indicated in green blue, and purple. **B:** Zoom-in of orange dotted box in A - mutated residues with putative inter-subunit interactions (adjacent subunit surface density in blue) **C:** Zoom-in and 90° rotated view of black dotted box in A - ARD and C-terminal helix interface

ii. TRPPs:

The TRPP ("polycystin") subfamily consists of three members: TRPP2, TRPP3, and TRPP5 (often referred to by their gene names PKD2, PKD2L1 and PKD2L2, respectively), all of which exhibit the structural hallmarks of TRP channels: six transmembrane segments, cation-permeable pore between S5 and S6. Earlier studies have also grouped the TRPPs with non-TRP channels including the large, multidomain ion channel PKD1 and related channels PKD1L13 and PKDREJ into a larger "polycystin" family of gene products underlying polycystic kidney disease. To date, not much is known about endogenous activators of TRPPs, and in vitro experiments suggest they are generally constitutively active[33,34].

TRPP2 (PKD2): The founding member of the TRPPs, TRPP2 (hereby called PKD2 for contextual clarity), was first discovered through genetic studies of Autosomal Dominant Polycystic Kidney Disease (ADPKD). ADPKD is the most common hereditary kidney disease, occurring in 1:800-1:1000 individuals[35]. The main clinical manifestation of ADPKD is progressive development of large renal cysts, ultimately leading to chronic renal failure in approximately 50% of affected individuals. Beyond the kidneys, cysts can also form in the pancreas and liver with high incidence of hypertension, intracranial aneurysms, and inflammation in other organs [36]. The involvement of multiple organ systems in ADPKD suggests it is a systemic disorder, and is consistent with the widespread tissue expression of PKD2 and other polycystin proteins[37]

ADPKD is primarily caused by a mutation in either PKD2 (~15%) or PKD1 (~80%) [38], and often requires an additional ("second hit") acquired mutation in one of these genes. Mutations of the PKD1 gene are typically associated with earlier onset of renal failure and more severe clinical presentation[39]. Otherwise, PKD1 and PKD2 mutations produce virtually identical disease manifestations, indicating that the two proteins function in concert within a common signaling pathway. The majority of PKD2 mutations linked to ADPKD are thought to be loss-of-function due to truncations or insertion/deletion [40]. A small group of mutations are missense (~5%) and tend to cluster strongly within the extracellular TOP domain and transmembrane helices. Functional

studies on these missense mutations reveal mainly loss-of-function[41] due to local conformational changes, trafficking defects, and destabilization of channel assembly. An interesting exception was found in 2009 by Miyagi et al. This study identified a frameshift mutation (697fsX) causing the addition of 17 abnormal residues after E697 followed by premature termination [42]. Interestingly, 697fsX PKD2 exhibited a unique ability to interact with TRPC3 and TRPC7, and displayed distinct trafficking to the plasma membrane rather than the ER retention observed in WT PKD2. At the plasma membrane, these TRPC3/7-PKD2 complexes showed unique biophysical channel properties, including enhanced single channel conductance, eventually leading to enhanced receptor-activated Ca^{2+} influx, presumably leading to mild ADPKD (**Figure 3B**).

Understanding the pathogenic mechanism of PKD2 loss of function is made complicated by its functional versatility and its unique ability to heteromerize with ion channels outside its subfamily. While PKD2 does form constitutively active homotetrameric ER-resident channels permeable to Ca^{2+}, it can also assemble into functionally distinct hetero-channels with PKD1, which are present at the plasma membrane and the ciliary membrane [43,44]. Importantly, this heteromerization is disrupted in some cases of ADPKD [45]. Recently, the structure of the PKD1-PKD2 receptor-ion channel complex was solved, revealing a 1:3 stoichiometry and domain-swapped heterotetrameric architecture [46]. Though this structure lacked flexible N-and C-termini, mapping a handful of ADPKD-causing point mutations to this structure suggests incorrect folding and trafficking of the PKD1-PKD2 complex as a likely cause of disease pathogenesis, as opposed to disrupted channel gating and activity. Indeed, numerous studies have underscored the importance of PKD2 trafficking in disease pathogenesis [47], since PKD2 participates in distinct signaling pathways at multiple subcellular locations (**Figure 3**). PKD2 can localize to the ER, the plasma membrane, as well as the primary cilium depending on its interacting partners. Mutations in PKD2 can thus negatively impact Ca^{2+} homeostasis by changing the subcellular localization or

perturbing interactions between PKD2 and other ion channels to which it directly binds or oligomerizes [42,48].

The cellular and tissue-wide consequences of PKD2 dysfunction are still being elucidated (**Figure 3B**). The prevailing model is that cysts in the renal tubes form as a result of increased proliferation of epithelial cells. Prior studies have linked PKD2 haploinsufficiency and LoF mutations to faster cell proliferation, and that PKD1 and PKD2 together induce antiproliferative effects in cells[49-51]. Additionally, PKD2 plays an important role in ciliary function. Studies have shown that both the PKD1-PDK2 and TRPV4-PDK2 complexes are mechanosensitive in primary cilia, allowing flow-mediated bending of the cilia to trigger Ca^{2+} influx [52]. Loss of this flow-dependent calcium signal in the cilia can ultimately lead to defects in planar cell polarity, presumably via Wnt signaling [53], though this mechanism is still poorly understood. The resulting inability of renal cells to orient themselves along polar axes could contribute to cystogenesis.

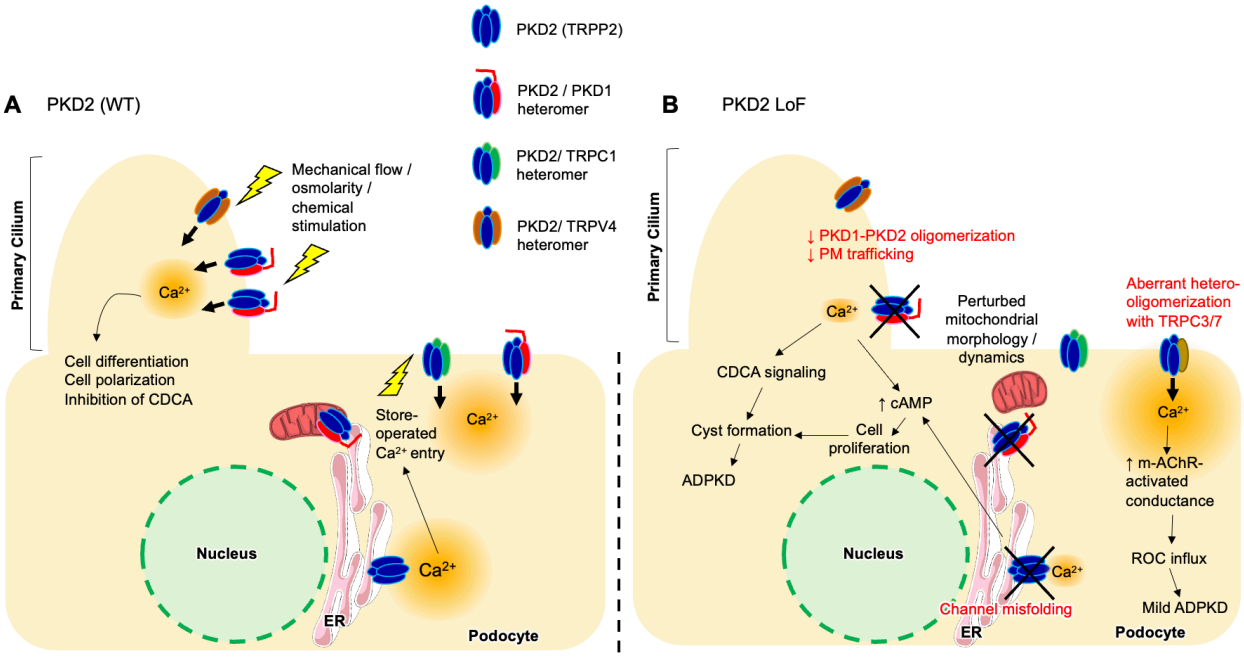

Figure 3: Putative pathways to ADPKD through PKD2 loss-of-function
A: PKD2 function in WT background. PKD2 homotetramers localize intracellularly at the ER, where they constitutively release Ca^{2+}. PKD2 also forms heteromeric channels with other TRP family members and PKD2 at the cell surface or ciliary membrane, where it plays a vital role in kidney cell homeostasis.
B: PKD2 in disease conditions. ADPKD mutations result in various modes of PKD2 loss-of-function (red), leading to altered Ca^{2+} influx patterns and pathogenic signaling pathways, ultimately resulting in cyst formation. CDCA = cilia-dependent cyst activation

iii. TRPMs:

The TRPM ("melastatin") channel family is comprised of 8 members (1-8). All TRPM channel subunits contain 4 melastatin homology regions and a pre-S1 homology region at the N-terminus, which collectively form a pocket structure that has been implicated in agonist sensing and channel assembly [54]. Significant sequence variability among TRPM subfamily members is observed in the C-terminus. Based on sequence homology of the C-terminal coiled-coil domains, TRPM channels are classified into 4 groups: TRPM1/3, TRPM2/8, TRPM4/5, and TRPM6/7 [55]. Each member of the TRPM subfamily exhibits its own unique expression profile [56] and ion conductivity, thus resulting in a diversity of TRPM-related diseases.

TRPM1: The founding member of the TRPM subfamily, TRPM1, was first discovered as regulator of pigmentation in melanocytes, that also functioned as a tumor suppressor (thus named "melastatin", as its expression is downregulated in malignant melanomas) [57]. Around a decade later, multiple groups reported TRPM1 expression in retinal bipolar cells, and its crucial role in driving glutamate receptor-coupled depolarization of ON-bipolar cells in response to light[58,59]. Indeed, channelopathic mutations in TRPM1 were identified as the cause of congenital stationary night blindness (CSNB) first in Appaloosa horses and then later in human patients [60,61]. CSNB is characterized by impaired vision in night or dim lighting, prolonged dark adaptation, and general decreased visual acuity. A key feature in CSNB diagnosis is the selective loss of "b-waves" in electroretinograms (ERG), indicating absent or defective response of ON-bipolar cells in the retina[60,61]. Interestingly, CSNB patients with TRPM1 mutations generally exhibit no severe pigmentation or melanocyte abnormalities [62].

More than 100 disease-associated TRPM1 variants have been identified, which range from missense, nonsense, frameshift, and splice-site mutations to copy number variants (e.g. complete loss of gene) [63]. Generally speaking, most of TRPM1 disease mutations are considered loss-of-function mutations given that patient ERGs and phenotypes match those of TRPM1-null animal models [60,61,64]. The ON visual pathway is initiated by a light-induced reduction of presynaptic glutamate at ON-bipolar cells, which deactivates the mGluR6 signaling pathway. This results in more TRPM1 activity and thus cell depolarization. Studies suggest that mGluR6-coupled gating of TRPM1 is mediated by direct agonism of inactive G_o and dual antagonism of active G_o components $G\boldsymbol{\alpha}_O$ and $G\boldsymbol{\beta\gamma}$ [59]. It follows that any pathogenic TRPM1 loss-of-function via nonfunctional mutations, mislocalization, copy number loss, etc would prevent propagation of low-light photosensation to the retinal ganglion, causing CSNB.

While TRPM1 loss of function is the likely cause of CSNB, how these mutations impair channel function is not fully studied. Single point mutations notably tend to cluster at soluble domains of TRPM1, implying distinct molecular mechanism for loss of function than more drastic

truncation, frameshift, or splice variants[65]. Nakamura et al characterized the effect of two missense mutations R624C (N-terminal) and F1075S (C-terminal) in electroporated mouse bipolar cells and found reduced localization at the ON bipolar cell dendritic tip, indicating the importance of these regions for proper trafficking [66]. Very few of the identified TRPM1 disease mutations have been functionally characterized in heterologous overexpression systems, in part because TRPM1 does not inherently localize to the plasma membrane without other ON-bipolar cell proteins, such as GRM6 and NYX[65,67] .

Importantly, several pathogenic mutations reside in non-coding regions of TRPM1 that are thought to impact splicing, thus potentially skewing isoform expression to produce a novel pathogenic effect [63,66]. The TRPM1 gene undergoes extensive alternative splicing, yielding several endogenous isoforms. Some of these isoforms are capable of forming functional channels, while others form shorter polypeptides overlapping with cytoplasmic domains [68,69]. Co-expression of full-length and a short N-terminal TRPM1 isoform in HEK293 cells showed lower calcium influx, indicating a physical interaction between the two isoforms suppresses channel activity [70], shedding light on the possibility of channel regulation via splice variants.

TRPM3: TRPM3 was identified in 2003 by a bioinformatics genome search [71] and has since been shown to be widely expressed throughout the body including nociceptive neurons, brain, kidney, reproductive organs, retinal pigmented epithelium, and pancreatic beta cells[71-73]. In these tissues, TRPM3 displays activation in response to heat as well as the endogenous steroid pregnenolone sulfate (PS) [74], though the physiological consequences are not fully elucidated for all tissue types. Within the TRP family, the *Trpm3* gene encodes the largest number of isoforms, increasing its functional complexity. Spliced TRPM3 protein products have been shown to interfere with functional isoforms to attenuate TRPM3 channel activity [75], or can function as full channels, but with altered ion selectivity [76].

The first pathogenic mutation in TRPM3 was identified by Bennett et al in 2014, where a novel heterozygous missense TRPM3 mutation was linked to inherited pediatric cataract and

high-tension glaucoma [77]. The mutation results in a substitution of a conserved isoleucine to methionine, which can then function as a novel translation start-site that competes with endogenous start-sites. The predicted result is an 89-amino acid extension of the N-terminus in lens isoforms of TRPM3 [77]. This mutation, when expressed in a 'knock-in' mouse line, produces the same early-onset cataract phenotype observed in humans[78]. Intriguingly, neither heterozygous nor homozygous Trpm3-null mice showed signs of cataract, indicating that the aberrant start-site TRPM3 protein product could actually facilitate a novel gain-of-function mechanism underlying disease. Indeed, increased cytoplasmic Ca^{2+} in the lens due to a ROS- and/or mechano- sensitive nonselective cation current is strongly implicated in cataract formation and lens aging [79]. TRPM3 activation could explain this current, as it is also known to regulate Ca^{2+} dynamics in various other eye tissues [80,81]. While direct functional characterizations of this disease mutation have not yet been performed, these studies have the potential to unravel a fascinating and distinct isoform-mediated TRP channel patho-mechanism in the human lens.

More recently, missense TRPM3 mutations have been associated with epilepsy and intellectual disorders. Little is known about TRPM3 function in the brain, making these newly discovered channelopathies an important area of study. All currently identified mutations that have been functionally characterized exhibit a gain-of-function phenotype[82-84]. The first missense mutations were identified in 8 probands with developmental and epileptic encephalopathy (DEE) [85]: a Val to Met substitution in the S4-S5 loop and a Pro to Gln substitution in the S6 pore loop (numbering varies between splice variants). Biophysical characterization of both mutants revealed high basal current, with increased pregnenolone sulphate and heat sensitivity compared to WT even in co-expression conditions mimicking the heterozygous genotype[83]. In particular, the Val to Met mutant also displays delayed Ca^{2+}-induced desensitization, as well as significant inwardly rectifying current [84]. This rectification change has been hypothesized to signify ion flux through an alternative pore formed by the voltage-sensor domains, which may gate when a substituted Met residue breaks the hydrophobic packing in the S4 helix; albeit, there is currently

no direct structural evidence that such a permeation pathway exists [84,86]. On the other hand, the Pro to Gln mutant displays more pronounced heat activation [83]. In existing structures, the proline residue in TRPM3 sits at the top of the S6 helix, where it is surrounded by cholesterol-like lipid densities. Cholesterol is reportedly a negative modulator TRPM3 [87] and perhaps the Pro to Gln substitution perturbs the effect of these regulatory lipids on channel gating.

Since then, an additional 8 novel missense mutations have been identified, most of which exhibit elevated basal Ca^{2+} influx the heterozygous background [82]. These point mutations seemingly cluster at cytosol-transmembrane interface regions in or proximal to the S4-S5 linker, suggesting gating perturbations as the likely cause of GoF. However, despite several detailed studies of TRPM3 mutant channel properties, there are many unanswered questions. While cranial MRIs of some DEE patient brains show signs of cerebellar atrophy, the specific brain regions and cell types affected by toxic GoF of TRPM3 have not yet been identified, nor have genetic animal models been developed to test pathophysiological mechanisms of DEE. These future studies will be key to understanding the role of TRPM3 in the brain.

TRPM4: TRPM4, like its close relative TRPM5, exhibits a notably higher permeation of monovalent cations such as Na^+ and K^+ than divalent cations. TRPM4 is known to express in a multitude of tissues, including (but not limited to) the heart, bladder and colon smooth muscle cells, the central nervous system, and immune cells[88-90]. Though it is impermeable to Ca^{2+}, TRPM4 is yet activated by intracellular Ca^{2+}, driving membrane depolarization and, consequently, enhanced Ca^{2+} influx via Ca^{2+}-permeable channels [91]. Physiologically, this means TRMP4 permeates depolarizing Na^+ at negative membrane potentials and mediates a repolarizing K^+ efflux at positive potentials.

In human pathology, both GoF and LoF TRPM4 mutations have been linked to cardiac disorders such as Brugada syndrome [92,93], progressive familial heart block type IB [94,95], atrio-ventricular and right bundle branch block [96], and other conduction disorders[97-99]. These mutations are scattered throughout the channel, but tend to spare transmembrane helices. However, why

both GoF and LoF mutations underlie similar conduction defects, and why the mutations specifically affect cardiac tissues is still under study.

Multiple lines of evidence implicate protein expression, localization, and turnover in TRPM4 disease etiology. The first characterized channelopathic mutation was identified in 2009 by Kruse et al, and was a heterozygous missense mutation (E7K) exhibiting normal biophysical channel properties, but an attenuated posttranslational deSUMOlyation[95]. The result was impaired endocytosis of TRPM4, leading to elevated plasma membrane localization and apparent channel gain-of-function. Other GoF TRPM4 mutations were subsequently identified that exhibited more channel stabilization at the cell surface[94,100]. Bianchi et al expanded on these findings with novel LoF and GoF TRPM4 conduction block mutants showing that differential protein turnover of mutants underlies GoF (stable, long half-life) and LoF (increased degradation)[97]. A unique exception was the A432T mutant, investigated by Xian et al using UV-flash Ca^{2+} uncaging to mimic rapid, dynamic changes in intracellular Ca^{2+} in cardiac cells. In their study, A324T variant displays slower Ca^{2+} deactivation kinetics than does WT TRPM4 [101], leading to a progressive increase in current over repeated stimulations.

It has been proposed that both GoF and LoF TRPM4 mutations can convergently cause slowing of cardiac conduction by interfering with components of action potential generation in the heart. TRPM4 GoF may enhance cell depolarization and thus increase the population of inactivated voltage-gated sodium (NaV1.5) channels to cause abnormal signaling, while LoF could induce a hyperpolarization of the membrane potential, reducing cellular excitability and signal propagation[88,99]. However, direct evidence of these hypothesized roles for TRPM4 remains elusive. While atrioventricular conduction block phenotypes can be re-capitulated in TRPM4-/- mouse models, it is not observed in WT-overexpression models, though these mice do exhibit increased ventricular arrhythmias [102]. Moreover, neither mouse knock-out or overexpression studies reveal specific modification of resting potentials or sodium currents, necessitating further study of TRPM4 pathophysiology in the human heart.

Interestingly, a recent study reported two novel TRPM4 mutations linked to progressive symmetric erythrokeratodermia (PSEK), a skin cornification disorder with no apparent cardiac symptoms or arrhythmias [103]. These missense mutations, I1033M and I1040T, were located in the S6 transmembrane helix directly within the ion permeation pathway of the pore[104]. Patch clamp analysis revealed enhanced channel activity at resting potentials as well as increased sensitivity to Ca^{2+} activation, with no alterations in channel trafficking. Thus, unlike most cardiac disease mutations, PSEK mutations exclusively alter intrinsic channel properties. The authors thus posit that increased expression of normally functioning channels in excitable cells leads to cardiac conduction diseases, while intrinsic channel hyperactivity in non-excitable keratinocytes underlies skin disorders, indicating potential tissue-specific pathways for TRPM4 disease.

TRPM2/TRPM7: TRPM2 and TRPM7, while belonging to different TRPM subgroups, are both "chanzymes", meaning that they function as ion channels while also possessing an enzymatic domain at the C-terminus [105]. Both have the ability to permeate monovalent and divalent cations, though TRPM7 seems to predominantly favor Ca^{2+} and Mg^{2+} permeation [106]. TRPM2 responds to reactive oxygen species to permeate Ca^{2+}. TRPM7 is constitutively active, but its activity can be suppressed by intracellular free Mg^{2+}.

In the mid-20th century, studies revealed an estimated 50-100 fold higher incidence rate of two distinct but related neurological disorders in Western Pacific populations: Gauminian amytrophic lateral sclerosis (ALS-G) and parkinsonism dementia (PD-G)[107]. Both disorders have overlapping symptoms and frequently occur together in the same families and even the same patient, and are thus considered to have the same pathogenic mechanism [108]. Indeed, Hermosura et al first linked the disorders to a heterozygous TRPM7 mutation in 2005, and then to a heterozygous TRPM2 mutation in 2008[108,109] . The first TRPM7 missense mutation T1482I, lies on the intracellular C-terminus of the channel in a serine/threonine rich region preceding the αkinase domain. Functional characterization revealed a higher sensitivity of the mutant to Mg^{2+} inhibition, where much lower concentrations of Mg^{2+} could suppress channel currents compared

to WT [109]. T1482 also appears to be an autophosphorylation site[109,110], thus revealing a novel role of autophosphorylated residues in Mg^{2+} inhibition. On the other hand, the TRPM2 missense mutation, P1018L, is located in the extracellular pore-forming loop just preceding the S6 transmembrane helix[111,112]. This mutation, which is predicted to increase conformational flexibility of the pore loop, functionally reduces ROS-evoked calcium influx due to more rapid inactivation compared to WT in physiological conditions. In contrast to TRPM7, the TRPM2 mutant inactivation is not Mg^{2+}-dependent. Both mutants, therefore, seem to result in less divalent cation translocation across the plasma membrane, but via distinct mechanisms.

Given these results, the etiology of ALS-G and PD-G is now believed to be a complex mix of both genetic and environmental factors. The Western Pacific has severely low levels of Ca^{2+} and Mg^{2+} in the soil, drinking water, and food supply. Animals fed diets mimicking the environmental levels in these areas show altered Ca^{2+} homeostasis and neuronal damage, and PD patients exhibit lower local Mg^{2+} concentrations strongly correlated with disease severity [113,114]. Thus, the TRPM2 and TRPM7 mutations, which decrease Ca^{2+} and Mg^{2+} influx into the cell, are thought to predispose individuals to harmful effects imposed by their specific environment. How these ion channels contribute to disease pathology is still under investigation. TRPM7 loss of function in ALS-G/PD-G patients is consistent with more recent studies showing that reduced TRPM7 expression and activity causes cell death in dopaminergic neurons of the substantia nigra, which is a hallmark of PD [115,116]. Evidence also points to ROS production as a key player in ALS and PD pathogenesis, where destabilization of Ca^{2+} and Mg^{2+} homeostasis may trigger mitochondrial dysfunction. TRPM2 is activated by ROS, and thus plays a vital role in mediating ROS-induced Ca^{2+} signaling. The role of Ca^{2+} influx via TRPM2 in the brain is still disputed, though recent evidence from cancer studies suggests it has a protective role against apoptosis [117], and its inhibition is deleterious to cell survival. Taken together, it is conceivable that TRPM2 and/or TRPM7 loss of function, in combination with environmentally-imposed ion

imbalances, underlie dysregulation of Ca^{2+} and Mg^{2+} homeostasis and ROS-mediated cell death, ultimately leading to neurodegeneration in key brain regions in ALS and PD.

TRPM6: TRPM6 is closely related with TRPM7, and thus also predominantly permeates Ca^{2+} and Mg^{2+}. Due to their structural similarities, TRPM6 and TRPM7 can form 2:2 heteromeric channels, which have distinct pore architecture, pH sensitivity, and conductance compared to their homomeric counterparts [106]. However, while TRPM7 is expressed ubiquitously, TRPM6 is expressed quite specifically in the kidney, small intestine, and colon [118].

In 2002, Schlingmann et al identified mutations in TRMP6 underlying autosomal recessive hypomagnesemia with secondary hypocalcemia (HSH), making it the first identified TRPM channelopathy [119] . HSH usually appears shortly after birth and is characterized by very low serum Mg^{2+} levels, leading to neuromuscular excitability and generalized convulsions. When diagnosed early, symptoms can be managed via intravenous and/or oral administration of Mg^{2+} and Ca^{2+}, but do not recover to normal levels.

Since then, many more mutations have been identified, which lead to stop, frame-shift, and splice site mutations that lack key structural regions for channel activity[120,121]. Some missense mutations at conserved residues have also been reported, all of which cause drastic loss of function, likely due to intrinsic changes in channel function rather than a trafficking deficiency [122]. Importantly, HSH occurs when mutations are homozygous, as serum Mg^{2+} levels are normal in heterozygous parents of affected individuals [122]. This differs from mouse studies, where TRM6+/- mice exhibit mild hypomagesemia and TRPM-/- mice do not even survive gestation, indicating that humans may have compensatory mechanisms for TRPM6 loss that are not present in mice.[123]. Thus, the disease model for HSH is TRPM6 loss of function at colon and distal convoluted tubule (DCT) epithelia. This in turn causes reduced uptake of Mg^{2+} in the intestine and kidney and renal wasting of Mg^{2+}, resulting in low Mg^{2+} serum levels [124].

iv. TRPMLs:

The “mucolipin” or TRPML / MCOLN subfamily of TRP channels comprises 3 members in mammalian genomes: TRPML1, TRPML2, and TRPML3. Structurally, TRPMLs differ from other TRPs mostly in the soluble loop between the 1st and 2nd transmembrane helix. All of these are found to largely localize within the intracellular endolysosomal system. This includes early and late endosomes, recycling endosomes and lysosomes - necessitating modified endolysosomal electrophysiology approaches to functionally study these channels.

TRPML1: TRPML1 is ubiquitously expressed across tissue types and is highly active in physiological lysosomal conditions (acidic luminal pH and PI(3,5)P2-rich membranes)[125-127].

In 2000, mutations in the MCOLN1 gene encoding TRPML1 were first identified as the cause of Mucolipidosis type IV (ML-IV)[128-131]. ML-IV is a recessive lysosomal storage disorder characterized by neurodegeneration, mental and motor impairment, corneal clouding, and elevated blood gastrin, ultimately leading to a shortened lifespan[132]. The majority of patients harboring these mutations are of Ashkenazi Jewish descent (70-80% of total cases) due to a high frequency of heterozygous carriers (~1:100)[133,134]. On the cellular level, hallmarks of ML-IV are enlarged late endosomes and lysosomes (LELs) and the accumulation of glycosphingolipids, cholesterols, and glycosaminoglycans within cells, as well as impaired autophagy. All currently identified mutations are thought to be loss-of-function. The most common mutation is a splice site variant IVS3-2A→G, resulting in skipping of exon 4-5 and subsequent loss of the reading frame, and the second is a drastic 6434-bp deletion which skips exons 1-6, and part of exon 7 [135]. The remainder of cases are caused by ~20 independent mutations, which range in disease severity depending on the degree of functional loss of protein [136].

In order for lysosomes to properly degrade macromolecules, they must traffic towards appropriate cargo-carrying vesicles and then undergo membrane fusion or fission. TRPML1 is thought to be the primary Ca^{2+} channel in LELs, and thus increases local juxta-organellar Ca^{2+} levels, which is important for membrane fusion events such as autophagic vesicle-lysosome fusion and lysosomal exocytosis. Indeed, *Drosophila* lacking TRPML1 exhibit “fusion-clamped”

lysosomes and LE/autophagosomes, in which vesicles are docked but are unable to undergo fusion [137]. This in turn leads to reduced degradation of endocytosed and autophagic material, consistent with accumulation of autophagosomes and ubiquitinated proteins observed in ML-IV patients [138]. TRPML1-mediated Ca^{2+} release has also been shown to induce transcriptional activity of TFEB, a master regulator which activates lysosomal biogenesis and autophagic genes [139]. Recently, a TFEB-independent pathway was also reported in which acute TRPML1 activity releases Ca^{2+} from lysosomes, activating calcium/calmodulin-dependent protein kinase kinase β (CaMKKβ) and AMP-activated protein kinase (AMPK), which induces the Beclin1/VPS34 autophagic complex and generates phosphatidylinositol 3-phosphate (PI3P) - culminating in the biogenesis of autophagic vesicles which must then fuse with lysosomes in a TRPML1-dependent manner [140]. TRPML1 activity also drives Ca^{2+}-dependent trafficking of lysosomes toward the autophagosome-rich perinuclear region during autophagy, and acts in concert with PI(3,5)P2 and ALG2 and dynein to facilitate lysosome tubulation and reformation [141]. Thus, TRPML1 likely plays a role in multiple lysosomal degradation and autophagy pathways, making its loss-of-function detrimental on both a cellular and systems level.

v. T*RPVs:*

Channels within the TRPV ("vanilloid") family are widely expressed in both neuronal and non-neuronal cell types. The TRPV family is made up of members TRPV1-6, which are further divided into the TRPV1-4 and TRP5/6 subgroups based on their functional properties [142]. Within the TRPV1-4 subgroup, channels can form homo- or hetero-tetrameric channels with mild calcium selectivity. On the other hand, TRPs 5/6 are highly calcium selective [143]. Of these, pathological variants have been described for TRPV3, TRPV4, and most recently for TRPV6.

TRPV3: TRPV3 is widely expressed in multiple tissue types, especially in epithelial tissues, including keratinocytes. TRPV3 is activated by innocuous thermal stimulation in the 30-40°C range, as well as some endogenous chemical ligands. Proper function of TRPV3 is vital for

keratinocyte maturation, skin barrier formation, wound healing, temperature sensation and itch [144,145].

In 2006, two independent point mutations were identified in rodent TRPV3 underlying the autosomal dominant hairless phenotype and spontaneous atopic dermatitis [146]. Both mutations featured a substitution of G573 in TRPV3 (Gly-> Ser in mice and Gly->Cys in rats). Functional characterization studies revealed both mutants are constitutively active at basal conditions [147]. Interestingly, while the mutant channels themselves exhibit high basal activity, they are unresponsive to thermal and chemical stimuli. On the other hand, when mutant and WT TRPV3 channels are co-expressed to recapitulate the genotype of hairless rodent keratinocytes, the channels exhibit reduced temperature threshold as well as enhanced responses to heat and TRPV3 ligands. Under physiological conditions, the hyperactivity imposed by mutant TRPV3 causes cell death due to imbalances in ion homeostasis, thereby underlying the hairless phenotype in rodents.

By 2012, TRPV3 mutations were found in human patients with Olmsted syndrome (OS), a rare autosomal dominant keratosis [148]. OS is classified by palmoplantar keratoderma (PPK), which describes an abnormal thickening of skin at the palms of the hands or soles of the feet, as well as periorificial keratotic plaques and a host of other symptoms that may vary from patient to patient. Notably, of the six patients in the study, 5 of them exhibited the very same de novo heterozygous point mutations previously identified in the hairless rodents - Gly573Ser (4 individuals), and Gly573Cys (1 individual). Additionally, a novel mutation, Trp692Gly, was identified in one individual. Whole-cell and inside-out patch clamp recordings of transiently transfected HEK293 cells revealed that much like in the hairless rodent mutants, all 3 human mutants were constitutively active, exhibiting large inward currents even without agonist. However, the effect of co-expression with WT TRPV3 was not tested, nor was any characterization made of response to temperature. Notably, thermosensation was normal in all affected individuals, even on affected areas, and no other sensory or neurological symptoms were

observed. In terms of disease patho-mechanism, it is primarily believed that much like the hairless rodents, gain-of-function mutations in human patients induce varying degrees of Ca^{2+}-overload, leading to keratinocyte apoptosis causing OS symptoms.

Since these foundational studies, additional human TRPV3 gain of-function point mutations have been linked to OS [149-151]. When mapped to the TRPV3 structure, these mutations cluster around S2-S3, S4-S5, the pore domain, and the TRP domain (**Figure 4**). Some mutations are located near the domain-swap interfaces between the pore domain and voltage-sensing domain [152,153]. Based on comparisons of TRPV3 structures solved in distinct functional states, regions carrying high abundance of OS mutations – such as S4-S5 linker, S6, and the TRP helix undergo major conformational rearrangements during gating to facilitate opening of the channel [153]. Thus, the location of the mutated residues supports alteration of channel gating leading to constitutive activity of the channel.

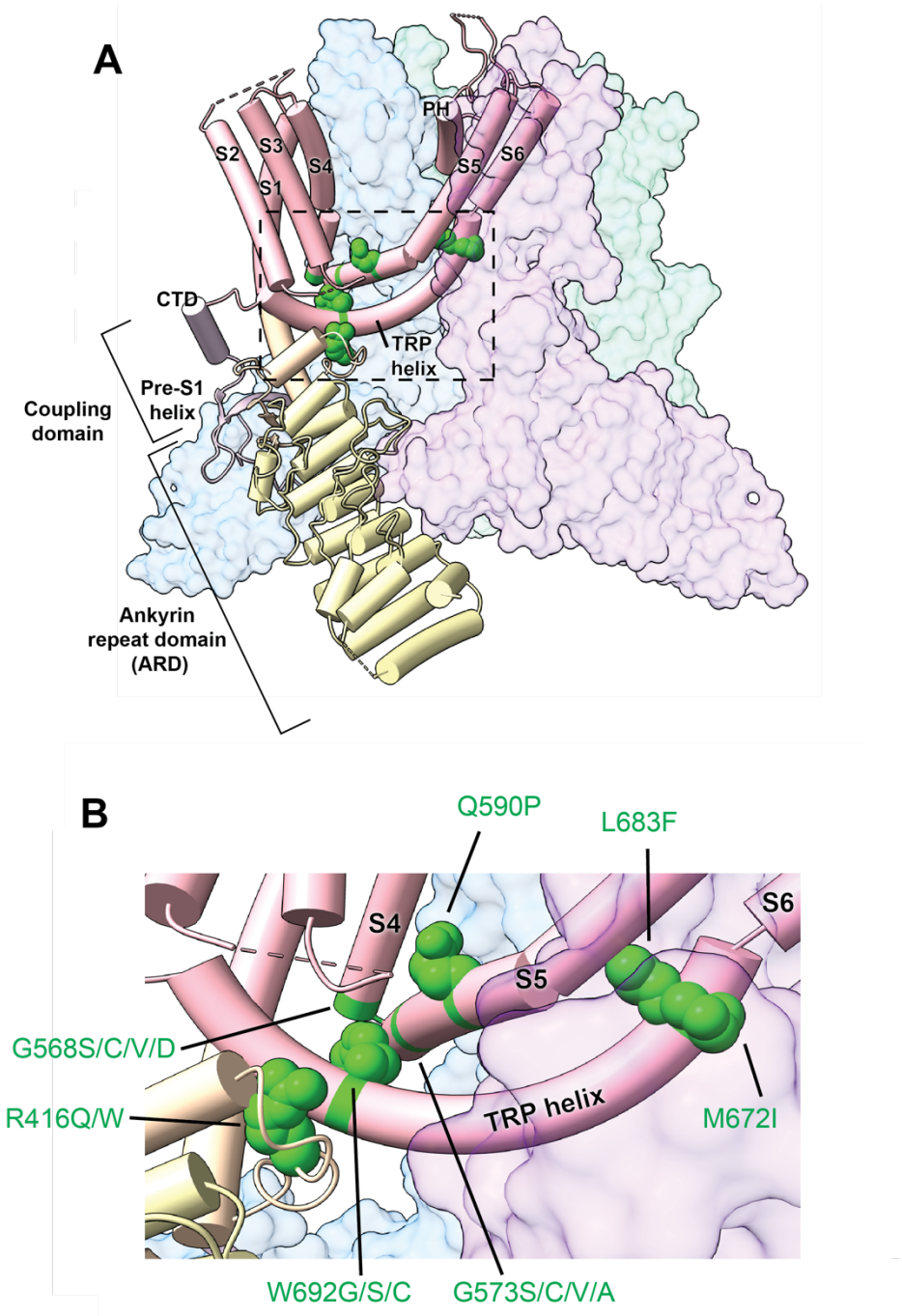

Figure 4: Olmsted Syndrome missense mutations mapped onto Cryo-EM structure (PDB: 7XJ3)
A: TRPV3 full tetramer with a single monomer tube helices colored and structural domains indicated. GoF mutation sites are indicated as ball-and-sticks.
B: Zoom-in of pore-proximal region (dotted box in A); Individual GoF mutations labeled

TRPV4: Disease-causing mutations in the TRPV family were first identified in TRPV4, a widely expressed polymodal channel that responds to innocuous warm temperatures (25-35°C), as well as mechanical stress, hyposmia, and a set of chemical ligands [142,154]. TRPV4 is expressed widely throughout the human body, playing a vital role in maintaining homeostasis in the vascular, cardiac, respiratory, urinary, skeletal, digestive, and nervous system. Despite its widespread expression and functional versatility, reported TRPV4 channelopathies exhibit striking tissue-specific phenotypes which can be classified into two groups with distinct pathophysiological mechanisms: neuropathic disorders and skeletal disorders. In a growing number of cases, patients may exhibit combined neuronal and skeletal phenotypes[155-158]. An enduring mystery in the field has been why TRPV4 channelopathic mutations have such strong tissue-specific phenotypes, and what the underlying basis of this phenotypic segregation is.

The first TRPV4 channelopathies were identified in patients with an autosomal dominant skeletal dysplasia known as brachyolmia (Greek: “short trunk”, where patients develop a short stature from childhood due to platyspondyly, or flattening of the spinal cord) [159]. These were heterozygous missense mutations, R616Q and V620I, located in the S5 helix [160,161] , which caused constitutive TRPV4 activity, as well as enhanced response to chemical and hypotonic stimulation. Since then, a whole host of mostly heterozygous TRPV4 missense mutations have been identified in multiple skeletal dysplasias of varying severity and symptomology. Almost all of these mutants exhibit higher basal activity than WT, while only some exhibit increased stimulus-evoked current [162,163]. How increased TRPV4 activity leads to skeletal dysplasias has yet to be fully elucidated, though some lines of evidence suggest that TRPV4 is a key downstream regulator of gene expression during chondrocyte differentiation and endochondral ossification, which are necessary processes for proper bone growth and homeostasis. Studies suggest that hyperactive mutants of TRPV4 dysregulate Ca^{2+}-dependent transcription of genes, causing reduced bone morphogenic protein (BMP) signaling, and therefore differentiation, in chondrocytes [164-166]. In another study, a dysplasia patient with the GoF L619F TRPV4 mutation, SOX9 was found to be upregulated,

leading to accelerated chrondrocyte differentiation [167]. Neuropathic TRPV4 mutations seem to largely affect motor and sensorimotor function, and have been linked to Charcot–Marie–Tooth disease type 2C (CMT2C) [168], scapuloperoneal spinal muscular atrophy (SPSMA) [169,170] and congenital distal spinal muscular atrophy (CDSMA). Unlike skeletal-dysplasia mutations, which all unilaterally lead to gain of function due to constitutive channel activity, neuropathic mutations have a more heterogenous effect on channel activity, with most mutations exhibiting gain-of-function via constitutive or enhanced activity [158,168,170] while a select few reportedly show loss of function via reduced expression, plasma membrane localization, and/or agonist-evoked currents [169,171]. Some studies have proposed that GoF mutations facilitate toxic Ca^{2+}-overload, leading to motor neuron degeneration in a set of TRPV4-dependent neuropathies [172]. However, this does not explain why many skeletal dysplasia patients with GoF TRPV4 mutations have no detectable motor neuron atrophy, suggesting more complex mechanisms are involved.

Clues into TRPV4 pathophysiological mechanisms are found when mutations are cumulatively mapped to the TRPV4 structure (**Figure 5**). Skeletal dysplasia mutations can be found throughout the channel structure, especially near the S4-S5 linker/TRP helix, the pore domain, and cytoplasmic interfacial regions critical for inter-subunit assembly [160]. Thus, skeletal dysplasia mutations seem to largely disrupt inherent channel gating and tetramerization properties to trigger disease pathology. Supporting this, two GoF skeletal dysplasia mutations were found to lie upstream of the C-terminal calmodulin-binding region, and revealed a putative auto-inhibitory domain responsible for maintaining the closed state [163]. In stark contrast to skeletal dysplasia mutations, neuropathic TRPV4 mutations are very heavily clustered around cytosolic N-terminal ankyrin repeat domain (ARD). Structurally, these mutations occur on the outmost-facing region of the ARD, which presumably mediates scaffolding and protein-protein interactions (**Figure 5B**). This finding opens up the intriguing possibility that disruption of interactions with cell-specific binding partners may underlie the phenotypic segregation of TRPV4 mutants between neuronal and skeletal tissues. Indeed, neuropathic mutations have been shown to selectively

disrupt binding of TRPV4 to the small GTPase RhoA, which has an inhibitory effect on TRPV4 activity [161,173,174]. Loss of TRPV4-RhoA binding can induce cytoskeletal reorganization and ultimately impair neurite growth and inhibit axonal regeneration after injury [173,175].

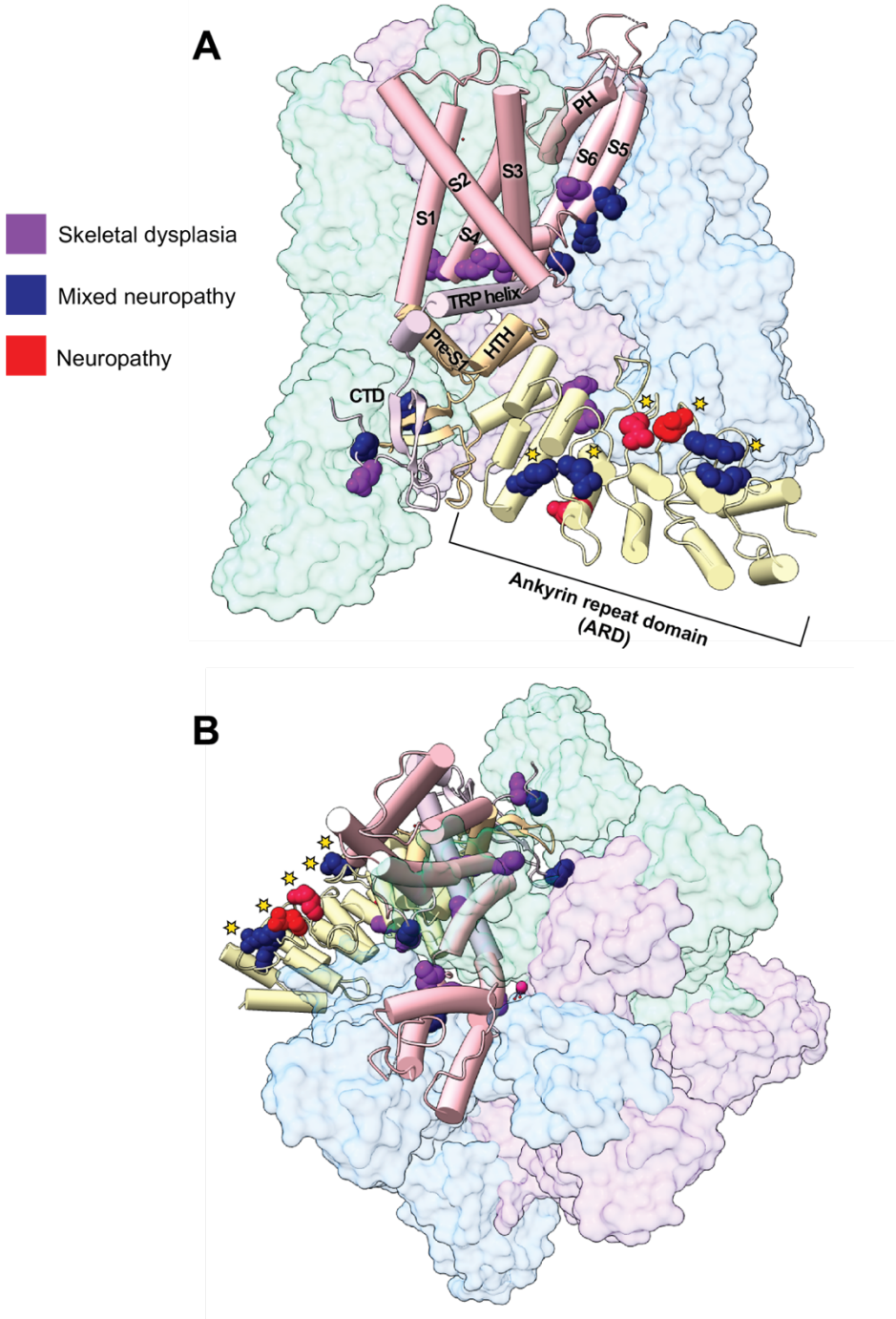

Figure 5: TRPV4 disease mutations mapped onto Cryo-EM structure (PDB: 8T1B)
A: full tetramer with monomer tube helices colored and structural domains labeled. Surface densities of neighboring 3 subunits indicated in green blue, and purple. Residues mutated in channelopathic conditions are color-coded according to pathology type**. B,C:** Top view of full tetramer. RhoA-binding sites starred

TRPV6: TRPV6 was identified at the turn of the century and was initially believed to be a relative of cation transporter CaT1 before its designation as a TRP family member [176,177]. A highly calcium-permeable channel, TRPV6 is expressed in epithelial tissues - especially the placenta, as well as a few exocrine glands, including the pancreas, salivary, mammary, and sweat glands, and is believed to facilitate calcium entry into vital organs.

In 2018, an exome-sequencing study linked TRPV6 mutations on both alleles to transient neonatal hyperparathyroidism (TNHP) with skeletal dysplasia, in which placental transport of Ca^{2+} from the mother to the fetus is disrupted. Newborn patients harboring these mutations experience insufficient bone mineralization, with rib and femoral fractures and narrowing of the chest. These issues tend to resolve within the first two years of life, indicating that only maternal-fetal calcium transport is affected, and other calcification mechanisms may compensate for TRPV6 loss during development. Missense mutations causing TNHP such as R390H, C212T, R425Q, G428R, and R483W cause loss of function when tested with patch clamp in overexpression systems [178,179]. Often, patients will exhibit different mutations in each allele – where one or both mutations causes loss of function.

Interestingly, a recent study conducted on French, German, and Japanese patients showed that TRPV6 loss-of-function may also contribute to non-alcohol dependent chronic pancreatitis [180]. More TRPV6 loss of function variants underlying pancreatitis were subsequently identified in other groups [181,182]. The exact etiology of this disease and what differentiates it from TNHP pathways still requires more study.

vi. TRPA1:

TRPA1, the only member of its subfamily in humans, earns its name from its extensive N-terminal ankyrin repeats, and is best known as a versatile chemosensor expressed in primary afferent nociceptive neurons. Often nicknamed “the wasabi receptor” due to its activation by horseradish component allyl isothiocyanate, TRPA1 can be activated by a diverse array of over

100 environmental and endogenous chemical irritants that fall into two groups: electrophiles which covalently bind to N-terminal cysteine residues, and non-electrophiles which bind within the transmembrane region [183]. Some evidence also exists that TRPA1 can sense noxious cold [184]. TRPA1, alongside other nociceptor TRPs such as TRPV1 and TRPM8, is thought to play an integral role in acute pain sensing, initiating neuronal depolarization in response to noxious stimuli, and also driving chronic pain and neurogenic inflammation. New studies have highlighted critical roles of TRPA1 expressed outside sensory nerves, including the respiratory, vascular, and gastrointestinal systems, though these pathways have yet to be fully elucidated.

In 2010, Kremeyer et al identified a TRPA1 point mutation underlying a rare autosomal dominant channelopathy familial episodic pain syndrome (FEPS). Prior to the discovery of FEPS, no heritable pain disorders in humans had yet been linked to TRP channel mutations (most are attributed to voltage-gated sodium and calcium channels), thus validating the importance of TRPA1 in pain sensation. FEPS patients exhibit a gain-of-function missense mutation (N855S) in the S4-S5 linker region of TRPA1 that ultimately produces symptoms of severe episodes of upper body pain triggered by fatigue, cold, or fasting [185]. Outside of these episodes, however, patients reported no altered pain sensitivity. Functional analysis of the N855S mutant reveals a more then five-fold larger inward current at negative membrane potentials compared to WT TRPA1 with no perturbations to channel trafficking. Subsequent structural modeling and patch-clamp experiments showed that residues within the S4-S5 region of TRPA1 form inter-subunit salt bridges that stabilize the open conformation of the channel[186] (**Figure 6A**). Interestingly, Gupta et al report that the N855 amino acid plays a vital role in inhibition of TRPA1 with the synthetic antagonist HC-03003, and that mutation of this residue to Ser results in reduced inhibition of TRPA1 currents[187]. The authors put forward an intriguing possibility that perhaps there are endogenous TRPA1 inhibitors yet to be discovered that may have reduced efficacy in the presence of the FEPS mutation.

8 years after the N855S FEPS mutation was reported, a new TRPA1 mutation was identified in a heterozygous father-son pair with cramp fasciculation syndrome (CFS) [188]. The authors designated this condition CRAMPT after its core clinical presentations in multiple tissue types: cramp fasciculation, reflux, asthma/anxiety, migraine, paresthesia/pain, and tachycardia / tremor. The CRAMPT TRPA1 variant introduces a nonsense mutation at R919, and the resulting R919* TRPA1 protein lacks the last 201 amino acids, including the 6th transmembrane helix and the entire cytoplasmic C-terminus. Intriguingly, patients' symptoms were alleviated by the sodium channel blocker carbamazepine, suggesting neuronal hyperexcitability or gain-of-function underlying CRAPMT, despite the expected loss-of-function of the R919* TRPA1 mutation. Our group recently uncovered a very unique mechanism for gain-of-function conferred by R919*, in which the truncated R919* mutant co-assembles with WT TRPA1 subunits into heteromeric channels that are functional at the plasma membrane [189] (**Figure 6B**). When expressed alone, R919* TRPA1 is functionally inactive, and thus it requires assembly with WT in a heterozygous background to exert its functional effects. Unlike the N855S FEPS-associated mutation, the hyperactivity of WT-R919* heteromers is only pronounced in the presence of Ca^{2+}. WT-R919* heteromers exhibit increased inward Ca^{2+} permeation and enhanced sensitivity to multiple agonists, likely due to dilated pore architecture and lowering of energetic barriers to gating contributed by missing structural elements. To our knowledge, this mechanism is the first reported TRP channelopathy in which a truncation mutation lacking pore-forming helices directly contributes to gain-of-function.

The FEPS and CRAMPT TRPA1 mutations lead to channel gain-of-function through very distinct structural mechanisms, and would both ultimately cause increased cation flux in sensory neurons, which may readily trigger depolarization and cause increased pain signaling. However, while both FEPS and CRAMPT patients do experience pain symptoms, the onset, localization, and duration of pain differs significantly. In addition, CRAMPT patients reportedly exhibit a host of non-sensory symptoms indicating disruption of numerous other TRPA1 pathways that have yet

to be fully explored. For example, enhanced activation of TRPA1 in the lung epithelia, vasculature, and gastrointestinal system has recently been shown to underlie chronic cough / asthma, vasodilation, and gut inflammation [190-193], which could contribute to patient symptoms. Further work is needed to determine exactly how TRPA1 gain-of-function results in these phenotypic changes across various tissue types.

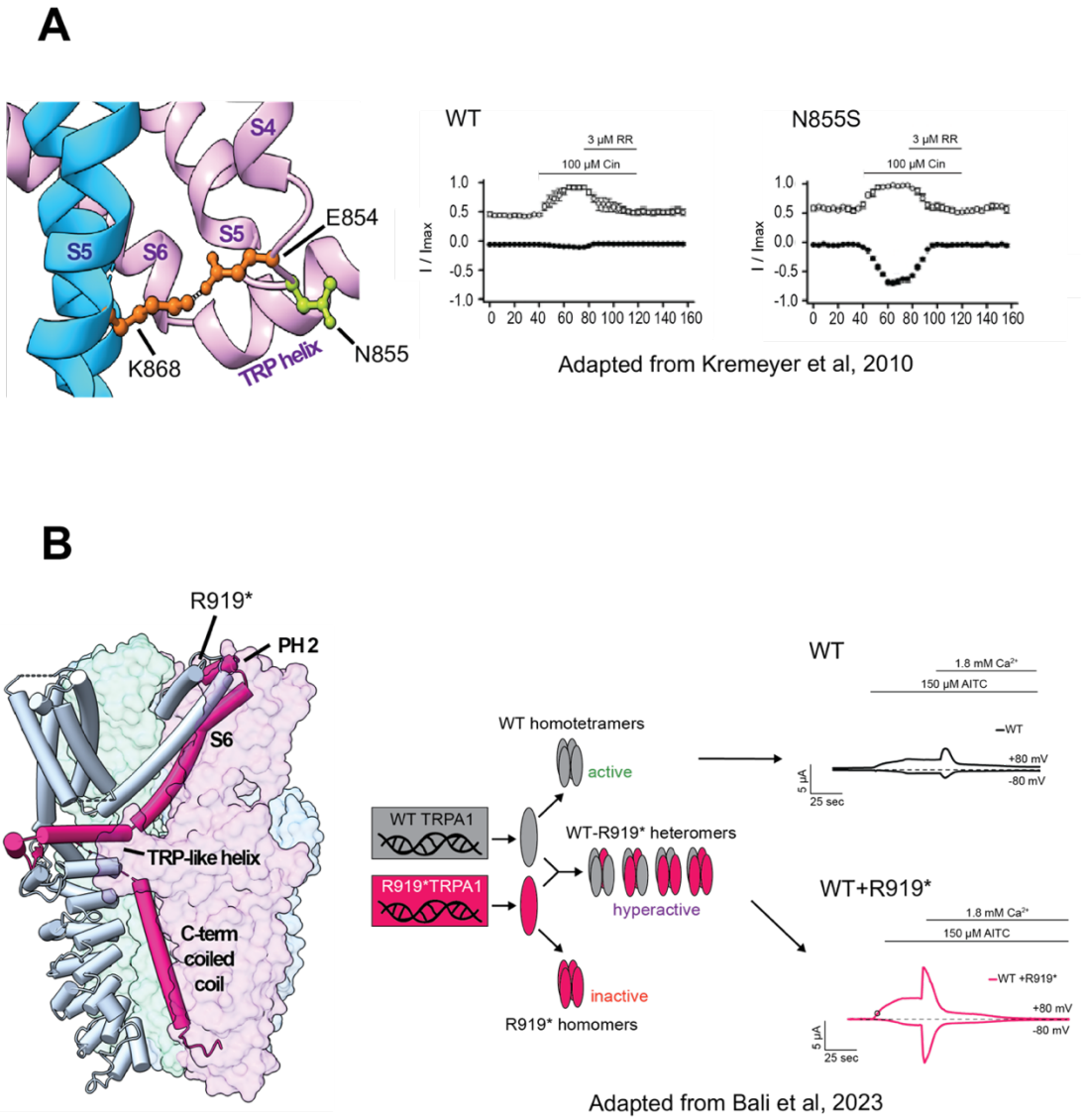

Figure 6: **Structural context and functional profiles of two distinct TRPA1 channelopthies (PDB: 6V9X) A:** FEPS-associated N855S mutation (yellow) flanks the conserved E854 residue, which forms a salt bridge with K868 on a neighboring TRPA1 subunit when the channel is in the open conformation. This leads to larger agonist-evoked currents at negative potentials.
B: CRAMPT- associated R919* mutation causes truncation of 19% of the protein (pink tubes). Truncated and full length subunits are both expressed in patients, and form hyperactive heteromeric channels with larger agonist-evoked currents in the presence of calcium at both positive and negative potentials.

vii. *Considerations when studying TRP channelopathies:*

Characterization of channelopathic mechanisms is an important step into understanding how TRP channels contribute to physiology, and can illuminate therapeutic strategies to alleviate symptoms in patients. When performing these studies, several factors should be taken into consideration. First is the patient genotype - are disease-causing mutations homozygous or heterozygous? In heterozygous conditions, does co-expression with wild-type protein affect the functional outcome? While co-expression of mutant and WT often causes intermediate responses, in some cases it reveals novel properties compared to homozygous conditions. This has been shown for the TRPA1 CRAMPT mutant, for example, which requires co-expression with WT to exert GoF. This has also been shown for TRPV3 Olmsted Syndrome patients, where co-expression of WT and GoF variants produces a distinct activity profile suggesting more sensitive channels. In this vein, splice variants also should be considered in pathomechanisms. Mutations may have differential effects depending on the isoform on which they occur, and certain channel isoforms may have different tissue expression profiles that may affect disease phenotype.

Another consideration is co-assembly of TRP channels with other TRP members, or even from outside the TRP family, thus broadening the function, subcellular localization, and physiological roles of a given TRP family member. For example, when studying PKD2 (TRPP2) mutations, the possible heterochannel formation of PKD2 with PKD1, TRPCs, and TRPVs can conceivably impact the pathogencity of mutations in PKD2 in distinct ways. Additionally, recent pentameric TRPV3 structures published by Lansky et al show the possibility of alternate non-cannonical TRP channel oligomeric states [152].

While *in vitro* methods have enormously enhanced our understanding of TRP channel mutants, there are substantial limitations worth considering. From a structural perspective, being able to solve high resolution structures of TRP channels with cryo-EM has improved our mechanistic understanding of disease mutations. However, many structures have been solved with flexible domains removed to improve biochemical stability. These flexible domains often

contain hotspots for genetic variation, and thus removing these regions prevents us from studying the structural pathogenesis of many diseases. In vitro functional studies of channelopathic mutations in heterologous systems, while useful for measuring inherent alterations in biophysical channel properties, also may lack tissue-specific factors important for driving pathology. For example, TRPC6 is known to directly interact with kidney podocyte proteins nephrin and podocin, which are potential players in disease phenotypes for TRPC6 channelopathies [27,28]. However, these proteins are not present in heterologous cell types commonly used for biophysical ion channel studies. Moreover, for many TRP channels we simply do not yet know the physiologically relevant activators that drive aberrant function in disease states. The relevant environmental and endogenous stimuli surrounding a given channel should therefore be considered *in vitro* studies, which often utilize artificial or non-physiological activators.

1.3 Concluding Remarks

Many decades ago, a detailed investigation of novel *Drosophila* mutants originated the entire field of TRP channel research, highlighting the importance of studying genetic mutations that underlie distinct phenotypes. Today, it is clear that TRP channels play crucial roles in the physiology of multiple systems, and we are still uncovering the exact mechanisms in which TRP channels participate. The expanding list of known TRP channelopathies provides clues into how specific alterations in these channels can lead to disease phenotypes, and can fill in previously elusive details of cellular pathways that drive human physiology. Therefore, the rigorous study of these mutations using a combination of techniques will be imperative to understanding TRP channel regulation and function, and will also help inform and develop therapeutic strategies to alleviate TRP-dependent pathologies.

1.4 References

1. Cosens, D.J. & Manning, A. Abnormal electroretinogram from a Drosophila mutant. *Nature* **224**, 285-7 (1969).
2. Hardie, R.C. & Minke, B. The trp gene is essential for a light-activated Ca2+ channel in Drosophila photoreceptors. *Neuron* **8**, 643-51 (1992).
3. Montell, C. & Rubin, G.M. Molecular characterization of the Drosophila trp locus: a putative integral membrane protein required for phototransduction. *Neuron* **2**, 1313-23 (1989).
4. Voets, T., Talavera, K., Owsianik, G. & Nilius, B. Sensing with TRP channels. *Nat Chem Biol* **1**, 85-92 (2005).
5. Nilius, B. & Szallasi, A. Transient receptor potential channels as drug targets: from the science of basic research to the art of medicine. *Pharmacol Rev* **66**, 676-814 (2014).
6. Cheng, W., Sun, C. & Zheng, J. Heteromerization of TRP channel subunits: extending functional diversity. *Protein Cell* **1**, 802-10 (2010).
7. Nilius, B. & Owsianik, G. Transient receptor potential channelopathies. *Pflugers Arch* **460**, 437-50 (2010).
8. Yue, L. & Xu, H. TRP channels in health and disease at a glance. *J Cell Sci* **134**(2021).
9. Wang, H. et al. TRPC channels: Structure, function, regulation and recent advances in small molecular probes. *Pharmacol Ther* **209**, 107497 (2020).
10. Hofmann, T., Schaefer, M., Schultz, G. & Gudermann, T. Subunit composition of mammalian transient receptor potential channels in living cells. *Proc Natl Acad Sci U S A* **99**, 7461-6 (2002).
11. Storch, U., Forst, A.L., Philipp, M., Gudermann, T. & Mederos y Schnitzler, M. Transient receptor potential channel 1 (TRPC1) reduces calcium permeability in heteromeric channel complexes. *J Biol Chem* **287**, 3530-40 (2012).
12. Zhang, Z. et al. Activation of Trp3 by inositol 1,4,5-trisphosphate receptors through displacement of inhibitory calmodulin from a common binding domain. *Proc Natl Acad Sci U S A* **98**, 3168-73 (2001).
13. Tang, J. et al. Identification of common binding sites for calmodulin and inositol 1,4,5-trisphosphate receptors on the carboxyl termini of trp channels. *J Biol Chem* **276**, 21303-10 (2001).
14. Ambudkar, I.S., de Souza, L.B. & Ong, H.L. TRPC1, Orai1, and STIM1 in SOCE: Friends in tight spaces. *Cell Calcium* **63**, 33-39 (2017).
15. Winn, M.P. et al. A mutation in the TRPC6 cation channel causes familial focal segmental glomerulosclerosis. *Science* **308**, 1801-4 (2005).
16. Reiser, J. et al. TRPC6 is a glomerular slit diaphragm-associated channel required for normal renal function. *Nat Genet* **37**, 739-44 (2005).
17. Riehle, M. et al. TRPC6 G757D Loss-of-Function Mutation Associates with FSGS. *J Am Soc Nephrol* **27**, 2771-83 (2016).
18. Gigante, M. et al. TRPC6 mutations in children with steroid-resistant nephrotic syndrome and atypical phenotype. *Clin J Am Soc Nephrol* **6**, 1626-34 (2011).
19. Liu, Z. et al. Novel gain-of-function mutation of TRPC6 Q134P contributes to late onset focal segmental glomerulosclerosis in a Chinese pedigree. *Nephrology (Carlton)* **26**, 1018-1025 (2021).
20. Heeringa, S.F. et al. A novel TRPC6 mutation that causes childhood FSGS. *PLoS One* **4**, e7771 (2009).
21. Polat, O.K. et al. Contribution of Coiled-Coil Assembly to Ca(2+)/Calmodulin-Dependent Inactivation of TRPC6 Channel and its Impacts on FSGS-Associated Phenotypes. *J Am Soc Nephrol* **30**, 1587-1603 (2019).
22. Sun, Z.J. et al. Genetic Interactions Between TRPC6 and NPHS1 Variants Affect Posttransplant Risk of Recurrent Focal Segmental Glomerulosclerosis. *Am J Transplant* **15**, 3229-38 (2015).
23. Azumaya, C.M., Sierra-Valdez, F., Cordero-Morales, J.F. & Nakagawa, T. Cryo-EM structure of the cytoplasmic domain of murine transient receptor potential cation channel subfamily C member 6 (TRPC6). *J Biol Chem* **293**, 10381-10391 (2018).
24. Guo, W. et al. Structural mechanism of human TRPC3 and TRPC6 channel regulation by their intracellular calcium-binding sites. *Neuron* **110**, 1023-1035 e5 (2022).
25. Chen, S. et al. Calcium entry via TRPC6 mediates albumin overload-induced endoplasmic reticulum stress and apoptosis in podocytes. *Cell Calcium* **50**, 523-9 (2011).

26. Pollak, M.R. Familial FSGS. *Adv Chronic Kidney Dis* **21**, 422-5 (2014).
27. Kanda, S. et al. Tyrosine phosphorylation-dependent activation of TRPC6 regulated by PLC-gamma1 and nephrin: effect of mutations associated with focal segmental glomerulosclerosis. *Mol Biol Cell* **22**, 1824-35 (2011).
28. Dryer, S.E., Roshanravan, H. & Kim, E.Y. TRPC channels: Regulation, dysregulation and contributions to chronic kidney disease. *Biochim Biophys Acta Mol Basis Dis* **1865**, 1041-1066 (2019).
29. Singh, I. et al. Galphaq-TRPC6-mediated Ca2+ entry induces RhoA activation and resultant endothelial cell shape change in response to thrombin. *J Biol Chem* **282**, 7833-43 (2007).
30. Wang, Y. et al. Activation of NFAT signaling in podocytes causes glomerulosclerosis. *J Am Soc Nephrol* **21**, 1657-66 (2010).
31. Schlondorff, J., Del Camino, D., Carrasquillo, R., Lacey, V. & Pollak, M.R. TRPC6 mutations associated with focal segmental glomerulosclerosis cause constitutive activation of NFAT-dependent transcription. *Am J Physiol Cell Physiol* **296**, C558-69 (2009).
32. Chiluiza, D., Krishna, S., Schumacher, V.A. & Schlondorff, J. Gain-of-function mutations in transient receptor potential C6 (TRPC6) activate extracellular signal-regulated kinases 1/2 (ERK1/2). *J Biol Chem* **288**, 18407-20 (2013).
33. Luo, Y., Vassilev, P.M., Li, X., Kawanabe, Y. & Zhou, J. Native polycystin 2 functions as a plasma membrane Ca2+-permeable cation channel in renal epithelia. *Mol Cell Biol* **23**, 2600-7 (2003).
34. Shimizu, T., Janssens, A., Voets, T. & Nilius, B. Regulation of the murine TRPP3 channel by voltage, pH, and changes in cell volume. *Pflugers Arch* **457**, 795-807 (2009).
35. Gabow, P.A. Autosomal dominant polycystic kidney disease. *N Engl J Med* **329**, 332-42 (1993).
36. Cantero, M.D.R. & Cantiello, H.F. Polycystin-2 (TRPP2): Ion channel properties and regulation. *Gene* **827**, 146313 (2022).
37. Chauvet, V. et al. Expression of PKD1 and PKD2 transcripts and proteins in human embryo and during normal kidney development. *Am J Pathol* **160**, 973-83 (2002).
38. Mochizuki, T. et al. PKD2, a gene for polycystic kidney disease that encodes an integral membrane protein. *Science* **272**, 1339-42 (1996).
39. Wu, G. & Somlo, S. Molecular genetics and mechanism of autosomal dominant polycystic kidney disease. *Mol Genet Metab* **69**, 1-15 (2000).
40. Cornec-Le Gall, E. et al. PKD2-Related Autosomal Dominant Polycystic Kidney Disease: Prevalence, Clinical Presentation, Mutation Spectrum, and Prognosis. *Am J Kidney Dis* **70**, 476-485 (2017).
41. Wang, Y. et al. The diverse effects of pathogenic point mutations on ion channel activity of a gain-of-function polycystin-2. *J Biol Chem* **299**, 104674 (2023).
42. Miyagi, K. et al. A pathogenic C terminus-truncated polycystin-2 mutant enhances receptor-activated Ca2+ entry via association with TRPC3 and TRPC7. *J Biol Chem* **284**, 34400-12 (2009).
43. Delmas, P. et al. Gating of the polycystin ion channel signaling complex in neurons and kidney cells. *FASEB J* **18**, 740-2 (2004).
44. Wang, Z. et al. The ion channel function of polycystin-1 in the polycystin-1/polycystin-2 complex. *EMBO Rep* **20**, e48336 (2019).
45. Hanaoka, K. et al. Co-assembly of polycystin-1 and -2 produces unique cation-permeable currents. *Nature* **408**, 990-4 (2000).
46. Su, Q. et al. Structure of the human PKD1-PKD2 complex. *Science* **361**(2018).
47. Tian, P.F., Sun, M.M., Hu, X.Y., Du, J. & He, W. TRPP2 ion channels: The roles in various subcellular locations. *Biochimie* **201**, 116-127 (2022).
48. Cai, Y. et al. Altered trafficking and stability of polycystins underlie polycystic kidney disease. *J Clin Invest* **124**, 5129-44 (2014).
49. Grimm, D.H. et al. Polycystin-2 regulates proliferation and branching morphogenesis in kidney epithelial cells. *J Biol Chem* **281**, 137-44 (2006).
50. Chang, M.Y. et al. Haploinsufficiency of Pkd2 is associated with increased tubular cell proliferation and interstitial fibrosis in two murine Pkd2 models. *Nephrol Dial Transplant* **21**, 2078-84 (2006).
51. Bhunia, A.K. et al. PKD1 induces p21(waf1) and regulation of the cell cycle via direct activation of the JAK-STAT signaling pathway in a process requiring PKD2. *Cell* **109**, 157-68 (2002).

52. Kottgen, M. TRPP2 and autosomal dominant polycystic kidney disease. *Biochim Biophys Acta* **1772**, 836-50 (2007).
53. Otto, E.A. et al. Mutations in INVS encoding inversin cause nephronophthisis type 2, linking renal cystic disease to the function of primary cilia and left-right axis determination. *Nat Genet* **34**, 413-20 (2003).
54. Winkler, P.A., Huang, Y., Sun, W., Du, J. & Lu, W. Electron cryo-microscopy structure of a human TRPM4 channel. *Nature* **552**, 200-204 (2017).
55. Jimenez, I. et al. TRPM Channels in Human Diseases. *Cells* **9**(2020).
56. Fonfria, E. et al. Tissue distribution profiles of the human TRPM cation channel family. *J Recept Signal Transduct Res* **26**, 159-78 (2006).
57. Duncan, L.M. et al. Down-regulation of the novel gene melastatin correlates with potential for melanoma metastasis. *Cancer Res* **58**, 1515-20 (1998).
58. Morgans, C.W. et al. TRPM1 is required for the depolarizing light response in retinal ON-bipolar cells. *Proc Natl Acad Sci U S A* **106**, 19174-8 (2009).
59. Xu, Y. et al. The TRPM1 channel in ON-bipolar cells is gated by both the alpha and the betagamma subunits of the G-protein Go. *Sci Rep* **6**, 20940 (2016).
60. Bellone, R.R. et al. Differential gene expression of TRPM1, the potential cause of congenital stationary night blindness and coat spotting patterns (LP) in the Appaloosa horse (Equus caballus). *Genetics* **179**, 1861-70 (2008).
61. Koike, C., Numata, T., Ueda, H., Mori, Y. & Furukawa, T. TRPM1: a vertebrate TRP channel responsible for retinal ON bipolar function. *Cell Calcium* **48**, 95-101 (2010).
62. Li, Z. et al. Recessive mutations of the gene TRPM1 abrogate ON bipolar cell function and cause complete congenital stationary night blindness in humans. *Am J Hum Genet* **85**, 711-9 (2009).
63. Iosifidis, C. et al. Clinical and genetic findings in TRPM1-related congenital stationary night blindness. *Acta Ophthalmol* **100**, e1332-e1339 (2022).
64. Koike, C. et al. TRPM1 is a component of the retinal ON bipolar cell transduction channel in the mGluR6 cascade. *Proc Natl Acad Sci U S A* **107**, 332-7 (2010).
65. Neuille, M. et al. LRIT3 is essential to localize TRPM1 to the dendritic tips of depolarizing bipolar cells and may play a role in cone synapse formation. *Eur J Neurosci* **42**, 1966-75 (2015).
66. Nakamura, M. et al. TRPM1 mutations are associated with the complete form of congenital stationary night blindness. *Mol Vis* **16**, 425-37 (2010).
67. Cao, Y., Posokhova, E. & Martemyanov, K.A. TRPM1 forms complexes with nyctalopin in vivo and accumulates in postsynaptic compartment of ON-bipolar neurons in mGluR6-dependent manner. *J Neurosci* **31**, 11521-6 (2011).
68. Oancea, E. et al. TRPM1 forms ion channels associated with melanin content in melanocytes. *Sci Signal* **2**, ra21 (2009).
69. Fang, D. & Setaluri, V. Expression and Up-regulation of alternatively spliced transcripts of melastatin, a melanoma metastasis-related gene, in human melanoma cells. *Biochem Biophys Res Commun* **279**, 53-61 (2000).
70. Xu, X.Z., Moebius, F., Gill, D.L. & Montell, C. Regulation of melastatin, a TRP-related protein, through interaction with a cytoplasmic isoform. *Proc Natl Acad Sci U S A* **98**, 10692-7 (2001).
71. Lee, N. et al. Expression and characterization of human transient receptor potential melastatin 3 (hTRPM3). *J Biol Chem* **278**, 20890-7 (2003).
72. Grimm, C., Kraft, R., Sauerbruch, S., Schultz, G. & Harteneck, C. Molecular and functional characterization of the melastatin-related cation channel TRPM3. *J Biol Chem* **278**, 21493-501 (2003).
73. Wang, H.P., Pu, X.Y. & Wang, X.H. Distribution profiles of transient receptor potential melastatin-related and vanilloid-related channels in prostatic tissue in rat. *Asian J Androl* **9**, 634-40 (2007).
74. Oberwinkler, J. & Philipp, S.E. Trpm3. *Handb Exp Pharmacol* **222**, 427-59 (2014).
75. Fruhwald, J. et al. Alternative splicing of a protein domain indispensable for function of transient receptor potential melastatin 3 (TRPM3) ion channels. *J Biol Chem* **287**, 36663-72 (2012).
76. Oberwinkler, J., Lis, A., Giehl, K.M., Flockerzi, V. & Philipp, S.E. Alternative splicing switches the divalent cation selectivity of TRPM3 channels. *J Biol Chem* **280**, 22540-8 (2005).
77. Bennett, T.M., Mackay, D.S., Siegfried, C.J. & Shiels, A. Mutation of the melastatin-related cation channel, TRPM3, underlies inherited cataract and glaucoma. *PLoS One* **9**, e104000 (2014).

78. Zhou, Y., Bennett, T.M. & Shiels, A. Mutation of the TRPM3 cation channel underlies progressive cataract development and lens calcification associated with pro-fibrotic and immune cell responses. *FASEB J* **35**, e21288 (2021).
79. Rhodes, J.D. & Sanderson, J. The mechanisms of calcium homeostasis and signalling in the lens. *Exp Eye Res* **88**, 226-34 (2009).
80. Brown, R.L. et al. TRPM3 expression in mouse retina. *PLoS One* **10**, e0117615 (2015).
81. Shiels, A. TRPM3_miR-204: a complex locus for eye development and disease. *Hum Genomics* **14**, 7 (2020).
82. Burglen, L. et al. Gain-of-function variants in the ion channel gene TRPM3 underlie a spectrum of neurodevelopmental disorders. *Elife* **12**(2023).
83. Zhao, S., Yudin, Y. & Rohacs, T. Disease-associated mutations in the human TRPM3 render the channel overactive via two distinct mechanisms. *Elife* **9**(2020).
84. Van Hoeymissen, E. et al. Gain of channel function and modified gating properties in TRPM3 mutants causing intellectual disability and epilepsy. *Elife* **9**(2020).
85. Dyment, D.A. et al. De novo substitutions of TRPM3 cause intellectual disability and epilepsy. *Eur J Hum Genet* **27**, 1611-1618 (2019).
86. Zhao, C. & MacKinnon, R. Structural and functional analyses of a GPCR-inhibited ion channel TRPM3. *Neuron* **111**, 81-91 e7 (2023).
87. Naylor, J. et al. Pregnenolone sulphate- and cholesterol-regulated TRPM3 channels coupled to vascular smooth muscle secretion and contraction. *Circ Res* **106**, 1507-15 (2010).
88. Abriel, H., Syam, N., Sottas, V., Amarouch, M.Y. & Rougier, J.S. TRPM4 channels in the cardiovascular system: physiology, pathophysiology, and pharmacology. *Biochem Pharmacol* **84**, 873-81 (2012).
89. Smith, A.C. et al. TRPM4 channel: a new player in urinary bladder smooth muscle function in rats. *Am J Physiol Renal Physiol* **304**, F918-29 (2013).
90. Cho, C.H., Lee, Y.S., Kim, E., Hwang, E.M. & Park, J.Y. Physiological functions of the TRPM4 channels via protein interactions. *BMB Rep* **48**, 1-5 (2015).
91. Launay, P. et al. TRPM4 is a Ca2+-activated nonselective cation channel mediating cell membrane depolarization. *Cell* **109**, 397-407 (2002).
92. Liu, H. et al. Molecular genetics and functional anomalies in a series of 248 Brugada cases with 11 mutations in the TRPM4 channel. *PLoS One* **8**, e54131 (2013).
93. Gualandi, F. et al. Mutation Load of Multiple Ion Channel Gene Mutations in Brugada Syndrome. *Cardiology* **137**, 256-260 (2017).
94. Daumy, X. et al. Targeted resequencing identifies TRPM4 as a major gene predisposing to progressive familial heart block type I. *Int J Cardiol* **207**, 349-58 (2016).
95. Kruse, M. et al. Impaired endocytosis of the ion channel TRPM4 is associated with human progressive familial heart block type I. *J Clin Invest* **119**, 2737-44 (2009).
96. Stallmeyer, B. et al. Mutational spectrum in the Ca(2+)--activated cation channel gene TRPM4 in patients with cardiac conductance disturbances. *Hum Mutat* **33**, 109-17 (2012).
97. Bianchi, B., Ozhathil, L.C., Medeiros-Domingo, A., Gollob, M.H. & Abriel, H. Four TRPM4 Cation Channel Mutations Found in Cardiac Conduction Diseases Lead to Altered Protein Stability. *Front Physiol* **9**, 177 (2018).
98. Palladino, A. et al. The Role of TRPM4 Gene Mutations in Causing Familial Progressive Cardiac Conduction Disease: A Further Contribution. *Genes (Basel)* **13**(2022).
99. Amarouch, M.Y. & El Hilaly, J. Inherited Cardiac Arrhythmia Syndromes: Focus on Molecular Mechanisms Underlying TRPM4 Channelopathies. *Cardiovasc Ther* **2020**, 6615038 (2020).
100. Liu, H. et al. Gain-of-function mutations in TRPM4 cause autosomal dominant isolated cardiac conduction disease. *Circ Cardiovasc Genet* **3**, 374-85 (2010).
101. Xian, W. et al. Aberrant Deactivation-Induced Gain of Function in TRPM4 Mutant Is Associated with Human Cardiac Conduction Block. *Cell Rep* **24**, 724-731 (2018).
102. Demion, M. et al. Trpm4 gene invalidation leads to cardiac hypertrophy and electrophysiological alterations. *PLoS One* **9**, e115256 (2014).
103. Wang, H. et al. Gain-of-Function Mutations in TRPM4 Activation Gate Cause Progressive Symmetric Erythrokeratodermia. *J Invest Dermatol* **139**, 1089-1097 (2019).
104. Duan, J. et al. Structure of full-length human TRPM4. *Proc Natl Acad Sci U S A* **115**, 2377-2382 (2018).

105. Schlingmann, K.P. & Gudermann, T. A critical role of TRPM channel-kinase for human magnesium transport. *J Physiol* **566**, 301-8 (2005).
106. Li, M., Jiang, J. & Yue, L. Functional characterization of homo- and heteromeric channel kinases TRPM6 and TRPM7. *J Gen Physiol* **127**, 525-37 (2006).
107. Elizan, T.S. et al. Amyotrophic lateral sclerosis and parkinsonism-dementia complex of Guam. Neurological reevaluation. *Arch Neurol* **14**, 356-68 (1966).
108. Hermosura, M.C. & Garruto, R.M. TRPM7 and TRPM2-Candidate susceptibility genes for Western Pacific ALS and PD? *Biochim Biophys Acta* **1772**, 822-35 (2007).
109. Hermosura, M.C. et al. A TRPM7 variant shows altered sensitivity to magnesium that may contribute to the pathogenesis of two Guamanian neurodegenerative disorders. *Proc Natl Acad Sci U S A* **102**, 11510-5 (2005).
110. Cai, N., Bai, Z., Nanda, V. & Runnels, L.W. Mass Spectrometric Analysis of TRPM6 and TRPM7 Phosphorylation Reveals Regulatory Mechanisms of the Channel-Kinases. *Sci Rep* **7**, 42739 (2017).
111. Wang, L. et al. Structures and gating mechanism of human TRPM2. *Science* **362**(2018).
112. Hermosura, M.C. et al. Altered functional properties of a TRPM2 variant in Guamanian ALS and PD. *Proc Natl Acad Sci U S A* **105**, 18029-34 (2008).
113. Bocca, B. et al. Metal changes in CSF and peripheral compartments of parkinsonian patients. *J Neurol Sci* **248**, 23-30 (2006).
114. Yasui, M. & Ota, K. Experimental and clinical studies on dysregulation of magnesium metabolism and the aetiopathogenesis of multiple sclerosis. *Magnes Res* **5**, 295-302 (1992).
115. Sun, Y., Sukumaran, P. & Singh, B.B. Magnesium-Induced Cell Survival Is Dependent on TRPM7 Expression and Function. *Mol Neurobiol* **57**, 528-538 (2020).
116. Sun, Y., Kamat, A. & Singh, B.B. Isoproterenol-Dependent Activation of TRPM7 Protects Against Neurotoxin-Induced Loss of Neuroblastoma Cells. *Front Physiol* **11**, 305 (2020).
117. Chen, S.J. et al. Transient receptor potential ion channel TRPM2 promotes AML proliferation and survival through modulation of mitochondrial function, ROS, and autophagy. *Cell Death Dis* **11**, 247 (2020).
118. Kunert-Keil, C., Bisping, F., Kruger, J. & Brinkmeier, H. Tissue-specific expression of TRP channel genes in the mouse and its variation in three different mouse strains. *BMC Genomics* **7**, 159 (2006).
119. Schlingmann, K.P. et al. Hypomagnesemia with secondary hypocalcemia is caused by mutations in TRPM6, a new member of the TRPM gene family. *Nat Genet* **31**, 166-70 (2002).
120. Schlingmann, K.P. et al. Novel TRPM6 mutations in 21 families with primary hypomagnesemia and secondary hypocalcemia. *J Am Soc Nephrol* **16**, 3061-9 (2005).
121. Guran, T. et al. Clinical and molecular characterization of Turkish patients with familial hypomagnesaemia: novel mutations in TRPM6 and CLDN16 genes. *Nephrol Dial Transplant* **27**, 667-73 (2012).
122. Lainez, S. et al. New TRPM6 missense mutations linked to hypomagnesemia with secondary hypocalcemia. *Eur J Hum Genet* **22**, 497-504 (2014).
123. Woudenberg-Vrenken, T.E., Sukinta, A., van der Kemp, A.W., Bindels, R.J. & Hoenderop, J.G. Transient receptor potential melastatin 6 knockout mice are lethal whereas heterozygous deletion results in mild hypomagnesemia. *Nephron Physiol* **117**, p11-9 (2011).
124. de Baaij, J.H. The art of magnesium transport. *Magnes Res* **28**, 85-91 (2015).
125. Chen, C.C. et al. A small molecule restores function to TRPML1 mutant isoforms responsible for mucolipidosis type IV. *Nat Commun* **5**, 4681 (2014).
126. Dong, X.P. et al. PI(3,5)P(2) controls membrane trafficking by direct activation of mucolipin Ca(2+) release channels in the endolysosome. *Nat Commun* **1**, 38 (2010).
127. Dong, X.P. et al. The type IV mucolipidosis-associated protein TRPML1 is an endolysosomal iron release channel. *Nature* **455**, 992-6 (2008).
128. Slaugenhaupt, S.A. et al. Mapping of the mucolipidosis type IV gene to chromosome 19p and definition of founder haplotypes. *Am J Hum Genet* **65**, 773-8 (1999).
129. Bargal, R. et al. Identification of the gene causing mucolipidosis type IV. *Nat Genet* **26**, 118-23 (2000).

130. Bassi, M.T. et al. Cloning of the gene encoding a novel integral membrane protein, mucolipidin- and identification of the two major founder mutations causing mucolipidosis type IV. *Am J Hum Genet* **67**, 1110-20 (2000).
131. Sun, M. et al. Mucolipidosis type IV is caused by mutations in a gene encoding a novel transient receptor potential channel. *Hum Mol Genet* **9**, 2471-8 (2000).
132. Amir, N., Zlotogora, J. & Bach, G. Mucolipidosis type IV: clinical spectrum and natural history. *Pediatrics* **79**, 953-9 (1987).
133. Bargal, R. et al. Mucolipidosis type IV: novel MCOLN1 mutations in Jewish and non-Jewish patients and the frequency of the disease in the Ashkenazi Jewish population. *Hum Mutat* **17**, 397-402 (2001).
134. Bach, G., Webb, M.B., Bargal, R., Zeigler, M. & Ekstein, J. The frequency of mucolipidosis type IV in the Ashkenazi Jewish population and the identification of 3 novel MCOLN1 mutations. *Hum Mutat* **26**, 591 (2005).
135. Edelmann, L., Dong, J., Desnick, R.J. & Kornreich, R. Carrier screening for mucolipidosis type IV in the American Ashkenazi Jewish population. *Am J Hum Genet* **70**, 1023-7 (2002).
136. Boudewyn, L.C. & Walkley, S.U. Current concepts in the neuropathogenesis of mucolipidosis type IV. *J Neurochem* **148**, 669-689 (2019).
137. Wong, C.O., Li, R., Montell, C. & Venkatachalam, K. Drosophila TRPML is required for TORC1 activation. *Curr Biol* **22**, 1616-21 (2012).
138. Vergarajauregui, S., Connelly, P.S., Daniels, M.P. & Puertollano, R. Autophagic dysfunction in mucolipidosis type IV patients. *Hum Mol Genet* **17**, 2723-37 (2008).
139. Medina, D.L. et al. Lysosomal calcium signalling regulates autophagy through calcineurin and TFEB. *Nat Cell Biol* **17**, 288-99 (2015).
140. Scotto Rosato, A. et al. TRPML1 links lysosomal calcium to autophagosome biogenesis through the activation of the CaMKKbeta/VPS34 pathway. *Nat Commun* **10**, 5630 (2019).
141. Li, X. et al. A molecular mechanism to regulate lysosome motility for lysosome positioning and tubulation. *Nat Cell Biol* **18**, 404-17 (2016).
142. Rosenbaum, T. & Islas, L.D. Molecular Physiology of TRPV Channels: Controversies and Future Challenges. *Annu Rev Physiol* **85**, 293-316 (2023).
143. Vangeel, L. & Voets, T. Transient Receptor Potential Channels and Calcium Signaling. *Cold Spring Harb Perspect Biol* **11**(2019).
144. Su, W. et al. TRPV3: Structure, Diseases and Modulators. *Molecules* **28**(2023).
145. Karki, T. & Tojkander, S. TRPV Protein Family-From Mechanosensing to Cancer Invasion. *Biomolecules* **11**(2021).
146. Asakawa, M. et al. Association of a mutation in TRPV3 with defective hair growth in rodents. *J Invest Dermatol* **126**, 2664-72 (2006).
147. Xiao, R., Tian, J., Tang, J. & Zhu, M.X. The TRPV3 mutation associated with the hairless phenotype in rodents is constitutively active. *Cell Calcium* **43**, 334-43 (2008).
148. Lin, Z. et al. Exome sequencing reveals mutations in TRPV3 as a cause of Olmsted syndrome. *Am J Hum Genet* **90**, 558-64 (2012).
149. Zhong, W. et al. Genotype–Phenotype Correlation of TRPV3-Related Olmsted Syndrome. *J Invest Dermatol* **141**, 545-554 (2021).
150. Ni, C. et al. A novel mutation in TRPV3 gene causes atypical familial Olmsted syndrome. *Sci Rep* **6**, 21815 (2016).
151. Duchatelet, S. et al. A new TRPV3 missense mutation in a patient with Olmsted syndrome and erythromelalgia. *JAMA Dermatol* **150**, 303-6 (2014).
152. Lansky, S. et al. A pentameric TRPV3 channel with a dilated pore. *Nature* **621**, 206-214 (2023).
153. Nadezhdin, K.D. et al. Structural mechanism of heat-induced opening of a temperature-sensitive TRP channel. *Nat Struct Mol Biol* **28**, 564-572 (2021).
154. White, J.P. et al. TRPV4: Molecular Conductor of a Diverse Orchestra. *Physiol Rev* **96**, 911-73 (2016).
155. Cho, T.J. et al. TRPV4-pathy manifesting both skeletal dysplasia and peripheral neuropathy: a report of three patients. *Am J Med Genet A* **158A**, 795-802 (2012).
156. Faye, E., Modaff, P., Pauli, R. & Legare, J. Combined Phenotypes of Spondylometaphyseal Dysplasia-Kozlowski Type and Charcot-Marie-Tooth Disease Type 2C Secondary to a TRPV4 Pathogenic Variant. *Mol Syndromol* **10**, 154-160 (2019).

157. Evangelista, T. et al. Phenotypic variability of TRPV4 related neuropathies. *Neuromuscul Disord* **25**, 516-21 (2015).
158. Taga, A. et al. TRPV4 mutations causing mixed neuropathy and skeletal phenotypes result in severe gain of function. *Ann Clin Transl Neurol* **9**, 375-391 (2022).
159. Rock, M.J. et al. Gain-of-function mutations in TRPV4 cause autosomal dominant brachyolmia. *Nat Genet* **40**, 999-1003 (2008).
160. Deng, Z. et al. Cryo-EM and X-ray structures of TRPV4 reveal insight into ion permeation and gating mechanisms. *Nat Struct Mol Biol* **25**, 252-260 (2018).
161. Nadezhdin, K.D. et al. Structure of human TRPV4 in complex with GTPase RhoA. *Nat Commun* **14**, 3733 (2023).
162. Krakow, D. et al. Mutations in the gene encoding the calcium-permeable ion channel TRPV4 produce spondylometaphyseal dysplasia, Kozlowski type and metatropic dysplasia. *Am J Hum Genet* **84**, 307-15 (2009).
163. Loukin, S., Su, Z. & Kung, C. Increased basal activity is a key determinant in the severity of human skeletal dysplasia caused by TRPV4 mutations. *PLoS One* **6**, e19533 (2011).
164. Muramatsu, S. et al. Functional gene screening system identified TRPV4 as a regulator of chondrogenic differentiation. *J Biol Chem* **282**, 32158-67 (2007).
165. Leddy, H.A., McNulty, A.L., Guilak, F. & Liedtke, W. Unraveling the mechanism by which TRPV4 mutations cause skeletal dysplasias. *Rare Dis* **2**, e962971 (2014).
166. Dicks, A.R. et al. Skeletal dysplasia-causing TRPV4 mutations suppress the hypertrophic differentiation of human iPSC-derived chondrocytes. *Elife* **12**(2023).
167. Nonaka, K. et al. Novel gain-of-function mutation of TRPV4 associated with accelerated chondrogenic differentiation of dental pulp stem cells derived from a patient with metatropic dysplasia. *Biochem Biophys Rep* **19**, 100648 (2019).
168. Landoure, G. et al. Mutations in TRPV4 cause Charcot-Marie-Tooth disease type 2C. *Nat Genet* **42**, 170-4 (2010).
169. Auer-Grumbach, M. et al. Alterations in the ankyrin domain of TRPV4 cause congenital distal SMA, scapuloperoneal SMA and HMSN2C. *Nat Genet* **42**, 160-4 (2010).
170. Deng, H.X. et al. Scapuloperoneal spinal muscular atrophy and CMT2C are allelic disorders caused by alterations in TRPV4. *Nat Genet* **42**, 165-9 (2010).
171. Thibodeau, M.L. et al. Compound heterozygous TRPV4 mutations in two siblings with a complex phenotype including severe intellectual disability and neuropathy. *Am J Med Genet A* **173**, 3087-3092 (2017).
172. Klein, C.J. et al. TRPV4 mutations and cytotoxic hypercalcemia in axonal Charcot-Marie-Tooth neuropathies. *Neurology* **76**, 887-94 (2011).
173. McCray, B.A. et al. Neuropathy-causing TRPV4 mutations disrupt TRPV4-RhoA interactions and impair neurite extension. *Nat Commun* **12**, 1444 (2021).
174. Kwon, D.H. et al. TRPV4-Rho GTPase complex structures reveal mechanisms of gating and disease. *Nat Commun* **14**, 3732 (2023).
175. Bagnell, A.M., Sumner, C.J. & McCray, B.A. TRPV4: A trigger of pathological RhoA activation in neurological disease. *Bioessays* **44**, e2100288 (2022).
176. Wissenbach, U. et al. Expression of CaT-like, a novel calcium-selective channel, correlates with the malignancy of prostate cancer. *J Biol Chem* **276**, 19461-8 (2001).
177. Voets, T. et al. CaT1 and the calcium release-activated calcium channel manifest distinct pore properties. *J Biol Chem* **276**, 47767-70 (2001).
178. Suzuki, Y. et al. TRPV6 Variants Interfere with Maternal-Fetal Calcium Transport through the Placenta and Cause Transient Neonatal Hyperparathyroidism. *Am J Hum Genet* **102**, 1104-1114 (2018).
179. Burren, C.P. et al. TRPV6 compound heterozygous variants result in impaired placental calcium transport and severe undermineralization and dysplasia of the fetal skeleton. *Am J Med Genet A* **176**, 1950-1955 (2018).
180. Masamune, A. et al. Variants That Affect Function of Calcium Channel TRPV6 Are Associated With Early-Onset Chronic Pancreatitis. *Gastroenterology* **158**, 1626-1641 e8 (2020).
181. Shah, I.A. et al. A novel frameshift mutation in TRPV6 is associated with hereditary pancreatitis. *Front Genet* **13**, 1058057 (2022).

182. Oracz, G. et al. Loss of function TRPV6 variants are associated with chronic pancreatitis in nonalcoholic early-onset Polish and German patients. *Pancreatology* **21**, 1434-1442 (2021).
183. Talavera, K. et al. Mammalian Transient Receptor Potential TRPA1 Channels: From Structure to Disease. *Physiol Rev* **100**, 725-803 (2020).
184. Karashima, Y. et al. TRPA1 acts as a cold sensor in vitro and in vivo. *Proc Natl Acad Sci U S A* **106**, 1273-8 (2009).
185. Kremeyer, B. et al. A gain-of-function mutation in TRPA1 causes familial episodic pain syndrome. *Neuron* **66**, 671-80 (2010).
186. Zima, V. et al. Structural modeling and patch-clamp analysis of pain-related mutation TRPA1-N855S reveal inter-subunit salt bridges stabilizing the channel open state. *Neuropharmacology* **93**, 294-307 (2015).
187. Gupta, R. et al. Structural basis of TRPA1 inhibition by HC-030031 utilizing species-specific differences. *Sci Rep* **6**, 37460 (2016).
188. Nirenberg, M.J., Chaouni, R., Biller, T.M., Gilbert, R.M. & Paisan-Ruiz, C. A novel TRPA1 variant is associated with carbamazepine-responsive cramp-fasciculation syndrome. *Clin Genet* **93**, 164-168 (2018).
189. Bali, A. et al. Molecular mechanism of hyperactivation conferred by a truncation of TRPA1. *Nat Commun* **14**, 2867 (2023).
190. Alvarado, M.G., Thakore, P. & Earley, S. Transient Receptor Potential Channel Ankyrin 1: A Unique Regulator of Vascular Function. *Cells* **10**(2021).
191. Lapointe, T.K. & Altier, C. The role of TRPA1 in visceral inflammation and pain. *Channels (Austin)* **5**, 525-9 (2011).
192. Holzer, P. TRP channels in the digestive system. *Curr Pharm Biotechnol* **12**, 24-34 (2011).
193. Gerhold, K.A. & Bautista, D.M. TRPA1: irritant detector of the airways. *J Physiol* **586**, 3303 (2008).

Chapter 2: Molecular mechanism of hyperactivation conferred by a truncation of TRPA1

This work has been previously published in A.P. Bali, S. Schaefer, I. Trier, A. Zhang, L. Kabeche, and C. Paulsen, Molecular mechanism of hyperactivation conferred by a truncation of TRPA1. *Nat Commun* **14**, 2867 (2023) ; DOI https://doi.org/10.1038/s41467-023-38542-1. I have adapted the introduction for this thesis chapter.

2.1 Introduction:

Introduction

The wasabi receptor, TRPA1 (Transient Receptor Potential Ankyrin subtype 1), is a calcium-permeable non-selective homotetrameric cation channel expressed in a subset of primary sensory neurons of the dorsal root, trigeminal, and nodose ganglia where it plays a role in many pain-associated sensory disorders including itch, airway diseases, and inflammation [1-6]. Outside the sensory system, TRPA1 has also been implicated in respiratory, cardiovascular, gastrointestinal, and muscular physiology [3,7-9]. The TRPA1 chemosensor is activated by a chemically diverse panel of environmental and endogenous toxins that fall into two broad categories: electrophiles and non-electrophiles. Electrophile agonists such as Allyl Isothiocyanate (AITC) and Cinnamaldehyde activate the channel by covalently modifying key conserved cysteine residues in the membrane proximal cytoplasmic N-terminus (Fig. 1a, yellow circles) [10-13]. Non-electrophile agonists such as Carvacrol and 2-Aminoethoxydiphenyl Borate (2-APB) bind at distinct sites in the transmembrane domain to promote channel activation [14-17]. TRPA1-activating ligands can also originate endogenously from toxic byproducts of cell stress. For example, some reactive oxygen species (H_2O_2 and superoxide) and 4-Hydroxynonenal (a peroxidated membrane lipid) can bind and activate TRPA1 to illicit pain generation during tissue damage, inflammation, and injury. There is also evidence that mammalian TRPA1 channels serve as noxious cold

receptors [10,18]. Recent cryo-electron microscopy (cryo-EM) TRPA1 structures captured in the closed and electrophile agonist activated states reveal large, allosterically coupled conformational changes in the transmembrane domain and membrane-proximal cytoplasmic N- and C-termini, referred to as the allosteric nexus, highlighting key roles for these regions in channel gating (Fig. 1a-c) [19-21].

The TRPA1 transmembrane domain and allosteric nexus account for only 35% of the total protein sequence (390 of 1119 amino acids) and little is known about the functional impact of the remaining cytoplasmic domains. Situated below the allosteric nexus, TRPA1 houses a large N-terminal ankyrin repeat domain (ARD), in which five membrane proximal ARs form a cage around a C-terminal coiled coil that coordinates a requisite polyanion cofactor (Fig. 1a-c) [19,22]. Interestingly, certain TRPA1 orthologues can be activated by temperature, though the molecular mechanism of temperature sensing is unclear [23]. Studies with TRPA1 species chimeras and point mutations have shown thermosensation can be conferred or tuned through the ARD [24,25]. Whether or how the ARD can communicate to the channel pore remains unknown.

The ability of TRPA1 to bind highly reactive chemical agonists and induce cation flux is widely thought to serve as a protective mechanism- triggering signaling pathways in response to toxic environments or internal injury. In primary sensory neurons, TRPA1 activation causes cell depolarization, initiating action potential signaling cascades from the periphery to the spinal cord, and then to brain, resulting in pain perception [4]. TRPA1-expressing peripheral neurons also innervate non-neuronal tissues, such as blood vessels, GI tract, and respiratory tissues, and release neuropeptides such as substance P, calcitonin gene-related peptide (CGRP) and neurokinin A upon excitation[5]. However, the exact role of TRPA1 activation on other tissue systems in the body has yet to be fully elucidated.

Ion channel mutations with associated pathological conditions, known as channelopathies, provide direct evidence that a channel is relevant to human health, and can illuminate molecular mechanisms and protein domains that govern normal and aberrant channel

function [26]. To date, two human *TRPA1* disease mutations associated with pain disorders have been reported, illustrating a direct role for TRPA1 in pain signaling and marking it as a promising therapeutic target [18,27]. The first characterized TRPA1 channelopathy, which was discovered in patients with the rare, autosomal dominant Familial Episodic Pain Syndrome (FEPS), introduced a missense mutation at N855 [18]. The N855S TRPA1 mutant forms functional channels when expressed alone in heterologous cells characterized by increased inward current at resting membrane potentials with no change to agonist sensitivity. The location of the N855S mutation in a short linker that physically couples two transmembrane helical bundles highlighted a key role for this region in channel gating years before high-resolution TRPA1 structures were available.

The second reported TRPA1 channelopathy has not yet been characterized and a mechanism for how it may alter channel function is unknown. This mutant was discovered in a father-son pair with cramp-fasciculation and other neuronal hyperexcitability-hypersensitivity symptoms including cold hyperalgesia, chronic itch, and asthma that are consistent with aberrant TRPA1 function [27]. This collection of symptoms was referred to as CRAMPT syndrome [27]. The CRAMPT *TRPA1* variant introduces a nonsense mutation at R919 located at the start of the second pore helix, and the resulting R919* TRPA1 protein lacks the final 201 amino acids, including critical elements involved in gating such as the pore-lining transmembrane helix (S6) and components of the allosteric nexus (Fig. 1a-c). In clinical settings, it is frequently assumed that pathologies linked to truncations of channel proteins originate from haploinsufficiency or dominant negative effects. However, such broad assumptions have been challenged as more rigorous studies of truncation proteins reveal numerous mechanisms through which they may underlie hyperexcitability-hypersensitivity phenotypes [28-32]. In this study, we sought to elucidate whether and how the R919* TRPA1 mutant influences channel activity that could explain the observed congenital pain phenotype in patients. Our results expand the functional impact of drastic truncation mutants and provide an impetus for whole exome sequencing of patients with seemingly stochastic pain phenotypes.

2.2 Results:

i. Functional characterization of the R919* TRPA1 mutant

Whole-exome sequencing and co-segregation analysis of a father-son pair with CRAMPT syndrome identified a novel *TRPA1* gene variant consisting of a C to T transition (*c.2755C>T*) [27]. When mapped onto the wild type (WT) human TRPA1 monomer structure, the R919* mutant truncates the last 201 amino acids, or 18% of the protein, removing many important structural and regulatory features including the second pore helix, the ion conduction pathway-lining S6 transmembrane helix and the entire cytoplasmic C-terminus (Fig. 1a-c).

Channelopathies are generally first studied in isolation in heterologous systems to reveal alterations to channel biophysical properties [18,33-36]. For example, the previously reported FEPS-associated TRPA1 mutant (N855S) exhibits enhanced channel activity when expressed in isolation [18]. Since patients carrying the R919* TRPA1 mutant exhibit hypersensitivity-hyperexcitability symptoms, we tested whether R919* TRPA1 inherently possesses any enhanced functional properties. Human R919* TRPA1 was expressed in HEK293T cells or *Xenopus laevis* oocytes, which do not natively express TRPA1, and channel activity was assayed by Fura-2 ratiometric calcium imaging or whole-cell voltage clamp recordings, respectively. HEK293T cells and *Xenopus* oocytes expressing the R919* TRPA1 mutant revealed no activity in the presence of either the electrophile agonist AITC (Fig. 1d-e and 1g-h) and the non-electrophile agonist Carvacrol (Supplementary Fig. 1a), compared to the robust activation observed for WT TRPA1. Additionally, the N855S TRPA1 mutant exhibited enhanced channel activity with a loss of channel rectification and a 3.8-fold increase in inward currents in *Xenopus* whole-cell recordings consistent with its reported gain-of-function properties (Fig. 1d-e, 1g-h, and Supplementary Fig. 1a) [18]. Immunoblot analysis confirmed R919* mutant protein was produced in HEK293T cells and *Xenopus* oocytes, albeit at significantly lower levels than WT or N855S TRPA1 in HEK293T cells (Fig. 1f and i). Nonetheless, WT TRPA1 still formed functional channels

when expressed at a comparable amount to R919* mutant (Supplementary Fig. 1b and c). These results suggest that the lack of inherent activity for R919* TRPA1 is due to its inability to produce functional calcium permeable ion channels, which is unsurprising given the loss of the many key structural and functional domains from this mutant (Fig. 1a-c).

ii. Functional characterization of WT and R919* co-expression

Both R919* and N855S TRPA1 mutants were discovered in heterozygous individuals, where WT and mutant TRPA1 protein could be co-produced [18,27]. This raised the possibility that the R919* mutant mediates its effects by altering co-expressed WT TRPA1 properties. To test whether the R919* mutant affected channel activity in the presence of WT TRPA1, ratiometric calcium imaging was performed on HEK293T cells co-expressing both variants. Cells co-expressing WT and R919* TRPA1 exhibited a robust increase in calcium influx compared to cells expressing WT TRPA1 alone, especially in response to sub-saturating concentrations of AITC (Fig. 2a and Supplementary Fig. 2a), Cinnamaldehyde (Fig. 2b), and Carvacrol (Supplementary Fig. 2b-c). A similar robust increase in whole-cell currents was observed with a sub-saturating AITC concentration in *Xenopus* oocytes co-expressing WT and R919* TRPA1 compared to those expressing WT protein alone (Fig. 2c-d and 3a-b). These channels were inhibited by the canonical TRPA1 antagonists A-967079, HC-030031, and ruthenium red whether they were applied before or after channel activation, consistent with TRPA1-specific responses in both functional assays (Fig. 3a-b and Supplementary Fig. 3a-d). Patients harboring the R919* *TRPA1* mutation experienced symptom relief with the sodium channel blocker carbamazepine (CBZ) raising the possibility that this molecule directly inhibits TRPA1 channels; however, CBZ failed to affect TRPA1 activity at concentrations below 1 mM (Supplementary Fig. 3e-h). Together, these observations suggest that co-expression of WT TRPA1 with the R919* mutant yields hyperactive channels that are sensitive to canonical TRPA1 antagonists but not to CBZ, which likely abolishes pain responses downstream of TRPA1.

Enhanced channel activity at sub-saturating AITC concentration hints that co-expression of WT and R919* TRPA1 affects agonist sensitivity. This is distinct from cells co-expressing WT and N855S TRPA1, which displayed a clear enhancement of calcium influx at both sub-saturating and saturating AITC concentrations (Fig. 2a). While the N855S mutant exhibits increased calcium influx at each agonist concentration, its agonist sensitivity was previously shown to be no different from WT TRPA1 with the electrophile agonist Cinnamaldehyde [18]. Cinnamaldehyde sensitivity was quantified by determining the half maximum effective concentration (EC_{50}) from dose-response curves of cells expressing WT TRPA1 alone or with the N855S or R919* mutants. While no significant change in the Cinnamaldehyde EC_{50} was observed when WT TRPA1 was co-expressed with the N855S mutant (37.7 μM for WT TRPA1 versus 43.1 μM for WT and N855S TRPA1), a 4.8-fold increase in Cinnamaldehyde sensitivity (EC_{50} = 7.8 μM) was observed with R919* TRPA1 co-expression (Fig. 3c). Significantly enhanced agonist sensitivity was also observed with Carvacrol, indicating that the R919* mutant mediates channel hypersensitivity independent of agonist type (Supplementary Fig. 2d).

Collectively, these results reveal that the R919* mutant confers enhanced agonist sensitivity when co-expressed with WT TRPA1, consistent with mutant-mediated sensitization and hyperactivation of TRPA1 channels (Fig. 2, 3 and Supplementary Fig. 2). In contrast, the N855S mutant has no effect on agonist sensitivity. Thus, the mechanism of channel hyperactivity conferred by the R919* mutant is likely distinct from N855S TRPA1.

iii. Effect of R919* mutant on TRPA1 expression, localization, and general cell stress

Channels can become hyperactive through altered protein stability, enhanced plasma membrane trafficking or *via* post-translational channel modifications triggered by general cell stress [37-47]. Immunoblot analysis indicated that expression of R919* had no effect on WT TRPA1 levels, even when performed on cells exhibiting hyperactivity (Supplementary Fig. 4a-c). Similarly, individual or co-expression of WT and R919* TRPA1 had no overt effects on cell viability, reactive oxygen species production, or ER stress induction (Supplementary Fig. 4d-f). It is possible that

R919* TRPA1 causes cell stress not detected by these assays that is capable of generally hypersensitizing ion channels. Thus, R919* TRPA1 was co-expressed with the related capsaicin receptor, TRPV1 and assayed for its effect on human TRPV1 expression, activity, or agonist sensitivity. Akin to WT TRPA1, the R919* mutant had no effect on TRPV1 expression (Supplementary Fig. 4a-b). Moreover, co-expression with R919* TRPA1 conferred no change in capsaicin evoked TRPV1 calcium influx or agonist sensitivity (Supplementary Fig. 5). Finally, surface biotinylation assays revealed that co-expression of R919* had no effect on the amount of WT TRPA1 at the plasma membrane (Fig. 4a-b, compare solid and striped black bars). Together, these data indicate that the R919* mutant does not sensitize channels *via* changes in WT TRPA1 expression, altered plasma membrane localization, or general induction of cell stress.

iv. Effect of WT TRPA1 on R919* mutant expression and localization

Some but not all ion channel truncation mutants result in defects in plasma membrane trafficking [28,42,46,48-52]. Surface biotinylation assays revealed a small plasma membrane population of the R919* mutant, which increased significantly when co-expressed with WT TRPA1 (Fig. 4a-b, compare solid and striped pink bars). Overexpressed Torsin A, an endoplasmic reticulum and perinuclear space-resident AAA+ ATPase, was used as an internal negative control to ensure the R919* mutant labeling was attributed to true plasma membrane localization and not to probe internalization during such assays (Fig. 4a) [53]. We further investigated the R919* mutant plasma membrane localization using immunofluorescence imaging. Deconvolved images of HEK293T cells expressing GFP-tagged R919* TRPA1 or 3xFLAG-tagged WT TRPA1 revealed robust WT TRPA1 localization at the cell surface, while the R919* mutant displayed aberrant localization spreading more diffusely throughout the cytoplasm with minimal plasma membrane localization (Fig. 4c). When co-expressed, 3xFLAG-tagged WT and GFP-tagged R919* TRPA1 both co-localized at the plasma membrane (Fig. 4c). Cross-sectional line scans were performed on raw images of immuno-stained cells, revealing a statistically significant increase in R919* mutant at the cell surface when co-expressed with WT TRPA1 (Fig. 4d and Supplementary Fig. 6a-b).

Notably, co-expression with WT TRPA1 did not increase the R919* mutant protein expression, suggesting enhanced plasma membrane localization is not simply due to stabilization of R919* TRPA1 protein (Fig. 4a and Supplementary Fig. 4a-b).

Interestingly, deconvolved immunofluorescence images of HEK293T cells co-expressing GFP-tagged R919* TRPA1 and 3xFLAG-tagged WT TRPA1 exhibit apparent co-localization of WT and R919* TRPA1 at the plasma membrane (Fig. 4c and e).To further asses the degree of co-localization between WT and R919* TRPA1 at the plasma membrane, line scan analysis of plasma membrane segments was performed on raw images of immuno-stained cells [54,55]. Such analysis on HEK293T cells co-expressing GFP-tagged WT TRPA1 and 3xFLAG-tagged WT or R919* TRPA1 revealed a strong positive correlation between WT subunits that is consistent with known channel homotetramerization, and a positive, albeit weaker correlation between WT and R919* TRPA1 signal at the cell surface (Fig. 4f and Supplementary Fig. 6c-e). Together, these data suggest that co-expression of WT and R919* TRPA1 influences the localization of the R919* mutant, and that both co-localize at the plasma membrane.

v. Physical interaction of WT and R919* TRPA1 in cells

A direct interaction between WT and R919* TRPA1 would explain their observed co-localization in HEK293T cells (Fig. 4) and could structurally impact WT TRPA1 to confer the observed channel sensitization (Fig. 2). To test whether WT and R919* TRPA1 directly interact, pulldown assays were conducted on lysates from cells co-expressing differentially tagged variants of WT or R919* TRPA1. These pulldown assays revealed a robust interaction between MBP-tagged WT TRPA1 and 3xFLAG-tagged WT and R919* TRPA1, but not with 3xFLAG-tagged Kv1.2/2.1 (Kv), a voltage-gated potassium channel (Fig. 5a). Similarly, MBP-tagged R919* TRPA1 was able to efficiently pulldown 3xFLAG-tagged WT and R919* TRPA1, with no interaction observed with 3xFLAG-tagged Kv (Fig. 5a).

A proximity biotin ligation assay was used to further investigate if WT and R919* TRPA1 directly interact in intact cells [56]. BioID2-fused WT TRPA1 or Kv were co-expressed with 3xFLAG-

tagged WT TRPA1, R919* TRPA1, or Kv. Biotinylated 3xFLAG-tagged variants were detected by immunoblot analysis of Neutravidin eluates. These experiments revealed that 3xFLAG-tagged WT and R919* TRPA1 were biotinylated by BioID2-fused WT TRPA1, but not by BioID2-fused Kv (Fig. 5b). Additionally, 3xFLAG-tagged Kv was biotinylated by BioID2-fused Kv, but not by BioID2-fused WT TRPA1 (Fig. 5b). Collectively, our results indicate that WT and R919* TRPA1 engage in a close-range physical interaction in cells.

vi. Biochemical characterization of isolated WT and R919* TRPA1 complexes

The proximity biotinylation results reveal that WT and R919* TRPA1 subunits are within a range of ~10 nm, approximately the width of a single TRPA1 channel [19]. This labeling radius is consistent with proximity of adjacent WT and R919* TRPA1 homotetramers or with co-assembly of WT and R919* TRPA1 subunits into heteromeric complexes. While TRPA1 is the only member of the TRPA sub-family of mammalian TRP ion channels, heteromerization within the multi-member TRPV, TRPC, TRPP, and TRPML sub-families is well characterized [57-67], raising the possibility that WT and R919* TRPA1 subunits could heteromerize in a similar manner. Indeed, such heteromerization of WT subunits with alternative splice variants or single nucleotide polymorphisms has been proposed for both TRPV1 and TRPA1 [68,69].

Fluorescence size exclusion chromatography (FSEC) was used to differentiate between association of adjacent homotetramers versus assembly of heteromeric complexes as these assemblies are of very different sizes (*e.g.,* ~1000 KD versus ~500 KD, respectively) and would yield distinct elution profiles [70]. GFP- or 3xFLAG-tagged WT or R919* TRPA1 were co-expressed in HEK93T cells in specific combinations, complexes were isolated by anti-FLAG immunoprecipitation, and eluates were analyzed by FSEC to monitor the associated GFP-tagged subunits. The elution profile from GFP WT TRPA1 co-purified with 3xFLAG WT TRPA1 revealed a monodisperse peak consistent with a TRPA1 tetramer, as previously reported (Fig. 5c, black trace) [19]. These complexes were of similar size to homotetrameric GFP-WT TRPA1 channels suggesting the heterogeneity in stoichiometry of a large GFP tag and a small 3xFLAG tag had

minimal impact on the elution profile (Supplementary Fig. 7a). Complexes purified from cells co-expressing GFP- and 3xFLAG-tagged R919* TRPA1 revealed a monodisperse peak that eluted slightly before WT TRPA1 homotetramers (Fig. 5c, teal trace). Interestingly, complexes isolated from cells co-expressing GFP-tagged WT TRPA1 and 3xFLAG-tagged R919* TRPA1 revealed a monodisperse peak that elutes slightly earlier than WT or R919* homotetramers (Fig. 5c, pink trace). Immunoblot analysis of FSEC fractions from the TRPA1 (•) and free FLAG peptide (∞) peaks confirmed the presence of 3xFLAG-tagged variants in the TRPA1 peaks (Fig. 5d). While fluorescent signal in these experiments was only attributed to one subunit type, multicolor FSEC experiments can be used to characterize heteromeric membrane protein assemblies [71]. Dual color FSEC analysis of Ni^{2+}-FLAG tandem-purified complexes from cells co-expressing 8xHis-mCerulean-tagged WT and FLAG-mVenus-tagged R919* TRPA1 revealed an overlapping peak (•) in both the mCerulean and mVenus channels consistent with TRPA1 peaks in Fig. 5 (Supplementary Fig. 7b-c). Importantly, mCerulean and mVenus have non-overlapping spectral properties (Supplementary Fig. 7d-e), confirming that the TRPA1 peak detected at both wavelengths from tandem-purified samples must contain both TRPA1 variants.

To further interrogate the oligomer state of WT-R919* complexes, Strep-FLAG tandem affinity purification was performed on lysates from HEK293T cells expressing dual-tagged FLAG-MBP- or Strep-MBP-WT or R919* TRPA1 variants and analyzed by Blue Native PAGE. These results also suggest WT-R919* complexes resemble WT TRPA1 homotetramers in size (Supplementary Fig. 7f). Notably, R919* homomers were not resolved after tandem purification by this method, perhaps suggesting their relative instability and/or revealing transient interactions between R919* TRPA1 subunits (Supplementary Fig. 7f).

There are three possible stoichiometries for the assembly of WT and R919* TRPA1 subunits into heterotetramers: 3:1, 2:2, or 1:3 WT:R919* TRPA1 subunits. To estimate subunit stoichiometry, immunoblot analysis was performed on Strep-FLAG tandem-purified WT-R919* TRPA1 heteromeric complexes with a common MBP-tag on both subunit types (Fig. 5e). The

common MBP-tag readout allows direct comparison of WT and R919* TRPA1 band intensities within isolated assemblies, yielding an average WT:R919* TRPA1 subunit ratio of 1:1.3 (Fig. 5f). This subunit ratio is inconsistent with a single WT-R919* TRPA1 heteromer composition. Together, these data suggest that WT and R919* TRPA1 subunits co-assemble into stable, tetrameric channel-sized complexes of heterogeneous subunit stoichiometries.

vii. R919* TRPA1 subunits comprise functional channels

Co-assembly of R919* and WT TRPA1 subunits into channel-sized heteromers raises the possibility that these complexes form functional channels that are a direct cause of the observed hyperactivity. Electrophile agonist complementation assays were performed to investigate whether R919* TRPA1 subunits reside within functional channels and contribute to activity. AITC activates TRPA1 by covalent modification of three conserved cysteine residues in the cytoplasmic N-terminus (*e.g.,* C621, C641, and C665) which are all present in both WT and R919* TRPA1 subunits (Fig. 1a and 5a) [11,13]. Mutation of these three cysteines to serine (3CtoS FL) on WT TRPA1 yields a full-length construct with greatly reduced AITC sensitivity (Fig 6b and Supplementary Fig. 8a), while preserving activation by the non-electrophile agonist Carvacrol (Supplementary Fig. 8b). To test whether the R919* mutant subunits contribute to functional channels, the R919* variant was co-expressed with 3CtoS FL TRPA1 in HEK293T cells and assayed for AITC-evoked activity compared to 3CtoS FL TRPA1 alone. Such experiments revealed that 3CtoS FL TRPA1 AITC sensitivity could be significantly restored by co-expression with the R919* mutant, suggesting that R919* subunits can complement the loss of reactive residues (Fig. 6b, compare teal and dark purple bars, Supplementary Fig. 8a-b). This functional rescue was contingent on the R919* mutant subunits themselves containing the three cysteine residues since co-expression of 3CtoS FL TRPA1 with the 3CtoS R919* mutant failed to enhance AITC-evoked calcium influx (Fig. 6b, lavender bar, Supplementary Fig. 8a-b). Results from whole-cell voltage clamp experiments in *Xenopus* oocytes were even more striking since a 3CtoA FL TRPA1 variant exhibited almost no AITC-evoked currents at all (Fig. 6c and Supplementary Fig.

8c). Non-electrophile agonist 2-APB did still evoke currents from oocytes expressing 3CtoA FL TRPA1 that were comparable to WT TRPA1 (Supplementary Fig. 8c and g). AITC sensitivity was restored when 3CtoA FL TRPA1 was co-expressed with the R919* mutant but not when it was co-expressed with the 3CtoA R919* mutant (Fig. 6d-e and Supplementary Fig. 8d-f). Together, these results support direct co-assembly of WT and R919* TRPA1 subunits into functional heteromeric channels acting at the plasma membrane with concerted activation among subunits. Moreover, these results demonstrate that electrophile-mediated channel activation can originate from the R919* mutant subunit(s).

viii. Source of R919* TRPA1-conferred hyperactivity

While AITC sensitivity of 3CtoS or 3CtoA FL TRPA1 could only be restored by R919* TRPA1 subunits with intact cysteines, co-expression of WT TRPA1 with the R919* or 3CtoS R919* mutants conferred similar hyperactivity (Fig. 6b, compare black, pink, and blue bars). These results indicate that the R919* mutant does not require intrinsic agonist sensitivity to modulate WT TRPA1 function and suggest that structural and/or regulatory features lost due to truncation contribute to channel hyperactivity.

TRPA1 structural features that are missing in the R919* mutant can be subdivided into three discrete regions: the second pore helix and S6 transmembrane helix, the latter of which forms the lower gate; the TRP domain and subsequent β-strand in the membrane-proximal cytoplasmic C-terminus as part of the allosteric nexus important for channel gating; and the remaining cytoplasmic C-terminus including an interfacial helix possibly involved in lipid regulation and the distal coiled coil, which forms the core intracellular inter-subunit interaction and coordinates a requisite polyanion cofactor (Fig. 1a-c) [19,20]. To analyze the contribution of specific functional domains to the conferred channel sensitization, a suite of C-terminal truncation mutants was generated that exclude the coiled coil and interfacial helix (Δ1011-1119), the complete cytoplasmic C-terminus (Δ969-1119), and the S6 transmembrane helix and cytoplasmic C-

terminus (Δ934-1119) (Fig. 7a and Supplementary Fig. 9a-b). Akin to R919* TRPA1, these C-terminal truncations failed to form functional channels when expressed alone in HEK293T cells or *Xenopus* oocytes, suggesting that key regions in the distal cytoplasmic C-terminus are required to support proper channel function (Fig. 1g-i and Supplementary Fig. 9c). This inactivity is seemingly not due to poor expression or failure of the C-terminal truncations to traffic to the plasma membrane (Fig. 1i and Supplementary Fig. 9d). Each C-terminal truncation could additionally immunoprecipitate WT TRPA1 when co-expressed, suggesting that they may also co-assemble with WT subunits into heteromeric complexes (Supplementary Fig. 10a). Ratiometric calcium imaging analysis of WT TRPA1 co-expressed with the partial (Δ1011-1119) and complete (Δ969-1119) cytoplasmic C-terminus truncations revealed a noticeable (though not statistically significant) increase in AITC sensitivity (Fig. 7b-c, light and medium pink bars). However, the additional truncation of the S6 transmembrane helix (Δ934-1119) conferred robust and significant channel hyperactivity when co-expressed with WT TRPA1 (Fig. 7b-c, pink bar). To account for any changes in WT TRPA1 expression for functional experiments, AITC sensitivity was further normalized to WT TRPA1 expression (Supplementary Fig. 10b). These results demonstrate that sequential truncation of the cytoplasmic C-terminus and the S6 transmembrane helix from TRPA1 subunits provide stepwise contributions to R919* TRPA1-conferred channel hyperactivity with loss of the S6 transmembrane helix being largely responsible for heteromeric channel hyperactivation.

ix. Calcium handling and pore architecture of heteromeric channels

The TRPA1 pore is formed by an S6 transmembrane helix that contains the lower gate and lines the ion permeation pathway as well as an outer pore domain comprised of two extracellular pore helices separated by a loop housing the selectivity filter (Fig 1a-b). This loop contains an aspartate (D915 in hTRPA1) crucial for calcium permeation and the two pore helices structurally orient the loop along the ion conduction pathway [19,72]. Since the S6 transmembrane

helix and the second pore helix are truncated in R919* TRPA1, it is conceivable that WT-R919* heteromeric channels display altered ion selectivity, channel conductance, and/or gating kinetics. Any of these altered properties could account for the observed channel hyperactivity.

To directly assess truncation mutant-mediated changes to channel properties, whole-cell voltage clamp recordings of *Xenopus* oocytes expressing WT TRPA1 with R919* TRPA1 (partially intact outer pore) or Δ934-1119 TRPA1 (fully intact outer pore) were compared in the absence or presence of extracellular calcium. *Xenopus laevis* oocytes endogenously express calcium-activated chloride channels, which could complicate such recordings. However, these channels produce small currents [73,74] and canonical calcium regulation profiles have previously been reported for TRPA1 channels in this heterologous system [24] suggesting endogenous channel contribution is minor and within error. When calcium was excluded from the bath solution, AITC evoked approximately 2-fold larger outward currents (recorded at +80 mV) from oocytes co-expressing WT and R919* or Δ934-1119 TRPA1 compared to those expressing WT TRPA1 alone (Fig. 3a-b and 8a-d). Larger inward currents (recorded at -80mV) were also typically observed in oocytes co-expressing WT and TRPA1 truncations in calcium-free conditions, though these were not statistically significant (Fig. 8a-d, timepoint i). Calcium causes rapid potentiation of TRPA1 channels [72], which was observed in each channel population (Fig. 8a-c, timepoint ii) and potentiated currents were larger from oocytes co-expressing WT TRPA1 and a truncation construct (Fig. 8d and Supplementary Fig. 10f) despite no significant change to potentiation kinetics (Supplementary Fig. 10g). Specifically, peak outward current amplitudes from oocytes co-expressing WT and R919* or Δ934-1119 TRPA1 were approximately 3-fold larger than from those expressing WT TRPA1 only. Inward peak current amplitudes were also significantly enhanced with 5.3- and 4.8-fold larger currents from oocytes co-expressing WT and R919* or Δ934-1119 TRPA1 than WT TRPA1 only, respectively. These larger currents were not attributed

to an increase in WT TRPA1 expression and thus reflect a true increase in channel activity (Fig. 8e).

Calcium potentiation evoked a more linearized current-voltage relationship (*e.g.,* reduced outward rectification) in all TRPA1 expression conditions consistent with significantly increased inward currents (Fig. 8a-c, blue I/V curves, and Supplementary Fig. 10c-e). For WT TRPA1 channels, calcium addition reduced outward rectification from 3.2-fold to 2.7-fold (calculated from $I_{outward}/I_{inward}$). Notably, this reduction in outward rectification with calcium was even more pronounced from oocytes co-expressing WT and R919* (2.4-fold to 1.8-fold upon calcium addition) or Δ934-1119 TRPA1 (3.1-fold to 1.7-fold upon calcium addition), reflective of a larger boost to their inward currents (Fig. 8a-c and Supplementary Fig. 10d-e). Taken together, these data suggest calcium critically contributes to mutant-conferred channel hyperactivity, characterized by significantly larger boosts in calcium-mediated inward currents compared to WT TRPA1 channels.

Following rapid channel potentiation, extracellular calcium triggers slow TRPA1 desensitization [72], which was observed in oocytes expressing WT TRPA1 alone and in those co-expressing WT and R919* or Δ934-1119 TRPA1 (Fig. 8a-c, following timepoint ii). As with potentiation, co-expression of WT TRPA1 with the R919* mutant did not significantly affect desensitization kinetics (Supplementary Fig. 10h). Though not statistically significant, potentiation and desensitization rates were typically faster in oocytes co-expressing WT and R919* TRPA1, suggesting that gating kinetics may be altered in WT-R919* heteromeric TRPA1 channels (Fig. 8a-c and Supplementary Fig. 10g-h). Indeed, the former is consistent with calcium imaging experiments that revealed an enhancement in the time to maximal response at a sub-saturating AITC concentration (Supplementary Fig. 2a). It is likely that more pronounced effects on gating kinetics in the WT-R919* heteromers are masked by the functional co-production of WT TRPA1 homotetramers in these cells. Nonetheless, the observation that channels from oocytes co-

expressing WT and R919* TRPA1 or Δ934-1119 TRPA1 exhibit calcium-mediated potentiation and desensitization indicate that these properties are not affected by loss of the S6 transmembrane helix (R919* and Δ934-1119) nor part of the outer pore domain (R919*) in the truncated TRPA1 subunits (Fig. 8a-c). This suggests that elements critical for TRPA1 calcium regulation are either retained in both truncation mutants or that these elements are lost but their presence in the associated WT TRPA1 subunits is sufficient to confer potentiation and desensitization.

The significantly enhanced current amplitudes in oocytes co-expressing WT and R919* TRPA1 raise the possibility that WT-R919* heterochannels exhibit enhanced calcium permeability perhaps due to changes in pore architecture (Fig. 8d). To probe the pore architecture, inward currents were measured with the large monovalent cation *N*-methyl-D-glucamine ($NMDG^+$) as the predominant extracellular cation. WT TRPA1 typically exhibits low $NMDG^+$ permeability upon acute exposure to agonists [75]. Consistently, WT TRPA1 channels exhibited only small (30 nA) inward currents following activation by AITC while channels from oocytes co-expressing WT and R919* TRPA1 produced significantly larger currents (190 nA) (Fig. 8f-g, timepoint iii), indicating that the WT-R919* TRPA1 channel pore can better accommodate bulky $NMDG^+$ cations. This strongly suggests that the WT-R919* channel pore is larger than that in WT TRPA1 channels. When calcium was added to the extracellular solution, inward currents in both populations increased with significantly larger inward currents from oocytes co-expressing WT and R919* TRPA1 (Fig. 8f-g, timepoint iv). Since $NMDG^+$ permeation was low in oocytes expressing WT or WT and R919* TRPA1, the increase in currents above $NMDG^+$ currents are likely predominantly carried by calcium ions and thus these recordings can provide information on relative calcium permeability. Peak inward currents from oocytes co-expressing WT and R919* were approximately 4-fold higher than those from cells only expressing WT TRPA1 suggesting that WT-R919* TRPA1 channels exhibit enhanced calcium permeability. These larger currents were

not attributed to an increase in WT TRPA1 expression in co-injected oocytes and thus reflect a true increase in channel activity (Fig. 8h).

Collectively, these results reveal that channels from oocytes co-expressing WT and R919* TRPA1 exhibit enhanced inward and outward currents especially in the presence of calcium, a more linearized current-voltage relationship with calcium, increased pore size, and enhanced calcium permeability compared to WT TRPA1 alone. These results are consistent with the R919* mutant subunits affecting channel pore architecture and ion permeation. Interestingly, the N855S TRPA1 channelopathy also exhibits enhanced inward currents, however, this property can be detected without calcium (Fig. 1g-h) suggesting the N855S and R919* mutants affect TRPA1 channels through very distinct mechanisms. Endogenously, extracellular environments contain 1.5-2 mM calcium [76] and TRPA1 initiates pain signals by facilitating inward currents to sensory neurons from their resting membrane potential (~-60 to -75 mV) [77]. Thus, the significant enhancement of inward currents introduced by both N855S and R919* TRPA1 mutants should be capable of promoting neuronal excitability.

x. Conservation of mutant-conferred hyperactivity and broad applicability

Negative stain electron microscopy of thirteen TRPA1 species orthologues has previously revealed a conserved channel architecture, which raises the possibility that the CRAMPT-associated TRPA1 mutant may similarly confer channel hyperactivity in other orthologues [19]. Analogous CRAMPT-associated mutants were generated for mouse TRPA1 (R922*) and zebrafish TRPA1 isoform a (Q914*), which share 80% and 49% sequence identity to the human TRPA1 orthologue, respectively (Supplementary Fig. 11a). Expression of the mouse R922* or zebrafish Q914* TRPA1 mutants alone in HEK293T cells failed to form functional channels (Supplementary Fig. 11b-c). However, they conferred significantly enhanced AITC sensitivity when co-expressed with their WT TRPA1 counterparts (Fig. 9a-b and Supplementary Fig. 11b-

c), suggesting evolutionary conservation of structural features in the S6 transmembrane helix and cytoplasmic C-terminus that contribute to this mechanism of hyperactivity.

To test whether mutant-conferred hyperactivity is conserved across the TRP channel family, truncation mutants analogous to the ∆934-1119 human TRPA1 mutant lacking the S6 transmembrane helix and the cytoplasmic C-terminus were generated for TRPV1 (F656*) and the menthol receptor, TRPM8 (I955*). While TRPA1, TRPV1, and TRPM8 share global structural elements, they possess very structurally distinct outer pore domains and cytoplasmic domains (Supplementary Fig. 12a). Like the analogous ∆934-1119 TRPA1 truncation, neither F656* TRPV1 nor I955* TRPM8 formed functional channels when expressed alone in HEK293T cells despite expressing as well as their WT counterparts (Supplementary Fig. 12b-e). When co-expressed with their WT partners, F656* TRPV1 significantly enhanced capsaicin sensitivity (Fig. 9c and Supplementary Fig. 12b) while the I955* TRPM8 variant had no impact on menthol-evoked activity (Fig. 9d and Supplementary Fig. 12d). Thus, removal of the S6 transmembrane helix and cytoplasmic C-terminus similarly promotes TRPV1 channel sensitization in TRPV1 heteromers. This is consistent with previously reported enhanced channel activity conferred by a TRPV1 alternative splice variant that removes the part of the cytoplasmic C-terminus responsible for channel regulation by phosphatidylinositols [68,78]. In contrast, removal of these domains failed to confer channel hyperactivity to TRPM8, which is consistent with previous work that demonstrated components of the cytoplasmic C-terminus including the coiled coil are necessary for subunit oligomerization [52,79]. Collectively, these results illustrate analogous R919* or ∆936 TRPA1 mutants can be applied to other receptors to confer channel sensitization if their cytoplasmic C-terminal domains are not required for channel assembly.

2.3 Discussion:

Gain-of-function channelopathic mutations provide a unique opportunity to understand how changes in channel structure cause aberrant function. Most commonly, gain-of-function

channelopathies introduce missense mutations in key structural regions that alter channel gating [18,31,32,80]. Far rarer are truncation channelopathies that lead to gain-of-function, of which only two have been previously characterized [28,30]. In contrast to these variants, CRAMPT-associated R919* *TRPA1* is a drastic nonsense channelopathic mutation that lacks core parts of the ion conduction pathway machinery and the complete cytoplasmic C-terminus. Astonishingly, we found that the R919* mutant conferred gain-of-function when co-expressed with WT TRPA1 subunits. Our data support a model where WT and R919* TRPA1 subunits co-assemble to form hyperactive heteromeric ion channels characterized by enhanced sensitivity to multiple agonist types and by altered pore architecture and increased inward calcium permeation (Fig. 10a). Across neuronal and non-neuronal tissues expressing TRPA1, this increased sensitivity and inward ion conduction could account for the hyperexcitability-hypersensitivity observed in CRAMPT syndrome patients (*e.g.*, cold hyperalgesia, parasthesis, itch, asthma, and GI reflux). Importantly, we found these channels are sensitive to a suite of TRPA1 antagonists, which may illuminate a therapeutic path forward for CRAMPT and other TRPA1 channelopathic disorders.

Across neuronal and non-neuronal tissues expressing TRPA1, increased sensitivity and inward ion conduction could account for the hyperexcitability-hypersensitivity observed in CRAMPT syndrome patients (e.g., cold hyperalgesia, parasthesis, itch, asthma, and GI reflux). It is intuitive that TRPA1 hyperactivation should lead to pain phenotypes - cation influx in sensory neurons would readily trigger depolarization in nociceptor neurons and cause increased pain signaling. Indeed, CRAMPT patients experience full or partial alleviation of pain and other symptoms when treated with the voltage-gated channel blocker carbamazepine[27], indicating that TRPA1 may contribute to disease phenotypes by depolarizing cells. Outside the pain pathway, symptoms such as muscle fasciculations, GI distress, cardiac palpitations, and respiratory sensitivity are also observed in CRAMPT patients. In theory, the 4-fold increase in TRPA1 Ca^{2+} permeability observed in the CRAMPT genetic background could explain non-sensory symptoms. For example, TRPA1-expressing neurons innervating the arterial smooth muscle cells also

contain the potent vasodilator CGRP[92]. When activated, TRPA1 permeates calcium into the nerve terminal, facilitating CGRP release onto smooth muscle cells, resulting in vasodilation[92,93]. Arterial vasodilation can reflexively cause tachycardia and palpitations[94], both of which are reported symptoms in CRAMPT patients. Another system where TRPA1-mediated Ca^{2+} influx could play a key role in symptom development is in the gastrointestinal system. Within enterochromaffin and enteroendocrine cells, TRPA1-induced Ca^{2+} influx leads to increased secretion of serotonin and cholecystokinin, which facilitate increased gut motility and satiety signals[95,96]. Importantly, TRPA1-expressing nociceptor neurons innervating the intestines can, upon TRPA1 Ca^{2+} influx, release inflammatory mediators substance P and CGRP in the GI tract, underlying irritable bowel syndrome and gastritis[97,98] – both of which are present in CRAMPT patients.

Our model requires that some WT-R919* TRPA1 heteromeric complexes form functional channels at the plasma membrane (Fig. 10a). Two independent lines of evidence directly support this model. First, R919* TRPA1 restored electrophile agonist sensitivity to full-length TRPA1 subunits lacking the requisite cysteine residues indicating that R919* subunits are incorporated into these channels (Fig. 6). Second, channels formed in cells co-expressing WT and R919* TRPA1 exhibited a roughly 6-fold increase in current carried by the bulky monovalent cation $NMDG^{+}$ compared to WT TRPA1 (Fig. 8f-g). This is consistent with a larger ion channel pore in WT-R919* TRPA1 complexes expected due to the loss of the S6 ion conduction pathway-lining helix from the incorporated R919* subunits. This larger ion channel pore in WT-R919* heteromeric complexes may also account for our observed increase in calcium permeation from cells co-expressing WT and R919* TRPA1.

High-resolution TRPA1 structures solved in distinct functional states allow us to hypothesize how the R919* truncation may enhance channel activity [19-21]. TRPA1 activation is associated with large conformational changes throughout the protein structure including in subdomains lost in the R919* mutant (Fig. 10b, green arrows). These conformational rearrangements may serve as energetic barriers to gating when the channel is in the closed state

and loss of key structural elements from R919* subunits may lower the energetic bar for gating in WT-R919* heteromeric complexes by reducing structural constraints that oppose active conformations. Indeed, C-terminal regions have been found to oppose gating in some ion channels [28,81-83]. Consistently, we found that removal of the cytoplasmic C-terminus conferred channel sensitization with a significant boost in activity observed with the additional loss of the S6 transmembrane helix (Fig. 7b-c). This release in structural tension from R919* TRPA1 subunits would be expected to facilitate channel gating in WT-R919* heteromeric complexes originating from cytoplasmic (*e.g.,* AITC and Cinnamaldehyde) or transmembrane (*e.g.,* Carvacrol) ligand binding sites and may explain these channels' enhanced sensitivity to all agonists tested at sub-saturating concentrations. We also show that these truncated C-terminal regions play a similar role in TRPA1 orthologues and in the related TRPV1, suggesting evolutionary conservation of the proposed gating dynamics.

The ability of R919* TRPA1 subunits to initiate electrophile agonist gating of heteromeric channels in our complementation assays suggest channel gating insights (Fig. 6). R919* TRPA1 subunits lack certain key structural features (*e.g.*, the TRP domain and the S6 helix) that communicate this signal to the channel pore (Fig. 10b). However, channel activation is also accompanied by contraction of both the membrane proximal ARD, which forms a cage around the coiled coil, and the coiled coil (Supplementary Fig. 13). Interestingly, coiled coil dynamics have been shown to play a critical role in regulating bacterial voltage-gated sodium channels and TRPM8 [81,84]. Though R919* TRPA1 subunits lack the coiled coil helix, contraction of the R919* mutant's ARD may be "felt" by the coiled coil(s) of associated WT subunits (Fig. 10b, purple arrow 1) and communicated to the pore through their membrane proximal ARD (Fig. 10b, purple arrow 2). Thus, the membrane proximal ARD and coiled coil may represent an intracellular point of intersubunit communication that facilitates concerted channel gating akin to the transmembrane domain. Such a role for ARD dynamics in channel gating has exciting implications for how

thermosensation may be mediated by some TRPA1 species orthologues where the ARD has been shown to play a critical role [24,25].

Functional WT-R919* heteromeric complexes appear to retain TRPA1 calcium regulation characterized by rapid potentiation followed by slow desensitization, which raises interesting questions about this important regulatory mechanism (Fig. 8) [72]. To date, four distinct TRPA1 domains have been proposed to contribute to calcium regulation: a N-terminal EF hand, a S2-S3 calcium binding site, a C-terminal acidic cluster, and a C-terminal calmodulin binding domain [21,85-87]. The first two motifs are retained in R919* TRPA1 subunits while the two C-terminal motifs are lost. We observed typical calcium regulation of functional channels in oocytes co-expressing WT and R919* TRPA1 without significant changes to gating kinetics (Fig. 8). This may indicate either that structural features required for calcium-driven potentiation and/or desensitization are retained in the R919* subunits or that associated WT subunits are sufficient to mediate this regulation due to domain-swapped assembly in the transmembrane domain and concerted channel gating [88]. Future work with a homogenous population of WT-R919* TRPA1 complexes will reveal whether and how calcium regulation is affected in these channels.

We found that WT-R919* TRPA1 complexes can form with a mixture of subunit stoichiometries, and future work is needed to determine which of these stoichiometries form in cells to contribute to the CRAMPT syndrome phenotype (Fig. 10a). It is likely that specific WT-R919* TRPA1 heteromer complexes have greatly altered channel properties (*e.g.,* gating kinetics, ion permeation, agonist sensitivity) that are functionally diluted by the co-production of WT homotetrameric channels in the same cells in our whole-cell experiments (Fig. 10a). Notably, this heterogenous channel population is likely reflective of the native neuronal environment in CRAMPT syndrome patients and our observed channel sensitization may represent not only an increase in activity of WT-R919* heteromeric complexes, but also a calcium-driven potentiation of co-expressed WT TRPA1 channels. Thus, future work will require production of a homogenous population of WT-R919* TRPA1 complexes with defined subunit stoichiometries and

compositions that can be studied in isolation. Such homogeneous preparations will also facilitate structural determination of WT-R919* TRPA1 complexes that could directly reveal how these subunits alter channel architecture to promote sensitization.

The R919* TRPA1 mutant was the first reported genetic link to cramp-fasciculation syndrome (CFS), a rare muscle hyperexcitability syndrome that occurs spontaneously in patients with no family history of the condition. In clinical settings, truncation mutations are often overlooked as they predominantly confer dominant negative or loss-of-function phenotypes [49,89-91]. Thus, our discovery that the R919* TRPA1 mutant confers gain-of-function when co-expressed with WT subunits is noteworthy and distinct. Our findings also expand the possible physiological impact of seemingly nonfunctional truncation mutants, alternative splice variants, or other single nucleotide polymorphisms that are endogenously co-expressed with WT protein and demonstrate that it is critical to consider the genotype of patients where such gene permutations are identified. Finally, our work highlights that spontaneous channelopathic mutations may be more prevalent in the human population than previously appreciated, which provides an impetus for genetic analysis of patients with CFS, CRAMPT, or other stochastic pain syndromes.

2.4 Materials and Methods:

Cloning and Protein Expression

Point mutations to generate the CRAMPT-associated mutant premature stop codon (R919* for human TRPA1, R922* for mouse TRPA1, and Q914* for zebrafish TRPA1a), truncation constructs for TRPV1 (F656*) and TRPM8 (I955*), and electrophile incompetent variants were implemented using QuikChange Lightning site-directed mutagenesis. Larger deletions of C-terminal domains of TRPA1 were accomplished via InFusion EcoDry cloning. For calcium imaging experiments, untagged human TRPA1 in a combined mammalian/oocyte expression vector pMO (modified from pcDNA3 - obtained from David Julius) or 3xFLAG-tagged TRPA1, TRPV1, or TRPM8 in p3xFLAG-eYFP-CMV-7.1 vector were used. WT and inactive human TRPA1 variants

were subcloned into CaM/pIRES2-eGFP (Addgene) at the NheI/EcoRI sites to generate a positive fluorescent readout for transfection in singly transfected calcium imaging studies. For expression in *Xenopus laevis* oocytes, 3xFLAG-hTRPA1 variant genes were subcloned into the combined mammalian/oocyte expression vector pMO prior to generating cRNAs.

Human embryonic kidney cells (HEK293T, ATCC CRL-3216) were cultured in Dulbecco's modified Eagle's medium (DMEM; Invitrogen) supplemented with 10% calf serum for all experiments except immunofluorescence imaging where 10% FBS was used, and 1x Penicillin-Streptomycin (Invitrogen) at 37°C and 5% CO_2. Cells were grown to ~85-95% confluence before splitting for experiments or propagation.

Plasmids were transfected into HEK293T cells with jetPRIME (Polyplus) according to manufacturer protocols and cells were used for all experiments within 48 hours of transfection.

Ratiometric Calcium Imaging

After 40-48 hours transient transfection, HEK293T cells were loaded with 10 µg/mL Fura-2-acetoxymethylester (Thermo Fisher) in physiological Ringer's buffer (in mM: 120 NaCl, 5 KCl, 2 $CaCl_2$, 25 $NaHCO_3$, 1 $MgCl_2$, 5.5 HEPES, 1 D-glucose, pH 7.4; Boston BioProducts) for ratiometric calcium imaging. Activity of TRPA1 was monitored using a Zeiss Axio Observer 7 inverted microscope with a Hamamatsu Flash sCMOS camera at 20x objective. Dual images (340 and 380 nm excitation, 510 nm emission) were collected and pseudocolour ratiometric images were monitored during the experiment (Metafluor software). Following agonist application, cells were imaged for 45-100 s.

AITC, Carvacrol, Capsaicin, Menthol, and Cinnamaldehyde were all purchased from Sigma and were freshly prepared as stocks at 4x the desired concentration in 1% DMSO and Ringer's solution. 5 µL 4x agonist was added to wells containing 15 µL Ringer's solution to give the final 1x desired concentration. For the antagonist experiments in Fig. S3, cells were pre-treated with Ringer's solution containing A-967079 (Tocris), HC-030031 (Tocris), Ruthenium red

(Sigma), or Carbamazepine (Sigma) at the desired concentration for 1 min and activated with a 4x AITC solution containing 4x antagonist to maintain antagonist concentration. When quantifying calcium influx responses for dose-response curves, each experimental replicate at each agonist concentration was an average response from 30 cells, with three separate replicates (*e.g.*, 90 total cells per agonist concentration). For all other experiments, a minimum of 60-90 cells were selected per condition per replicate for ratiometric fluorescence quantification in Metafluor v7.8.13 with 3-5 replicates per experiment. Pre-active cells were excluded from quantification and background signal was quantified from un-transfected cells and subtracted from quantified cells for normalization. Unless reported in arbitrary units (arb. units), all data were normalized by the maximum response evoked for that transfection condition by 10x agonist (100 uM for human and mouse TRPA1, and 1 mM for zebrafish TRPA1), 200x agonist (200 μM Menthol), or 1000x agonist (1 μM Capsaicin). When validation of equivalent expression was required, the imaged cells were lysed, and quantitatively immunoblotted for 3xFLAG-tagged TRPA1 as detailed below. For inactive variants or antagonist-treated TRPA1 that did not exhibit appreciable calcium influx, constructs in the pIRES-eGFP vector were transfected in HEK293T cells. Fluorescence images were collected with a GFP filter after ratiometric calcium imaging, which allowed selection of GFP positive cells for subsequent quantification. R919* hTRPA1 data was quantified as above.

Oocyte Electrophysiology

pMO vectors carrying 3xFLAG-tagged hTRPA1 constructs were linearized with PmeI, cRNAs were generated by *in vitro* transcription with the mMessage mMachine T7 transcription kit (Thermo) according to the manufacturer's protocol and were purified with a RNeasy kit (Qiagen). cRNA transcripts were microinjected into surgically extracted *Xenopus laevis* oocytes (Ecocyte) with a Nanoject III (Harvard Apparatus). Oocytes were injected with 0.1 ng (full-length TRPA1 variants) and/or 0.25 ng (truncated variants) of cRNA per cell, and whole-cell currents were measured 24-48 hours post-injection using two-electrode voltage clamp (TEVC). Currents were

measured using an OC-725D amplifier (Warner Instruments) delivering a ramp protocol from -100mV to +100mV applied every second. Microelectrodes were pulled from borosilicate glass capillary tubes and filled with 3M KCl. Microelectrode resistances of 0.7-1.2 MΩ were used for all experiments. Bath solution contained (in mM) 93.5 NaCl, 2 KCl, 2 $MgCl_2$, 0.1 $BaCl_2$, and 5 HEPES (pH 7.5) . For experiments in the presence of calcium, $BaCl_2$ was replaced with 1.8 mM $CaCl_2$. NaCl was replaced with NMDG at equimolar concentrations for experiments in Fig. 8f-h. All recordings were performed at room temperature. Data were subsequently analyzed using pClamp software (Molecular Devices). Internal background currents were subtracted from all recordings unless otherwise indicated. Oocytes were individually collected after recordings, lysed in 50 µL TRPA1 lysis buffer, and subjected to anti-FLAG immunoblot analysis to confirm construct expression as detailed in the Supplementary Information.

Immunofluorescence Imaging

HEK293T cells transiently transfected using Lipofectamine 2000 (ThermoFisher) according to manufacturer's protocol were incubated for 20 hours prior to immunostaining. Cells were fixed on coverslips with 3.5% paraformaldehyde for 15 minutes, and then incubated with 5 ug/mL Alexa Fluor 350-conjugated Wheat Germ Agglutinin (Invitrogen) in PBS at room temperature for 10 minutes, followed by permeabilization using PBS + 0.5% Triton X-100 for 10 minutes and incubation with PBS + 1% Bovine serum albumin (BSA) for 10 minutes. Cells were incubated with primary antibodies (anti-FLAG, mouse, Sigma F1804; anti-GFP, rabbit, Invitrogen G10362) diluted 1:1000 in PBS + 1% BSA for 16 hours at 4ºC. Cells were washed with PBS and incubated with secondary antibodies (AffiniPure goat anti-mouse IgG AlexaFluor594-conjugated, Jackson ImmunoResearch 115-585; AffiniPure goat anti-rabbit IgG AlexaFluor488-conjugated, Jackson ImmunoResearch 111-545) diluted 1:1000 in PBS + 1% BSA for 1 hour at room temperature. Images were acquired on a Nikon ECLIPSE Ti2 with a Hamamatsu Fusion sCMOS camera at 100X magnification.

Image Analysis and Deconvolution

For quantitative analysis of R919* TRPA1 intensity at the plasma membrane, raw single stack immunofluorescence images were processed in ImageJ using the line scanning function. A straight line was drawn through the width of at least 30 cells and the fluorescence intensity of each pixel was measured as a function of distance for each channel. Intensity was normalized to the average middle 30% of each line scan representing the cell interior, and distance was normalized from 0 to 1 to account for differences in cellular size. Line scans were compiled using GraphPad Prism, and the average maxima from all scans was taken to represent fluorescence intensity at the plasma membrane. For quantitative analysis of WT and R919* TRPA1 co-localization, raw single stack immunofluorescence images were processed in ImageJ using the line scanning function. Freehand lines were drawn over the plasma membrane, and the intensity of at least 450 pixels were measured for each channel. Measurements were normalized to the average intensity of each line scan to account for variability in transfection efficiency. Pearson's correlation coefficient (r) and the coefficients of determination (r^2) were calculated to represent WT and R919* TRPA1 colocalization. To deconvolve immunofluorescence images, stacks of optical sections (z step = 0.2 μm) were restored with Huygens software (Scientific Volume Imaging) using the maximum-likelihood estimation algorithm. The restored stacks were further processed in Photoshop CS4 (Adobe).

Biotinylation Assays

HEK293T cells were seeded in a 6-well plate pre-coated with Poly-L-Lysine (Sigma) and transfected with expression plasmids. 40-48 hours post-transfection, cells were washed with PBS, placed on ice, and incubated for 20 minutes with chilled 0.05 mg/mL Sulfo-NHS-LC-Biotin (Thermo Fisher) in Ringer's solution. Cells were then washed with chilled wash buffer (PBS supplemented with 100 mM Glycine) and the reaction was quenched on ice for 30 minutes with

100 mM Glycine and 0.5% BSA in PBS. Cells were then washed three times and lysed in TRPA1 lysis buffer (50 mM HEPES, 150 mM NaCl, 1 mM IP_6, 20 mM DDM, 1x EDTA-free Roche Complete Protease Inhibitor Cocktail, pH 7.8) supplemented with 100 mM Glycine directly on the 6-well plate. Lysates were collected, protein concentration was determined by BCA assay (Pierce), biotinylated proteins were isolated by Neutravidin pulldown and analyzed by immunoblot as described below. During quantification, any FLAG signal in the torsin eluates lane was subtracted from all other conditions to account for probe internalization.

For proximity biotinylation assays, HEK293T cells co-expressing 8xHis-BioID2- or 3x-FLAG-tagged TRPA1 and Kv1.2/2.1 fusion proteins were treated with 50 uM biotin supplemented into culture media ~24 hours post-transfection. Cells were lysed 16 hours later with TRPA1 lysis buffer and affinity purified as below.

Pulldown Experiments

40-48 hours post-transfection, HEK293T cells were lysed in TRPA1 lysis buffer. Total protein concentration was quantitated using BCA assay (Pierce). Equal concentrations of protein lysate from each experimental condition were added to affinity resins. 10% of loaded protein amount was reserved as a whole-cell lysate loading control. Affinity purification, PAGE, and immunoblotting were performed as described below.

FLAG Immunoprecipitation: Lysates were incubated with EZview Red Anti-FLAG M2 affinity resin (Sigma) for 1 hour at 4°C with gentle rotation. Resin beads were washed four times with lysis buffer prior to elution with 125 µg/ml 3xFLAG peptide (Sigma).

Amylose Pulldown: Lysates were incubated with amylose resin (New England Biolabs) for 1 hour at 4°C with gentle rotation. The resin beads were washed five to six times with lysis buffer prior to elution in 60 mM maltose (Sigma).

Strep Pulldown: Lysates were incubated with Strep Tactin Sepharose (IBA) for 1 hour at 4°C with gentle rotation. The resin beads were washed six times with lysis buffer prior to elution in 1X Buffer E (IBA). For tandem pulldown assays, Strep-enriched eluates were subsequently incubated with EZview Red Anti-FLAG M2 affinity resin for 2 hours at 4°C with gentle rotation and washed 6 times with lysis buffer prior to elution as above.

Neutravidin Pulldown: Cell lysates that were generated following surface labeling or proximity biotinylation experiments were incubated with Neutravidin resin (Pierce) for 2 hours at 4°C with gentle rotation. The resin was then washed with lysis buffer three times, followed by a harsher wash with 1x PBS supplemented with 100 mM DTT. Resin was then washed once each with lysis buffer and 1x PBS. Biotinylated protein was eluted from the resin with a multi-step protocol to prevent TRPA1 aggregation while maximizing protein elution from the resin. First, resin was incubated with 10 µL of biotin elution buffer (TRPA1 lysis buffer, 100 mM Glycine, 10 mM Biotin, 1% SDS) on ice for 10 min, followed by addition of 1 µL β-mercaptoethanol (BME; Sigma) to each sample and incubation on ice for 5 minutes, and finally by addition of 4 µL 4x Laemmli buffer supplemented with 10% BME and incubated at 65°C for 10 minutes. The resin was centrifuged, supernatant was removed and combined with additional 4 µL Laemmli buffer supplemented with 10% BME for SDS-PAGE analysis.

Ni-NTA pulldown: Cell lysate samples were incubated with His-Pur Ni-NTA resin (ThermoFisher) for 30 minutes at 4°C with gentle rotation. Resin was washed 3x with lysis buffer and eluted with 400 mM imidazole.

SDS-PAGE and Immunoblot

Samples were combined with 4x Laemmli Sample buffer supplemented with 10% BME, separated on pre-cast 4-20% SDS-PAGE gels (BioRad), and transferred onto PVDF membranes (BioRad) by semi-dry transfer. Blots were blocked in 3% BSA prior to antibody probing. The following primary antibodies were used in 1x PBST buffer (Boston Bioproducts): MBP (mouse, 1:30,000,

New England Biolabs E8032), FLAG (mouse, 1:30,000, Sigma A8592), strep (mouse, 1:30,000, IBA 2-1509-001), tubulin (mouse, 1:5,000 in BSA, Sigma T6199), HA (rat, 1:2,000 in BSA, Roche 12013819001), and His probe (1:50,000, Thermo 15165). HRP-conjugated IgG secondary anti-mouse antibody was used as needed (rabbit, 1:25,000, Thermo 61-6520). Membranes were developed using Clarity Western ECL substrate (Bio-Rad) and imaged using a Chemidoc Imaging System (BioRad). Densitometric quantifications were performed with ImageJ software. All quantified band intensities for eluted samples were normalized to their tubulin-normalized input band intensities, except for the tandem purification crude stoichiometric analysis in Fig. 5f where only MBP signal intensity in eluates was used.

Intracellular ROS detection

Intracellular generation of ROS was measured via conversion of 2,7 dihydro-dichlorofluorescein diacetate (H_2DCF-DA) into the fluorescent product dichlorofluorescein (DCF) upon oxidation. Our procedure was adapted from previously reported protocols (Paulsen et al, *Nat Chem Bio*, 2011). Briefly, HEK293T cells transfected with empty vector (mock) or hTRPA1 variants were seeded into a 96-well dish 20 hours post-transfection. 40 hours after transfection, cells were loaded with 50 μM H_2DCF-DA dye in Ringer's solution for 1 hour at 37 °C. Cells were then washed 1x and resuspended in Ringer's solution. Fluorescence was measured in a BioTek SynergyMx plate reader (excitation: 488 nm ; emission 525 nm). Background readings were from wells containing Ringer's solution only. H_2DCF-DA dye treated with 400 μM H_2O_2 was the positive control.

ER Stress Assay

C-terminally truncated Lamin B receptor (LBR1600*) has been shown to be metabolically unstable, and generally undergoes rapid turnover that is partially dependent on ERAD factors such as p97, Ufd1, Npl4, and Hrd1 (Tsai et al, *Elife*, 2016). When these factors are pharmacologically inhibited, LBR1600* is stabilized, and can therefore be used as a model

substrate for ERAD. Our procedure was adapted from previously reported protocols. Briefly, HA-tagged LBR1600* was co-transfected into HEK293T cells alongside empty vector (mock) or 3xFLAG-WT and 3xFLAG R919* hTRPA1. 20-40 hours post-transfection, cells were treated with 10 μM of p97 inhibitor CB5983 in Ringer's solution for 0, 4 or 8 hrs. Cells were then lysed, analyzed by SDS-PAGE and Western blot, as described above.

Fluorescence Size Exclusion Chromatography (FSEC)

FSEC procedures were adapted from those previously reported [19]. Briefly, sample volumes were brought to 1 mL with TRPA1 lysis buffer, then passed through 0.22-micron filters (Costar) by centrifugation, loaded onto a Superose 6 Increase column (GE Healthcare) pre-equilibrated with FSEC buffer (20 mM HEPES, 150 mM NaCl, 1 mM BME, 0.5 mM DDM, 1 mM IP_6, pH 8), and run at a flow rate of 0.5 ml/min. The in-line fluorescence detector (Shimadzu) spectral settings were as follows: Ex:488; Em: 510 nm (eGFP), Ex:515; Em:528 nm (mVenus), Ex: 433; Em: 475 nm (mCerulean); time increment, 1 s; integration time, 1 s. Data were collected with Unicorn v7.2 software. Fractions corresponding to TRPA1 and free FLAG peptide peaks were collected, concentrated using Amicon Ultra 10 KDa cut-off spin filters, and subjected to immunoblot analysis.

For experiments in Fig. 5c, GFP- and 3xFLAG-tagged constructs were co-expressed in the indicated combinations for 40-48 hours. Lysates were subjected to FLAG immunoprecipitation prior to FSEC analysis.

For dual-color experiments in Supplementary Fig. 7, cells were transfected with 8xHis-mCerulean-WT hTRPA1 and/or FLAG-mVenus-R919* hTRPA1. Cells were lysed 40 hours post-transfection. For Supplementary Fig. 7b, lysates were subjected to Nickel-FLAG tandem purifications. For Supplementary Fig. S7d and e, whole cell lysates were used. Eluates or lysates were divided into two and analyzed sequentially with FSEC, first with mCerulean and second with

mVenus fluorescence detection settings. Tandem purified samples were also analyzed by immunoblot analysis in Supplementary Fig. 7c.

Blue Native PAGE

Lysates containing dual-tagged WT and R919* TRPA1 were tandem-purified with strep and FLAG affinity resins as described above. Eluates were split into two aliquots, one of which was given full denaturation treatment in Laemmli Sample buffer supplemented with 10% BME, while the second was added to NativePAGE Sample Buffer and 5% G-250 Sample Additive (Invitrogen) as per manufacturer instructions. Samples were loaded onto 4–15% Mini-Protean TGX Gels (Bio-Rad) and run at 180 V in NativePAGE Running Buffer (Invitrogen) with 10x Coomassie additive in the cathode buffer. After 25 min, the voltage was adjusted to 115 V for the remainder of the run. After 40 min of run time, the 10x Coomassie cathode buffer was removed and replaced with 1x Coomassie running buffer for the remaining 1.5 hours. Transfer to PVDF membrane and immunoblotting were performed as described above.

Statistical Analysis

All data quantification was performed in Microsoft Excel. Quantified data presentation and statistical analyses were performed in GraphPad Prism. The GraphPad Prism colorblind safe color pallet was applied to all quantified data presented. Data represent mean ± SEM. Each experiment was performed a minimum of three independent times. Comparison between two groups was analyzed by Student's t test, and comparison between multiple groups was analyzed by one-way ANOVA with Bonferroni or Tukey's *post hoc* analysis, as indicated. Criterion for statistical significance for all tests was $p<0.05$.

2.5 References:

1. Bautista, D.M., Pellegrino, M. & Tsunozaki, M. TRPA1: A gatekeeper for inflammation. *Annu Rev Physiol* **75**, 181-200 (2013).
2. Chen, J. & Hackos, D.H. TRPA1 as a drug target--promise and challenges. *Naunyn Schmiedebergs Arch Pharmacol* **388**, 451-63 (2015).
3. Grace, M.S., Baxter, M., Dubuis, E., Birrell, M.A. & Belvisi, M.G. Transient receptor potential (TRP) channels in the airway: role in airway disease. *Br J Pharmacol* **171**, 2593-607 (2014).
4. Julius, D. TRP channels and pain. *Annu Rev Cell Dev Biol* **29**, 355-84 (2013).
5. Talavera, K. et al. Mammalian Transient Receptor Potential TRPA1 Channels: From Structure to Disease. *Physiol Rev* **100**, 725-803 (2020).
6. Zhang, X. Targeting TRP ion channels for itch relief. *Naunyn Schmiedebergs Arch Pharmacol* **388**, 389-99 (2015).
7. Asgar, J. et al. The role of TRPA1 in muscle pain and mechanical hypersensitivity under inflammatory conditions in rats. *Neuroscience* **310**, 206-15 (2015).
8. Holzer, P. TRP channels in the digestive system. *Curr Pharm Biotechnol* **12**, 24-34 (2011).
9. Wang, Z. et al. The TRPA1 Channel in the Cardiovascular System: Promising Features and Challenges. *Front Pharmacol* **10**, 1253 (2019).
10. Bandell, M. et al. Noxious cold ion channel TRPA1 is activated by pungent compounds and bradykinin. *Neuron* **41**, 849-57 (2004).
11. Hinman, A., Chuang, H.H., Bautista, D.M. & Julius, D. TRP channel activation by reversible covalent modification. *Proc Natl Acad Sci U S A* **103**, 19564-8 (2006).
12. Jordt, S.E. et al. Mustard oils and cannabinoids excite sensory nerve fibres through the TRP channel ANKTM1. *Nature* **427**, 260-5 (2004).
13. Macpherson, L.J. et al. Noxious compounds activate TRPA1 ion channels through covalent modification of cysteines. *Nature* **445**, 541-5 (2007).
14. Liu, C. et al. A Non-covalent Ligand Reveals Biased Agonism of the TRPA1 Ion Channel. *Neuron* **109**, 273-284 e4 (2021).
15. Xiao, B. et al. Identification of transmembrane domain 5 as a critical molecular determinant of menthol sensitivity in mammalian TRPA1 channels. *J Neurosci* **28**, 9640-51 (2008).
16. Xu, H., Delling, M., Jun, J.C. & Clapham, D.E. Oregano, thyme and clove-derived flavors and skin sensitizers activate specific TRP channels. *Nat Neurosci* **9**, 628-35 (2006).
17. Zygmunt, P.M. & Hogestatt, E.D. Trpa1. *Handb Exp Pharmacol* **222**, 583-630 (2014).
18. Kremeyer, B. et al. A gain-of-function mutation in TRPA1 causes familial episodic pain syndrome. *Neuron* **66**, 671-80 (2010).
19. Paulsen, C.E., Armache, J.P., Gao, Y., Cheng, Y. & Julius, D. Structure of the TRPA1 ion channel suggests regulatory mechanisms. *Nature* **520**, 511-7 (2015).
20. Suo, Y. et al. Structural Insights into Electrophile Irritant Sensing by the Human TRPA1 Channel. *Neuron* **105**, 882-894 e5 (2020).
21. Zhao, J., Lin King, J.V., Paulsen, C.E., Cheng, Y. & Julius, D. Irritant-evoked activation and calcium modulation of the TRPA1 receptor. *Nature* **585**, 141-145 (2020).
22. Kim, D. & Cavanaugh, E.J. Requirement of a soluble intracellular factor for activation of transient receptor potential A1 by pungent chemicals: role of inorganic polyphosphates. *J Neurosci* **27**, 6500-9 (2007).
23. Laursen, W.J., Anderson, E.O., Hoffstaetter, L.J., Bagriantsev, S.N. & Gracheva, E.O. Species-specific temperature sensitivity of TRPA1. *Temperature (Austin)* **2**, 214-26 (2015).
24. Cordero-Morales, J.F., Gracheva, E.O. & Julius, D. Cytoplasmic ankyrin repeats of transient receptor potential A1 (TRPA1) dictate sensitivity to thermal and chemical stimuli. *Proc Natl Acad Sci U S A* **108**, E1184-91 (2011).
25. Jabba, S. et al. Directionality of temperature activation in mouse TRPA1 ion channel can be inverted by single-point mutations in ankyrin repeat six. *Neuron* **82**, 1017-31 (2014).
26. Kullmann, D.M. & Waxman, S.G. Neurological channelopathies: new insights into disease mechanisms and ion channel function. *J Physiol* **588**, 1823-7 (2010).

27. Nirenberg, M.J., Chaouni, R., Biller, T.M., Gilbert, R.M. & Paisan-Ruiz, C. A novel TRPA1 variant is associated with carbamazepine-responsive cramp-fasciculation syndrome. *Clin Genet* **93**, 164-168 (2018).
28. Johnson, A.A. et al. Autosomal Recessive Bestrophinopathy Is Not Associated With the Loss of Bestrophin-1 Anion Channel Function in a Patient With a Novel BEST1 Mutation. *Invest Ophthalmol Vis Sci* **56**, 4619-30 (2015).
29. Li, J., Maghera, J., Lamothe, S.M., Marco, E.J. & Kurata, H.T. Heteromeric Assembly of Truncated Neuronal Kv7 Channels: Implications for Neurologic Disease and Pharmacotherapy. *Mol Pharmacol* **98**, 192-202 (2020).
30. Miyagi, K. et al. A pathogenic C terminus-truncated polycystin-2 mutant enhances receptor-activated Ca2+ entry via association with TRPC3 and TRPC7. *J Biol Chem* **284**, 34400-12 (2009).
31. Menezes, L.F.S., Sabia Junior, E.F., Tibery, D.V., Carneiro, L.D.A. & Schwartz, E.F. Epilepsy-Related Voltage-Gated Sodium Channelopathies: A Review. *Front Pharmacol* **11**, 1276 (2020).
32. Waxman, S.G. Painful Na-channelopathies: an expanding universe. *Trends Mol Med* **19**, 406-9 (2013).
33. Cannon, S.C. Channelopathies of skeletal muscle excitability. *Compr Physiol* **5**, 761-90 (2015).
34. Jurkat-Rott, K. et al. Calcium currents and transients of native and heterologously expressed mutant skeletal muscle DHP receptor alpha1 subunits (R528H). *FEBS Lett* **423**, 198-204 (1998).
35. Kass, R.S. The channelopathies: novel insights into molecular and genetic mechanisms of human disease. *J Clin Invest* **115**, 1986-9 (2005).
36. Simpson, B.J. et al. Characterization of three myotonia-associated mutations of the CLCN1 chloride channel gene via heterologous expression. *Hum Mutat* **24**, 185 (2004).
37. Fan, Z. & Neff, R.A. Susceptibility of ATP-sensitive K+ channels to cell stress through mediation of phosphoinositides as examined by photoirradiation. *J Physiol* **529 Pt 3**, 707-21 (2000).
38. Kovacevic, J. et al. Protein instability, haploinsufficiency, and cortical hyper-excitability underlie STXBP1 encephalopathy. *Brain* **141**, 1350-1374 (2018).
39. Lee, T.T. et al. Myotonia congenita mutation enhances the degradation of human CLC-1 chloride channels. *PLoS One* **8**, e55930 (2013).
40. Pardillo-Diaz, R., Carrascal, L., Barrionuevo, G. & Nunez-Abades, P. Oxidative stress induced by cumene hydroperoxide produces synaptic depression and transient hyperexcitability in rat primary motor cortex neurons. *Mol Cell Neurosci* **82**, 204-217 (2017).
41. Pasantes-Morales, H. & Tuz, K. Volume changes in neurons: hyperexcitability and neuronal death. *Contrib Nephrol* **152**, 221-240 (2006).
42. Poli, M.C. et al. Heterozygous Truncating Variants in POMP Escape Nonsense-Mediated Decay and Cause a Unique Immune Dysregulatory Syndrome. *Am J Hum Genet* **102**, 1126-1142 (2018).
43. Tanaka, M. et al. Hyperglycosylation and reduced GABA currents of mutated GABRB3 polypeptide in remitting childhood absence epilepsy. *Am J Hum Genet* **82**, 1249-61 (2008).
44. Viard, P. et al. PI3K promotes voltage-dependent calcium channel trafficking to the plasma membrane. *Nat Neurosci* **7**, 939-46 (2004).
45. Zhou, Y., Suzuki, Y., Uchida, K. & Tominaga, M. Identification of a splice variant of mouse TRPA1 that regulates TRPA1 activity. *Nat Commun* **4**, 2399 (2013).
46. Huang, X., Tian, M., Hernandez, C.C., Hu, N. & Macdonald, R.L. The GABRG2 nonsense mutation, Q40X, associated with Dravet syndrome activated NMD and generated a truncated subunit that was partially rescued by aminoglycoside-induced stop codon read-through. *Neurobiol Dis* **48**, 115-23 (2012).
47. Schmidt, M., Dubin, A.E., Petrus, M.J., Earley, T.J. & Patapoutian, A. Nociceptive signals induce trafficking of TRPA1 to the plasma membrane. *Neuron* **64**, 498-509 (2009).
48. Doi, T. et al. A novel KCNJ2 nonsense mutation, S369X, impedes trafficking and causes a limited form of Andersen-Tawil syndrome. *Circ Cardiovasc Genet* **4**, 253-60 (2011).
49. Gong, Q., Keeney, D.R., Robinson, J.C. & Zhou, Z. Defective assembly and trafficking of mutant HERG channels with C-terminal truncations in long QT syndrome. *J Mol Cell Cardiol* **37**, 1225-33 (2004).

50. Quilty, J.A., Cordat, E. & Reithmeier, R.A. Impaired trafficking of human kidney anion exchanger (kAE1) caused by hetero-oligomer formation with a truncated mutant associated with distal renal tubular acidosis. *Biochem J* **368**, 895-903 (2002).
51. Torres, G.E. et al. Oligomerization and trafficking of the human dopamine transporter. Mutational analysis identifies critical domains important for the functional expression of the transporter. *J Biol Chem* **278**, 2731-9 (2003).
52. Phelps, C.B. & Gaudet, R. The role of the N terminus and transmembrane domain of TRPM8 in channel localization and tetramerization. *J Biol Chem* **282**, 36474-80 (2007).
53. Chase, A.R., Laudermilch, E. & Schlieker, C. Torsin ATPases: Harnessing Dynamic Instability for Function. *Front Mol Biosci* **4**, 29 (2017).
54. Dunn, K.W., Kamocka, M.M. & McDonald, J.H. A practical guide to evaluating colocalization in biological microscopy. *Am J Physiol Cell Physiol* **300**, C723-42 (2011).
55. van Unen, J. et al. The C-terminus of the oncoprotein TGAT is necessary for plasma membrane association and efficient RhoA-mediated signaling. *BMC Cell Biol* **19**, 6 (2018).
56. Kim, D.I. et al. An improved smaller biotin ligase for BioID proximity labeling. *Mol Biol Cell* **27**, 1188-96 (2016).
57. Cheng, W., Sun, C. & Zheng, J. Heteromerization of TRP channel subunits: extending functional diversity. *Protein Cell* **1**, 802-10 (2010).
58. Chubanov, V. et al. Disruption of TRPM6/TRPM7 complex formation by a mutation in the TRPM6 gene causes hypomagnesemia with secondary hypocalcemia. *Proc Natl Acad Sci U S A* **101**, 2894-9 (2004).
59. Fischer, M.J. & Edwardson, J.M. V2A2lidating TRP channel heteromers. *Temperature (Austin)* **1**, 26-7 (2014).
60. Hellwig, N., Albrecht, N., Harteneck, C., Schultz, G. & Schaefer, M. Homo- and heteromeric assembly of TRPV channel subunits. *J Cell Sci* **118**, 917-28 (2005).
61. Hoenderop, J.G. et al. Homo- and heterotetrameric architecture of the epithelial Ca2+ channels TRPV5 and TRPV6. *EMBO J* **22**, 776-85 (2003).
62. Hofmann, T., Schaefer, M., Schultz, G. & Gudermann, T. Subunit composition of mammalian transient receptor potential channels in living cells. *Proc Natl Acad Sci U S A* **99**, 7461-6 (2002).
63. Owsianik, G., D'Hoedt, D., Voets, T. & Nilius, B. Structure-function relationship of the TRP channel superfamily. *Rev Physiol Biochem Pharmacol* **156**, 61-90 (2006).
64. Owsianik, G., Talavera, K., Voets, T. & Nilius, B. Permeation and selectivity of TRP channels. *Annu Rev Physiol* **68**, 685-717 (2006).
65. Strubing, C., Krapivinsky, G., Krapivinsky, L. & Clapham, D.E. TRPC1 and TRPC5 form a novel cation channel in mammalian brain. *Neuron* **29**, 645-55 (2001).
66. Tsiokas, L. et al. Specific association of the gene product of PKD2 with the TRPC1 channel. *Proc Natl Acad Sci U S A* **96**, 3934-9 (1999).
67. Zeevi, D.A., Lev, S., Frumkin, A., Minke, B. & Bach, G. Heteromultimeric TRPML channel assemblies play a crucial role in the regulation of cell viability models and starvation-induced autophagy. *J Cell Sci* **123**, 3112-24 (2010).
68. Gracheva, E.O. et al. Ganglion-specific splicing of TRPV1 underlies infrared sensation in vampire bats. *Nature* **476**, 88-91 (2011).
69. Naert, R., Talavera, A., Startek, J.B. & Talavera, K. TRPA1 gene variants hurting our feelings. *Pflugers Arch* **472**, 953-960 (2020).
70. Kawate, T. & Gouaux, E. Fluorescence-detection size-exclusion chromatography for precrystallization screening of integral membrane proteins. *Structure* **14**, 673-81 (2006).
71. Parcej, D., Guntrum, R., Schmidt, S., Hinz, A. & Tampe, R. Multicolour fluorescence-detection size-exclusion chromatography for structural genomics of membrane multiprotein complexes. *PLoS One* **8**, e67112 (2013).
72. Wang, Y.Y., Chang, R.B., Waters, H.N., McKemy, D.D. & Liman, E.R. The nociceptor ion channel TRPA1 is potentiated and inactivated by permeating calcium ions. *J Biol Chem* **283**, 32691-703 (2008).
73. Boton, R., Dascal, N., Gillo, B. & Lass, Y. Two calcium-activated chloride conductances in Xenopus laevis oocytes permeabilized with the ionophore A23187. *J Physiol* **408**, 511-34 (1989).
74. Leonard, J.P. & Kelso, S.R. Apparent desensitization of NMDA responses in Xenopus oocytes involves calcium-dependent chloride current. *Neuron* **4**, 53-60 (1990).

75. Chen, J. et al. Pore dilation occurs in TRPA1 but not in TRPM8 channels. *Mol Pain* **5**, 3 (2009).
76. Egelman, D.M. & Montague, P.R. Calcium dynamics in the extracellular space of mammalian neural tissue. *Biophys J* **76**, 1856-67 (1999).
77. Davidson, S. et al. Human sensory neurons: Membrane properties and sensitization by inflammatory mediators. *Pain* **155**, 1861-1870 (2014).
78. Cao, E., Cordero-Morales, J.F., Liu, B., Qin, F. & Julius, D. TRPV1 channels are intrinsically heat sensitive and negatively regulated by phosphoinositide lipids. *Neuron* **77**, 667-79 (2013).
79. Tsuruda, P.R., Julius, D. & Minor, D.L., Jr. Coiled coils direct assembly of a cold-activated TRP channel. *Neuron* **51**, 201-12 (2006).
80. Nilius, B. & Owsianik, G. Transient receptor potential channelopathies. *Pflugers Arch* **460**, 437-50 (2010).
81. Arrigoni, C. et al. Unfolding of a Temperature-Sensitive Domain Controls Voltage-Gated Channel Activation. *Cell* **164**, 922-36 (2016).
82. Catterall, W.A. Voltage-gated calcium channels. *Cold Spring Harb Perspect Biol* **3**, a003947 (2011).
83. Lyu, L. et al. A new interaction between proximal and distal C-terminus of Cav1.2 channels. *J Pharmacol Sci* **133**, 240-246 (2017).
84. Diaz-Franulic, I., Raddatz, N., Castillo, K., Gonzalez-Nilo, F.D. & Latorre, R. A folding reaction at the C-terminal domain drives temperature sensing in TRPM8 channels. *Proc Natl Acad Sci U S A* **117**, 20298-20304 (2020).
85. Hasan, R., Leeson-Payne, A.T., Jaggar, J.H. & Zhang, X. Calmodulin is responsible for Ca(2+)-dependent regulation of TRPA1 Channels. *Sci Rep* **7**, 45098 (2017).
86. Sura, L. et al. C-terminal acidic cluster is involved in Ca2+-induced regulation of human transient receptor potential ankyrin 1 channel. *J Biol Chem* **287**, 18067-77 (2012).
87. Zurborg, S., Yurgionas, B., Jira, J.A., Caspani, O. & Heppenstall, P.A. Direct activation of the ion channel TRPA1 by Ca2+. *Nat Neurosci* **10**, 277-9 (2007).
88. Ye, W. et al. Activation Stoichiometry and Pore Architecture of TRPA1 Probed with Channel Concatemers. *Sci Rep* **8**, 17104 (2018).
89. Goldberg, Y.P. et al. Loss-of-function mutations in the Nav1.7 gene underlie congenital indifference to pain in multiple human populations. *Clin Genet* **71**, 311-9 (2007).
90. Kabra, M. & Pattnaik, B.R. Sensing through Non-Sensing Ocular Ion Channels. *Int J Mol Sci* **21**(2020).
91. Singh, B. et al. A Kv4.2 truncation mutation in a patient with temporal lobe epilepsy. *Neurobiol Dis* **24**, 245-53 (2006).
92. Notredame, C., Higgins, D.G. & Heringa, J. T-Coffee: A novel method for fast and accurate multiple sequence alignment. *J Mol Biol* **302**, 205-17 (2000).
92 Bautista, D. M., *et al*. TRPA1 mediates the inflammatory actions of environmental irritants and proalgesic agents. *Cell*, *124*(6), 1269–1282. (2006).
93 Alvarado, M. G., Thakore, P. & Earley, S. Transient receptor potential channel ankyrin 1: a unique regulator of vascular function. *Cells* **10**, 1167 (2021).
94 Waller, D. G. Systemic and pulmonary hypertension. in *Elsevier eBooks* (2018). doi:10.1016/b978-0-7020-7167-6.00006-3.
95 Purhonen, A.-K., Louhivuori, L., Kiehne, K., Åkerman, K. E. O. & Herzig, K. TRPA1 channel activation induces cholecystokinin release via extracellular calcium. *FEBS Letters* **582**, 229–232 (2007).
96 Lieder, B. *et al.* Structure-Dependent effects of cinnamaldehyde derivatives on TRPA1-Induced serotonin release in human intestinal cell models. *Journal of Agricultural and Food Chemistry* **68**, 3924–3932 (2020).
97 Lapointe, T. K. & Altier, C. The role of TRPA1 in visceral inflammation and pain. *Channels* **5**, 525–529 (2011).
98 Engel, M. *et al.* TRPA1 and substance P mediate colitis in mice. *Gastroenterology* **141**, 1346–1358 (2011).

2.7 Figures:

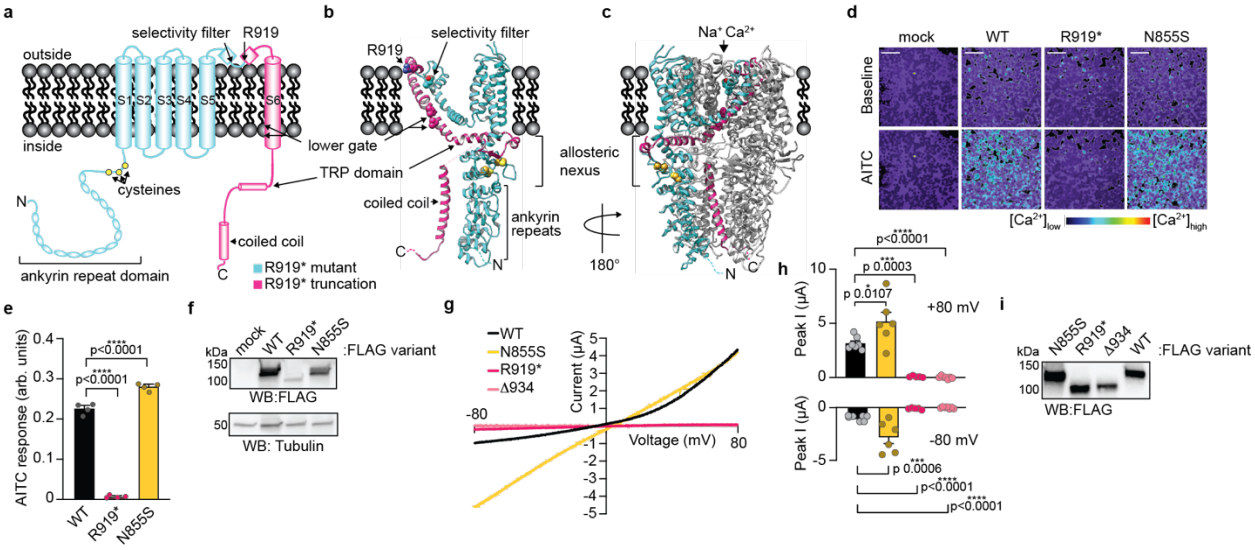

Figure 1. The R919* mutant is a nonfunctional *TRPA1* natural variant. (a) Cartoon schematic of a full-length hTRPA1 monomeric subunit, with relevant structural features denoted. Regions retained in R919* hTRPA1 are indicated in teal and regions truncated are indicated in pink. (b-c) Ribbon diagrams of WT hTRPA1 atomic model for residues K446-T1078 from a single subunit (b) and the homotetrameric channel (c). Color scheme and relevant structural features denoted as in (a). In (c), only one subunit is colored for clarity. Allosteric nexus indicated with brackets. Models built with the human TRPA1 Cryo-EM structure (PDB: 6V9W) in UCSF Chimera. (d) Ratiometric calcium imaging of HEK293T cells transfected with empty vector (mock), WT, R919*, or N855S hTRPA1. Cells were stimulated with 100 μM AITC. Images are representative of three independent experiments. Scale bars indicate 100 μm. (e) Quantification of AITC-evoked change in Fura-2 ratio (arbitrary units, arb. units) for WT (black), R919* (deep pink), or N855S (yellow) hTRPA1 variants. Data represent mean ± SEM. n = 4 independent experiments, n ≥ 90 cells per transfection condition per experiment. ****p<0.0001, one-way ANOVA with Bonferroni's *post hoc* analysis. (f) Western blot of lysates from cells expressing 3xFLAG-tagged hTRPA1 variants, probed using HRP-conjugated anti-FLAG antibody. Tubulin was the loading control. Results were verified in four independent experiments. (g) Representative voltage ramp (-80 mV to +80 mV) current-voltage (I-V) relationships from *Xenopus laevis* oocytes expressing WT (black), N855S (yellow), R919* (deep pink), or Δ934-1119 (pink) hTRPA1 variants. Currents evoked by 250 μM AITC. Extracellular solution contained no calcium. (h) Quantification of AITC-evoked peak current amplitudes at -80 mV and +80 mV. Colors as indicated in (g). Data represent mean ± SEM. n = 5 (R919* and Δ934-1119 hTRPA1), 6 (N855S hTRPA1), or 7 (WT hTRPA1) independent oocytes. ****p<0.0001, ***p<0.001, *p<0.05, one-way ANOVA with Bonferroni's *post hoc* analysis. (i) Western blot of lysates from representative *Xenopus* oocytes used for recordings in (g) expressing 3xFLAG-tagged hTRPA1 variants, probed using HRP-conjugated anti-FLAG antibody. (f and i) Full blots are included in Supplementary Fig. 14. (e, g, and h) Source data are provided as a Source Data file.

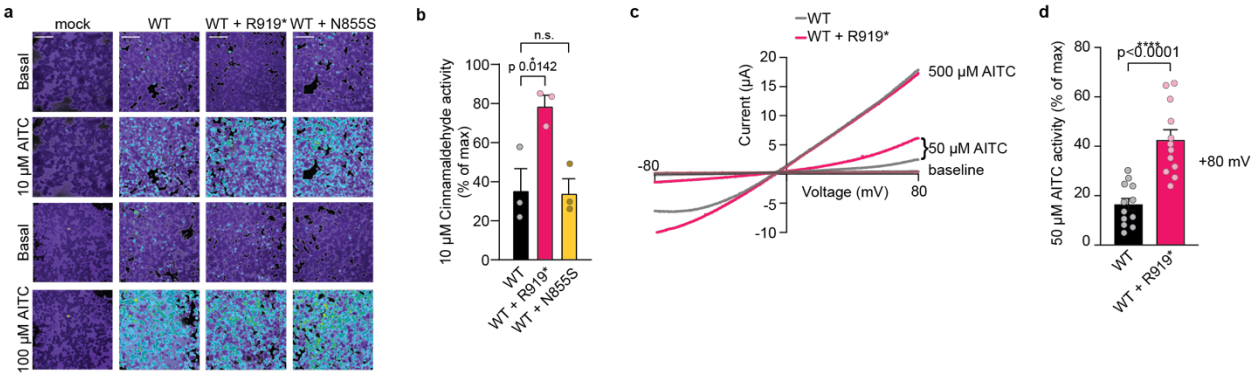

Figure 2. The R919* mutant confers hyperactivity when co-expressed with WT TRPA1. (a) Ratiometric calcium imaging of cells transfected with empty vector (mock), WT, WT and R919*, or WT and N855S hTRPA1. Cells were stimulated with 10 µM (top) or 100 µM (bottom) AITC. Images are representatives from three independent experiments. Scale bars indicate 100 µm. (b) Quantification of 10 µM Cinnamaldehyde-evoked change in Fura-2 ratio for WT (black), WT and R919* (pink), or WT and N885S (yellow) hTRPA1 relative to maximum response of each expression condition at 100 µM Cinnamaldehyde. Data represent mean ± SEM. *p<0.05, n.s. not significant. n = 3 independent experiments, n ≥ 90 cells per condition per experiment, one-way ANOVA with Bonferroni's *post hoc* analysis. (c) Representative raw I-V relationships from *Xenopus* oocytes expressing WT (black) or WT and R919* (pink) hTRPA1. Baseline currents and currents evoked by a sub-saturating (50 µM) or saturating (500 µM) AITC concentrations are shown. Extracellular solution contained 1.8 mM calcium. (d) Quantification of 50 µM AITC-evoked peak current amplitudes normalized to 500 µM AITC-evoked currents (max) at +80 mV holding potential. Colors as indicated in (c). Data represent mean ± SEM. ****p<0.0001. n = 12 oocytes per condition, two-tailed Student's t-test. (b and d) Source data are provided as a Source Data file.

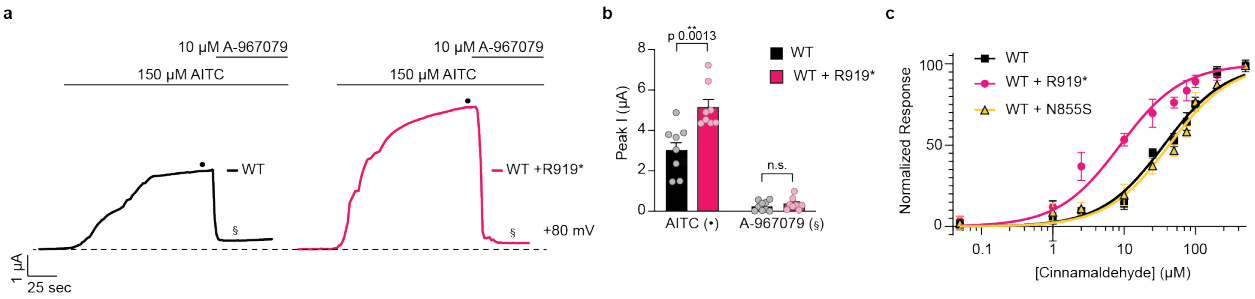

Figure 3. Hyperactive channels retain antagonist sensitivity and gain enhanced agonist sensitivity. (a) Representative whole-cell voltage-clamp recordings of *Xenopus* oocytes expressing WT hTRPA1 (black) or WT and R919* hTRPA1 (pink) at +80 mV holding potential. Currents evoked by 150 μM AITC (black dot) and inhibited by 10 μM A-967079 (double s). Dashed line denotes 0 μA current. Protocol of condition application indicated above. Extracellular solution contained no calcium. (b) Quantification of AITC-evoked and A-967079-inhibited peak current amplitudes at +80 mV. Colors as indicated in (a). Data represent mean ± SEM. **p<0.01, n.s. not significant. n = 8 oocytes per condition, two-tailed Student's t-test. (c) Dose-response curve of Cinnamaldehyde-evoked calcium responses for cells transfected with WT (black), WT and R919* (pink), or WT and N855S (yellow) hTRPA1. Calcium responses normalized to maximum calcium response to 500 μM Cinnamaldehyde. Traces represent average ± SEM of normalized calcium responses from 3 independent experiments, n = 30 cells per agonist concentration per experiment. Data were fit to a non-linear regression. EC_{50} (95% CI) values are 37.7 μM for WT hTRPA1 (95% CI, 30.5-45.8 μM), 7.8 μM for WT and R919* hTRPA1 (95% CI, 6.1-9.9 μM), and 43.1 μM for WT and N855S hTRPA1 (95% CI, 33.1-54.5 μM). Source data are provided as a Source Data file.

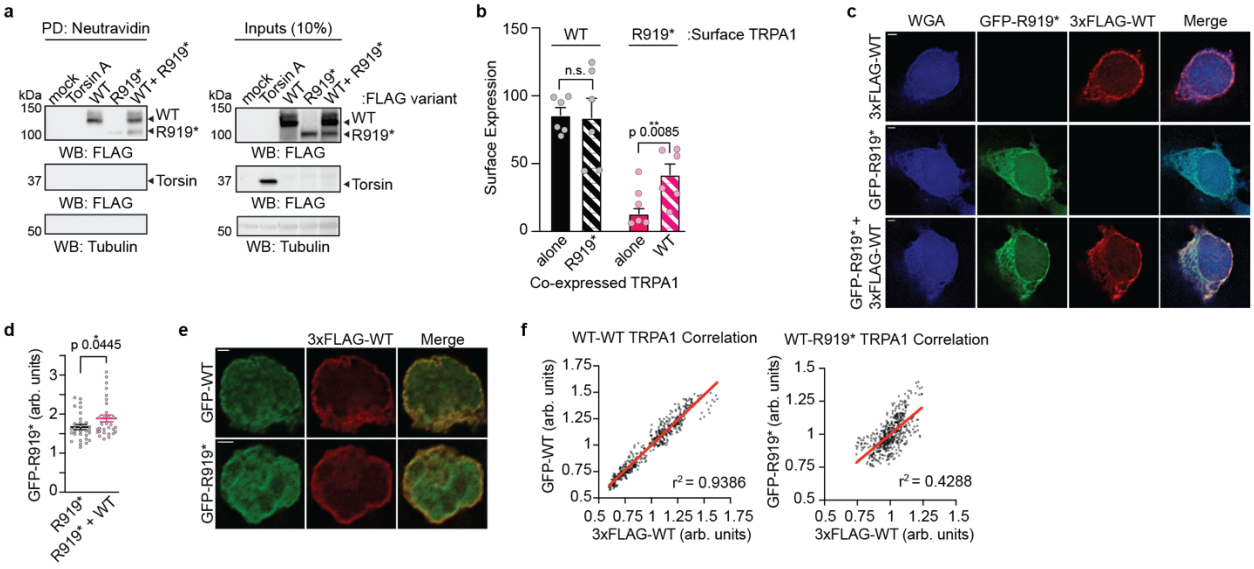

Figure 4. WT and R919* TRPA1 co-localize at the plasma membrane in cells. (a-b) Surface biotinylation analysis of 3xFLAG-WT or R919* hTRPA1 or FLAG-Torsin A from transfected HEK293T cells. Biotinylated proteins were precipitated by Neutravidin resin pulldown and probed using HRP-conjugated anti-FLAG antibody (a) and quantified (b). Tubulin from whole cell lysates (10%, inputs) was the loading control. Torsin A and Tubulin were negative controls for relative plasma membrane localization. Full blots are included in Supplementary Fig. 14. (b) Expression of WT (black) or R919* (pink) hTRPA1 in the plasma membrane is represented by filled bars (corresponding to lanes 2 and 3 in (a), respectively). Expression of WT or R919* hTRPA1 in the plasma membrane from co-transfected cells is represented by striped bars (corresponding to lane 4 in (a)). Data represent mean ± SEM. **p<0.01, n.s. not significant. n=6 independent experiments, two-tailed Student's t-test. (c) Representative deconvolved immunofluorescence images of HEK293T cells expressing GFP-R919*, 3xFLAG-WT, or GFP-R919* and 3xFLAG-WT hTRPA1. Cells were stained with anti-GFP (green) and anti-FLAG (red) antibodies. Plasma membrane was labeled with wheat germ agglutinin (blue). Scale bar indicates 2 μm. Images are representative of 3 independent experiments. (d) Quantification of GFP-R919* hTRPA1 fluorescence intensity in the plasma membrane of HEK293T cells relative to the cell interior (arbitrary units, arb. units). Values were obtained using line-scans of raw images. Data represent mean ± SEM. *p<0.05, n=30 cells per condition, two-tailed Student's t-test. (e) Representative deconvolved immunofluorescence images of HEK293T cells co-expressing 3xFLAG-WT hTRPA1 with GFP-WT or GFP-R919* hTRPA1. Cells were stained with anti-GFP (green) and anti-FLAG (red) antibodies. Scale bar indicates 2 μm. Images are representative of 3 independent experiments. (f) Scatter plot of 3xFLAG-WT hTRPA1 and GFP-WT (left) or R919* hTRPA1 (right) fluorescence intensity at the plasma membrane of HEK293T cells. Pearson's correlation coefficients (r) were determined using raw images and the coefficient of determination (r^2) is depicted in the lower right corner of each plot. A line of best fit is shown in red. p<0.0001, n>450 pixels in 1 cell per condition. (b, d, and f)

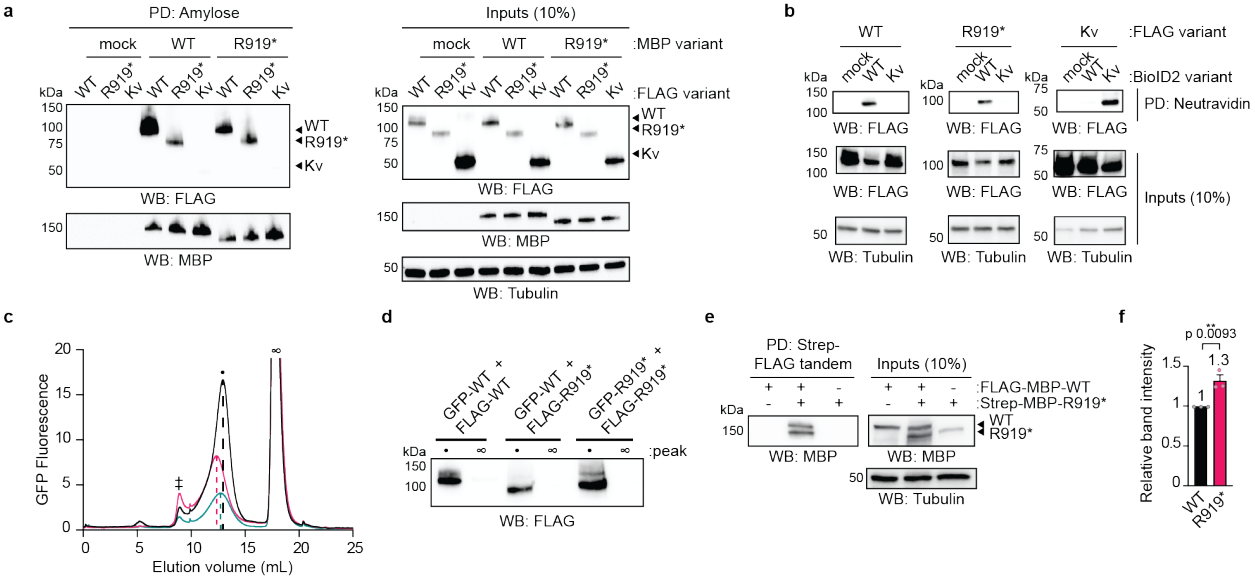

Figure 5. WT and R919* TRPA1 associate in cells to form complexes of similar size to homotetrameric WT channels. (a) Immunoblotting analysis of 3xFLAG-WT hTRPA1, R919* hTRPA1, or Kv1.2/2.1 protein expression after amylose pulldown from lysates of cells co-transfected with empty vector (mock), MBP-WT hTRPA1, or MBP-R919* hTRPA1. Samples were probed using HRP-conjugated anti-FLAG antibody. MBP-WT and R919* hTRPA1 were probed using anti-MBP antibody. Blots representative of three independent experiments. (b) Immunoblotting analysis of biotinylated 3xFLAG-WT hTRPA1, R919* hTRPA1, or Kv1.2/2.1 co-expressed with empty vector (mock), BioID2-WT hTRPA1, or BioID2-Kv1.2/2.1. Biotinylated proteins were precipitated by Neutravidin resin pulldown and probed using HRP-conjugated anti-FLAG antibody. Blots representative of three independent experiments. (c) FSEC chromatograms from cells co-expressing GFP-WT and 3xFLAG-WT hTRPA1 (black), GFP-WT and 3xFLAG-R919* hTRPA1 (pink), or GFP-R919* and 3xFLAG-R919* hTRPA1 (teal). FLAG immunoprecipitated eluates were analyzed by FSEC. Chromatograms reveal elution profiles of co-purified GFP-WT or R919* hTRPA1 complexes. Peaks corresponding to void (double cross), tetrameric WT hTRPA1 channels (black dot) and free FLAG peptide (infinity symbol) are indicated. Dashed lines denote the center elution volume of each co-purified complex. Results were verified in 3 independent trials. (d) Immunoblotting analysis of 3xFLAG-WT or R919* hTRPA1 from indicated peak fractions from (c) probed using HRP-conjugated anti-FLAG antibody. (e) Immunoblotting analysis of tandem-purified WT-R919* hTRPA1 complexes. FLAG-MBP-WT hTRPA1 and Strep-MBP-R919* hTRPA1 were transfected separately or together in cells. Lysates were tandem purified for Strep- then FLAG-tagged proteins. MBP-tagged proteins of tandem purification eluates were probed using anti-MBP antibody. In (a), (b), and (e) Tubulin from whole cell lysates was the loading control. (f) Quantitative analysis of FLAG-MBP-WT hTRPA1 (black) and Strep-MBP-R919* hTRPA1 (pink) from tandem purifications in (e). Band intensity was normalized to WT hTRPA1. Data represent mean ± SEM. Means are indicated above the bars. **p<0.01, n=3 independent experiments, two-tailed Student's t-test. (a, b, d, e) Full blots are included in Supplementary Fig. 15. (c and f)

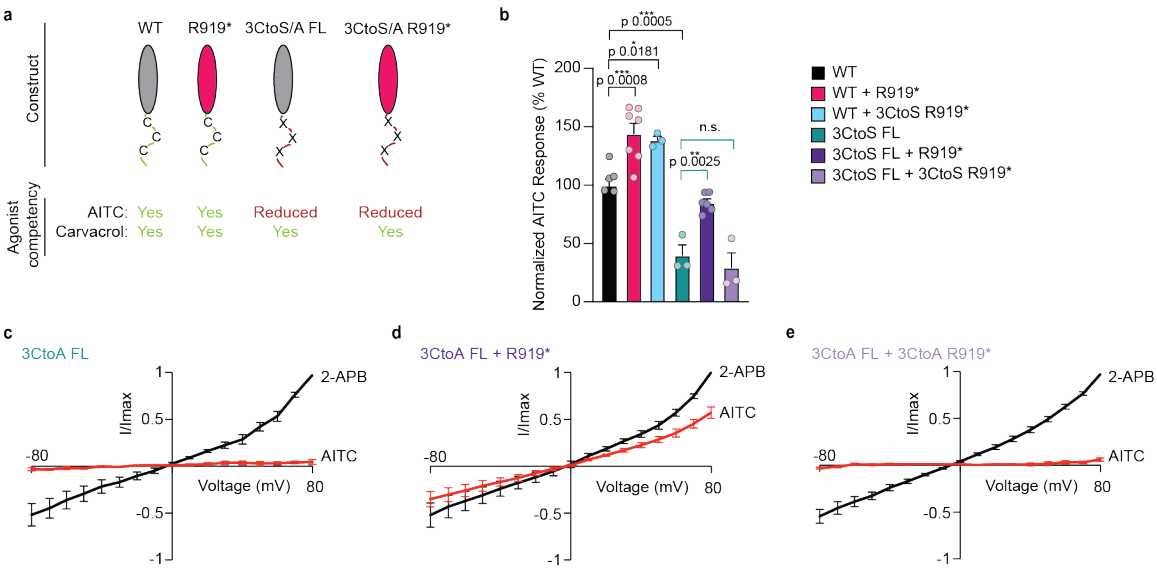

Figure 6. R919* TRPA1 subunits directly contribute to channel activity. (a) Schematic of full-length (FL, grey) and R919* (pink) hTRPA1 constructs used for electrophile agonist complementation assays. Agonist competency indicated in green (competent) or red (reduced competency). (b) Quantification of 10 µM AITC-evoked change in Fura-2 ratio relative to maximum response of each expression condition at 100 µM Carvacrol. Expression conditions are WT (black), WT and R919* (pink), WT and 3CtoS R919* (blue), 3CtoS FL (green), 3CtoS FL with R919* (deep purple), and 3CtoS FL with 3CtoS R919* (light purple) hTRPA1. Data further normalized to WT hTRPA1 as 100%. Data represent mean ± SEM. ***p<0.001, **p<0.01, *p<0.05, n.s. not significant. n = 3 (WT with 3CtoS R919*, 3CtoS FL, and 3CtoS FL with 3CtoS R919* hTRPA1), 5 (WT hTRPA1), 6 (3CtoS FL with R919* hTRPA1), or 7 (WT with R919* hTRPA1) independent experiments, n ≥ 90 cells per transfection condition per experiment, one-way ANOVA with Bonferroni's *post hoc* analysis. (c-e) Average I-V relationships from *Xenopus* oocytes expressing 3CtoA FL (c, n=7 independent oocytes), 3CtoA FL and R919* (d, n=8 independent oocytes), or 3CtoA FL and 3CtoA R919* (e, n=7 independent oocytes) hTRPA1. Currents were evoked sequentially with 150 µM AITC (red) and 500 µM 2-APB (black) applied to the same oocyte. Currents (I) normalized to 2-APB response at +80 mV (Imax). Extracellular solution contained no calcium. Error bars represent SEM across individual cell measurements. (b-e)

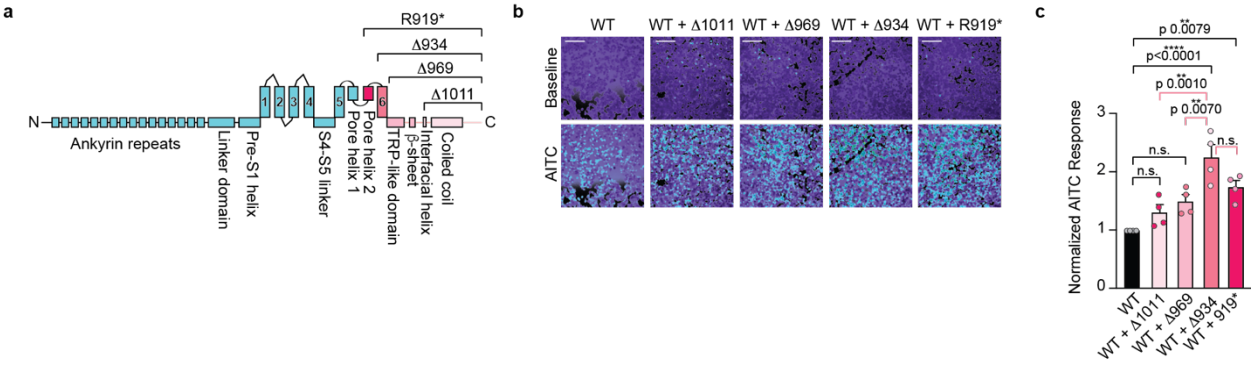

Figure 7. Source of R919* TRPA1-mediated channel hyperactivity. (a) Linear diagram depicting major structural domains in a WT hTRPA1 monomer. Missing portions from all C-terminal truncation constructs denoted above. R919* truncation completeness scales with gradations of pink. (b) Ratiometric calcium imaging of HEK293T cells transiently co-transfected with 3xFLAG-WT hTRPA1 and empty vector (mock) or the indicated C-terminal truncation constructs. Cells were stimulated with 10 μM AITC. Scale bars indicate 100 μm. Data representative of four independent experiments. (c) Quantification of 10 μM AITC-evoked change in Fura-2 ratio relative to maximum response of each expression condition at 100 μM AITC. Data further normalized to WT hTRPA1 response and WT hTRPA1 expression. Colors as indicated in (a). Data represent mean ± SEM. **** p<0.0001, ** p<0.01, n.s. not significant. n = 4 independent experiments, n ≥ 60 cells per transfection condition per experiment, one-way ANOVA with Tukey's *post hoc* analysis.

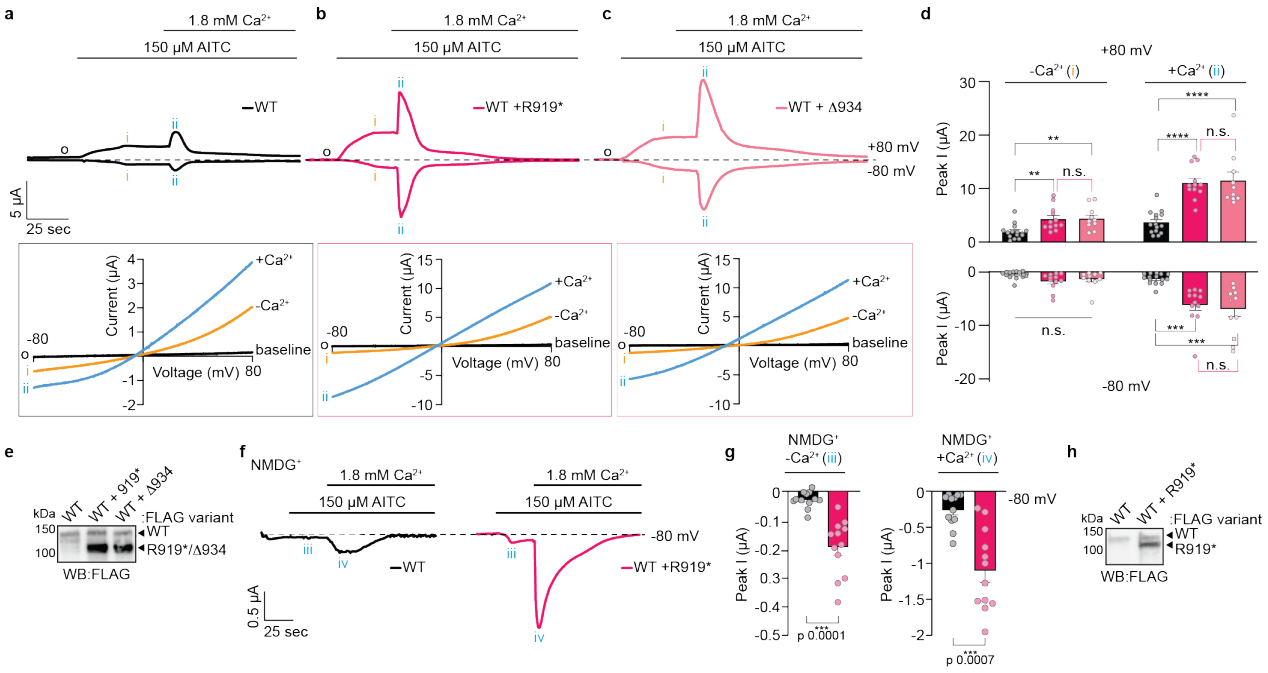

Figure 8. Functional characterization of R919* TRPA1-mediated channel hyperactivity. (a-c) Representative time-traces at -80 and +80 mV holding potentials (above) and the corresponding current-voltage relationships from timepoints indicated by o, i and ii (boxed below) from oocytes expressing WT TRPA1 (a, black), WT and R919* TRPA1 (b, deep pink), or WT and Δ934-1119 hTRPA1 (c, pink). Currents in the current-voltage relationships are raw, unadjusted values. Baseline currents (black o) and currents evoked with 150 µM AITC in the absence (orange i) and presence (blue ii) of 1.8 mM extracellular calcium are shown. (d) Quantification of peak current amplitudes from *Xenopus* oocytes used in a-c. Colors as indicated in (a-c). Data represent mean ± SEM. ****p<0.0001, ***p<0.001, **p<0.01,*p<0.05, n.s. not significant. n = 10 (WT with Δ934-1119 hTRPA1), 12 (WT with R919* hTRPA1), or 15 (WT hTRPA1) oocytes per condition, one-way ANOVA with Tukey's *post hoc* analysis. (f-g) Representative time-traces at -80 mV holding potential (f) and peak current amplitude quantification (g) from *Xenopus* oocytes expressing WT (black) or WT and R919* (deep pink) hTRPA1 with $NDMG^+$ as the predominant monovalent extracellular cation. Currents evoked with 150 µM AITC in the absence (iii) and presence (iv) of 1.8 mM extracellular Ca^{2+}. Data represent mean ± SEM. ***, p<0.001. n=12 oocytes per condition, two-tailed Student's t-test. (a-c and f) Dashed line denotes 0 µA current. Protocol of condition application indicated above. (e and h) Western blot of lysates from *Xenopus* oocytes used for representative recordings in a-c (e) and f (h) expressing 3xFLAG-tagged hTRPA1 variants, probed using HRP-conjugated anti-FLAG antibody. Blots are representative of one oocyte per injection type (WT hTRPA1 (n=15 (d) and 12 (f)), WT with R919* hTRPA1 (n= 12 (d and f)), and WT with Δ934-1119 hTRPA1 (n-10)). Full blots are included in Supplementary Fig. 14. (a-d, f and g).

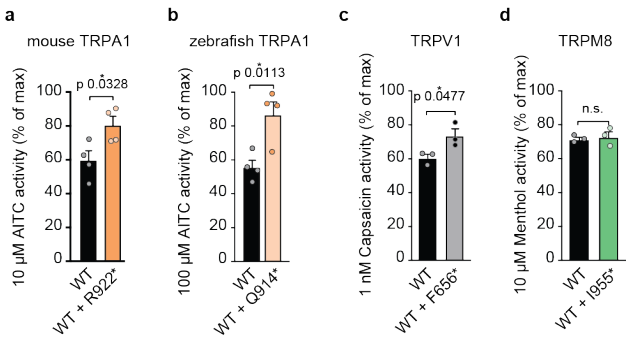

Figure 9. Evolutionary conservation and broad applicability of R919*-conferred channel hyperactivity. (a-d) Quantification of sub-saturating agonist-evoked Fura-2 ratio relative to a saturating agonist response for (a) mouse TRPA1 variants (10 µM AITC relative to 100 µM AITC), (b) zebrafish TRPA1 variants (100 µM AITC relative to 1 mM AITC), (c) human TRPV1 variants (1 nM Capsaicin relative to 1 µM capsaicin), and (d) rat TRPM8 variants (10 µM Menthol relative to 200 µM Menthol). Colors indicate (a) WT (black) or WT with R922* (orange) mouse TRPA1, (b) WT (black) or WT with Q914* (light orange) zebrafish TRPA1, (c) WT (black) or WT with F656* (grey) human TRPV1, and (d) WT (black) or WT with I955* (green) rat TRPM8. Data represent mean ± SEM. *p<0.05, n.s. not significant. n = 4 (a, b) or 3 (c, d) independent experiments, n ≥ 90 cells per transfection condition per experiment, two-tailed Student's t-test.

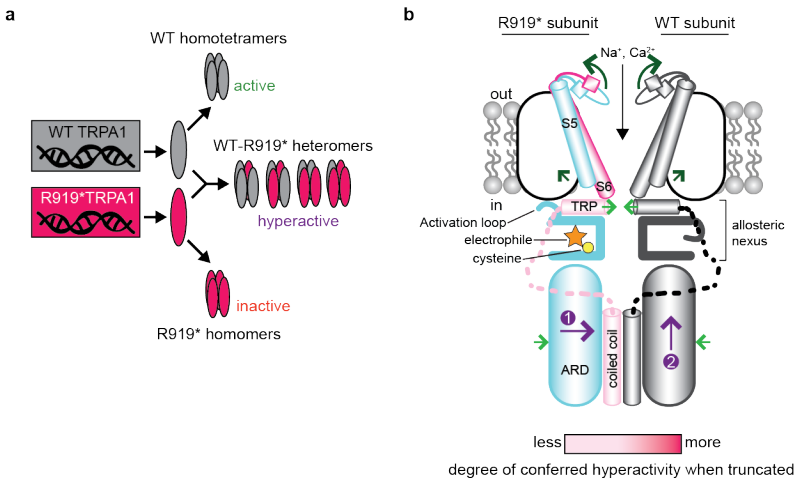

Figure 10. Models of R919*-conferred channel hyperactivity. (a) R919* TRPA1 patients are heterozygotes and carry WT and R919* *TRPA1* copies. WT and R919* hTRPA1 protein subunits can assemble into separate homomeric complexes that are active and inactive, respectively. WT and R919* hTRPA1 subunits may also co-assemble into hyperactive hetero-tetrameric channels of four possible subunit stoichiometries and configurations. We propose these heteromeric channels confer gain-of-function. (b) In WT TRPA1 channels, electrophile agonist-evoked gating involves rearrangements in the cytoplasmic domains including conformational flipping of the activation loop, contraction of the coiled coil and adjacent ankyrin repeat domain (ARD), and a sliding rotation of the TRP domain towards the central channel axis (light green arrows). These conformational changes occur with concerted dilation of the upper and lower gates in the S6 transmembrane helix and selectivity filter, which are coupled through straightening of the S5 transmembrane helix (dark green arrows). Loss of the cytoplasmic C-terminus and S6 transmembrane helix in the R919* mutant contribute to conferred hyperactivity in WT-R919* heteromer channels to different degrees (indicated by gradations of pink). Electrophile modification (orange star) of reactive cysteines (yellow circle) in R919* subunits may communicate channel activation to the pore through associated WT subunits *via* contraction of the ARD and coiled coil domains (purple arrow 1) that could propagate up to the allosteric nexus (purple arrow 2). Two subunits are shown for clarity.

Supplementary Figures

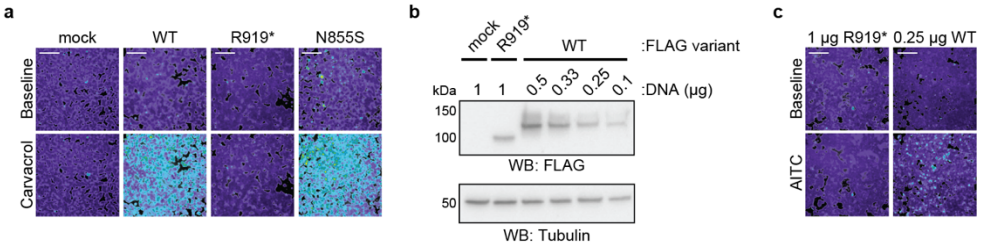

Supplementary Figure 1. The R919* mutant is a nonfunctional TRPA1 natural variant. (a) Ratiometric calcium imaging of HEK293T cells transiently transfected with empty vector (mock), WT hTRPA1, R919* hTRPA1, or N855S hTRPA1. Cells were stimulated with Carvacrol (100 µM). Images are representative of three independent experiments. (b) Western blot of lysates from transiently transfected HEK293T cells expressing 3xFLAG-tagged hTRPA1 variants, probed as in (Fig. 1f). HEK293T cells were transfected with the indicated amount of plasmid (in µg). Blot is representative of three independent experiments. Full blots are included in Supplementary Fig. 16. (c) Ratiometric calcium imaging of HEK293T cells transiently transfected with the indicated amount of 3xFLAG-tagged WT or R919* hTRPA1 to achieve comparable expression levels. Cells were stimulated with AITC (100 µM). Images are representative of three independent experiments. (a and c) Scale bars indicate 100 µm.

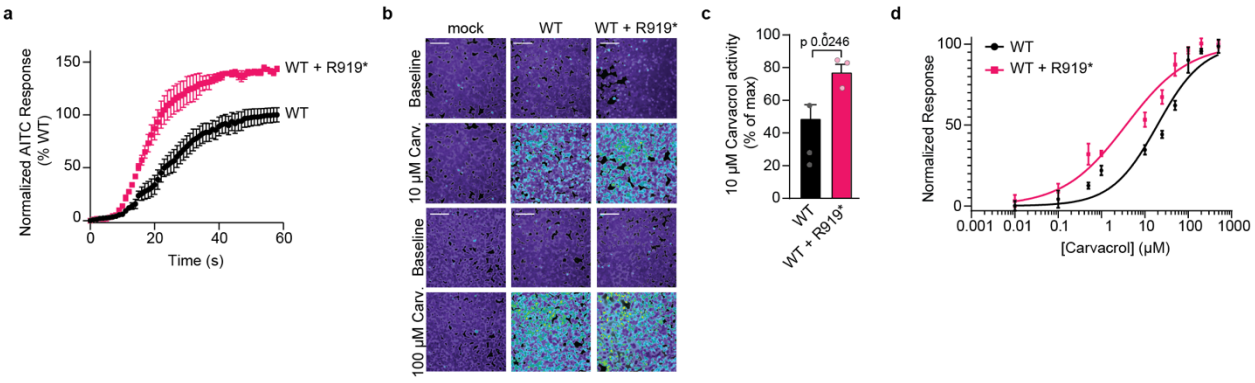

Supplementary Figure 2. The R919* mutant confers hyperactivity when co-expressed with WT TRPA1 subunits. (a) Time-dependent ratiometric calcium imaging responses evoked by 10 µM AITC normalized to maximum response elicited from WT (black) or WT and R919* (pink) hTRPA1-expressing cells. Data represent mean ± SEM. n = 3 independent experiments, n ≥ 90 cells per condition per experiment. (b) Ratiometric calcium imaging of HEK293T cells transiently transfected with empty vector (mock), WT hTRPA1, or WT and R919* hTRPA1. Cells were stimulated with Carvacrol (10 or 100 µM). Images are representatives from three independent experiments. Scale bars indicate 100 µm. (c) Quantification of 10 µM Carvacrol-evoked change in Fura-2 ratio relative to maximum response of each expression condition at 100 µM Carvacrol. Colors as indicated in (a). Data represent mean ± SEM. *p<0.05. n = 4 independent experiments, n ≥ 90 cells per transfection condition per experiment, two-tailed Student's t-test. (d) Dose-response curve of Carvacrol-evoked calcium responses for HEK293T cells transiently transfected with WT hTRPA1 (black) or WT and R919* hTRPA1 (pink). Calcium responses normalized to maximum calcium response to 500 µM Carvacrol. Traces represent the average ± SEM of normalized calcium responses from 3 independent experiments, n = 30 cells per agonist concentration per experiment. Data were fit to a non-linear regression. EC_{50} (95% CI) values are 19.5 µM for WT hTRPA1 (95% CI, 9.6-33.8 µM) and 3.7 µM for WT and R919* hTRPA1 (95% CI, 1.9-6.8 µM).

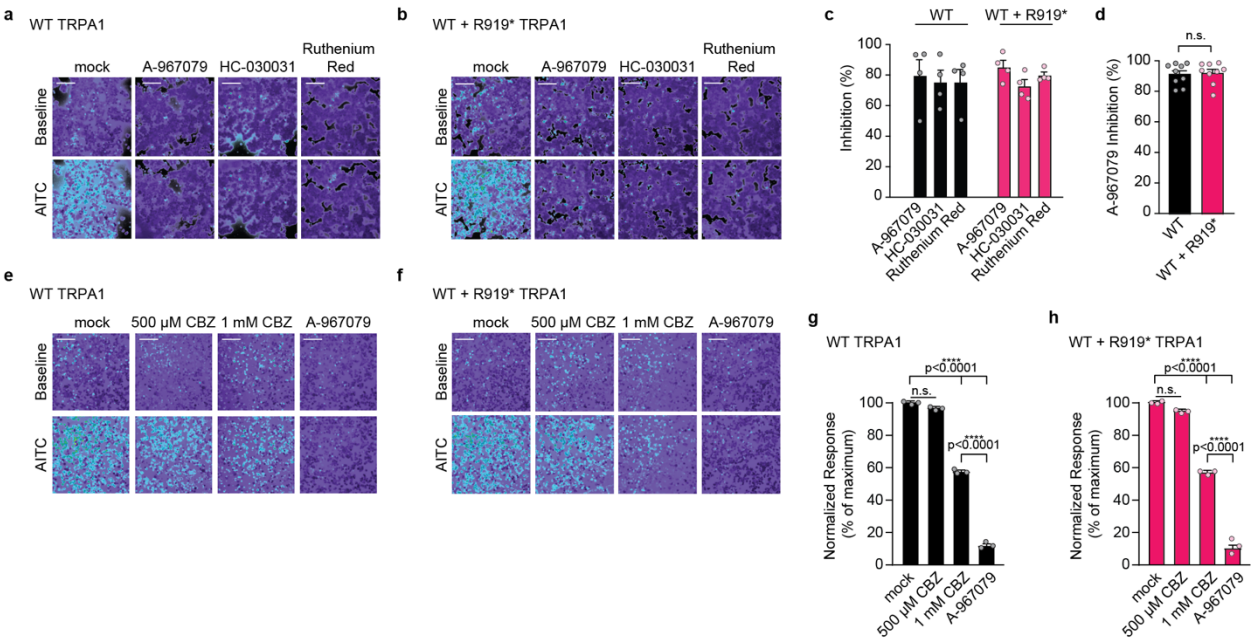

Supplementary Figure 3. WT and WT + R919* channels are inhibited by canonical TRPA1 antagonists and pore blockers. (a-b) Ratiometric calcium imaging of HEK293T cells transiently transfected with (a) WT hTRPA1, or (b) WT and R919* hTRPA1. Cells were pre-treated with Ringer's solution (mock), A-967079 (10 µM), HC-030031 (30 µM), or Ruthenium Red (10 µM). Channels were activated with AITC (100 µM). Images are representatives from four independent experiments. (c) Quantification of antagonist-mediated inhibition of 100 µM AITC-evoked changes in Fura-2 ratio in cells from B and C expressing WT (black) or WT and R919* (pink) hTRPA1. Data represent mean ± SEM of percentage of inhibition of the AITC-evoked maximum response for both transfection types. n = 4 independent experiments, n ≥ 90 cells per condition per experiment. (d) Quantification of percent inhibition of 150 µM AITC-evoked currents in *Xenopus* oocytes expressing WT (black) or WT and R919* (pink) hTRPA1 with 10 µM A-967079 (see Fig. 3a-b). Data represent mean ± SEM. n=9 oocytes per condition. n.s. not significant, two-tailed Student's t-test. (e-f) Ratiometric calcium imaging of HEK293T cells transfected with WT (e) or WT and R919* hTRPA1 (f) pre-treated with either 500 µM or 1 mM carbamazepine. Channels were activated with AITC (100 µM). Images are representatives from three independent experiments. (g-h) Quantification of antagonist-mediated inhibition of 100 µM AITC-evoked changes in Fura-2 ratio in cells from F and G expressing WT (g, black) or WT and R919* (h, pink) hTRPA1. Data represent mean ± SEM of percentage of inhibition of the AITC-evoked maximum response for both transfection types. n = 3 independent experiments, n ≥ 90 cells per condition per experiment. ****, p<0.0001, n.s. not significant. one-way ANOVA with Tukey's *post hoc* analysis. (a, b, e, and f) Scale bars indicate 100 µm.

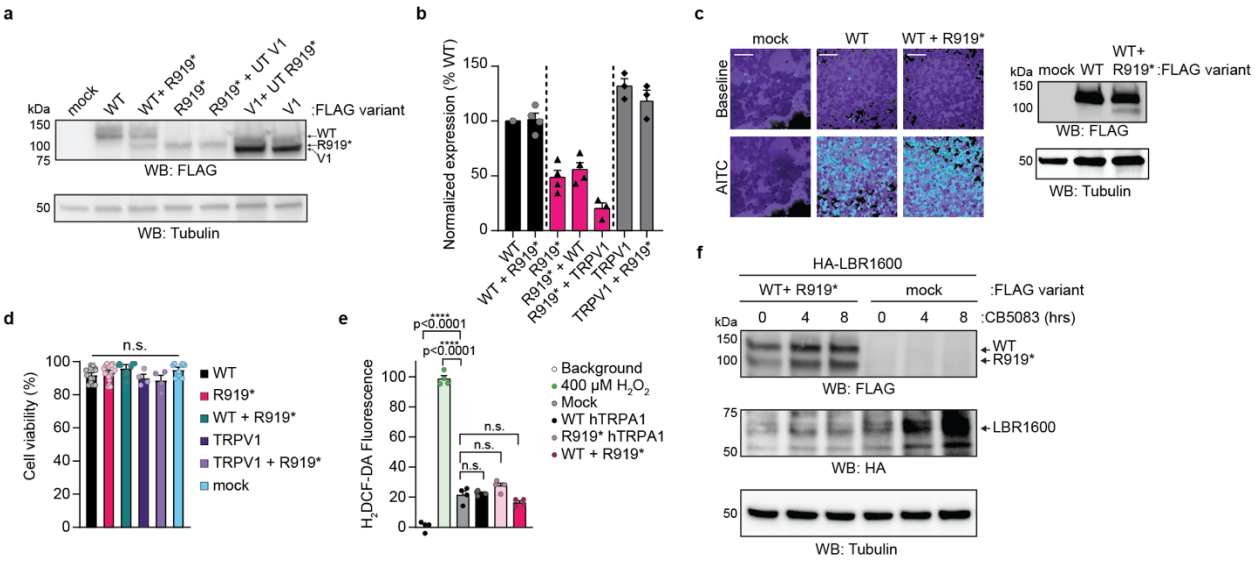

Supplementary Figure 4. The R919* mutant does not affect WT hTRPA1 or TRPV1 expression levels and does not cause general cell stress. (a) Western blot of lysates from transiently transfected HEK293T cells expressing empty vector (mock), 3xFLAG-WT hTRPA1, 3xFLAG-WT and R919* hTRPA1, 3xFLAG-R919* hTRPA1, 3xFLAG-R919* hTRPA1 and untagged (UT) hTRPV1, 3xFLAG-hTRPV1 and untagged (UT) R919* hTRPA1, or 3xFLAG-hTRPV1. Lysates were probed using HRP-conjugated anti-FLAG antibody. Tubulin was the loading control. Blot is representative of three independent experiments. (b) Quantitative analysis of Tubulin-normalized 3xFLAG-tagged hTRPA1 variants or hTRPV1 from (a) relative to WT hTRPA1. Data represent mean ± SEM. n=3 (TRPV1-expressing samples) or 4 (all other samples) independent experiments. Colors indicate WT hTRPA1 (black), R919* (pink) hTRPA1, or WT hTRPV1 (grey) expression in different transfection conditions. (c) Ratiometric calcium imaging (left) and Western blot analysis (right) of HEK293T cells transiently transfected with empty vector (mock), 3xFLAG-WT hTRPA1, or 3xFLAG-WT and R919* hTRPA1. Cells were stimulated with AITC (10 µM). Images are representatives from three independent experiments. Scale bars indicate 100 µm. Lysates were probed using HRP-conjugated anti-FLAG antibody. Tubulin was the loading control. (d) Cell viability of HEK293T cells transiently transfected with the indicated hTRPA1 variants or hTRPV1 was quantified by trypan blue exclusion. Data represent mean ± SEM. n=4 (TRPV1 (dark purple) and TRPV1 with R919* (light purple)), 9 (mock (blue) and WT with R919* (green)), or 17 (WT (black) and R919* (pink)) independent experiments, one-way ANOVA with Bonferroni's *post hoc* analysis. (e) ROS-detection assay to test for oxidative stress. HEK293T cells transfected with empty vector (mock, grey), WT (black), R919* (light pink), or WT and R919* (deep pink) hTRPA1 were loaded with 50 µM H_2DCF-DA dye to detect ROS. Background readings were from buffer only (white). Buffer treated with 400 µM H_2O_2 was the positive control (green) and data were normalized to H_2O_2-evoked H_2DCF-DA fluorescence. Data represent mean ± SEM. n=4 independent experiments, ****, p<0.0001, n.s. not significant. one-way ANOVA with Tukey's *post hoc* analysis. (f) LBR1600 stabilization assay to test for ERAD. To induce ERAD, HEK293T cells co-expressing HA-LBR1600 with empty vector (mock) or 3xFLAG-WT and 3xFLAG R919* hTRPA1 were treated with 10 µM of p97 inhibitor CB5983 for 4 or 8 hrs. Lysates were probed using HRP-conjugated anti-FLAG antibody for TRPA1 or HRP-conjugated anti-HA antibody for LBR1600. Tubulin was the loading control. Blots are representative of three independent experiments. (a, c, and f) Full blots are included in Supplementary Fig. 16.

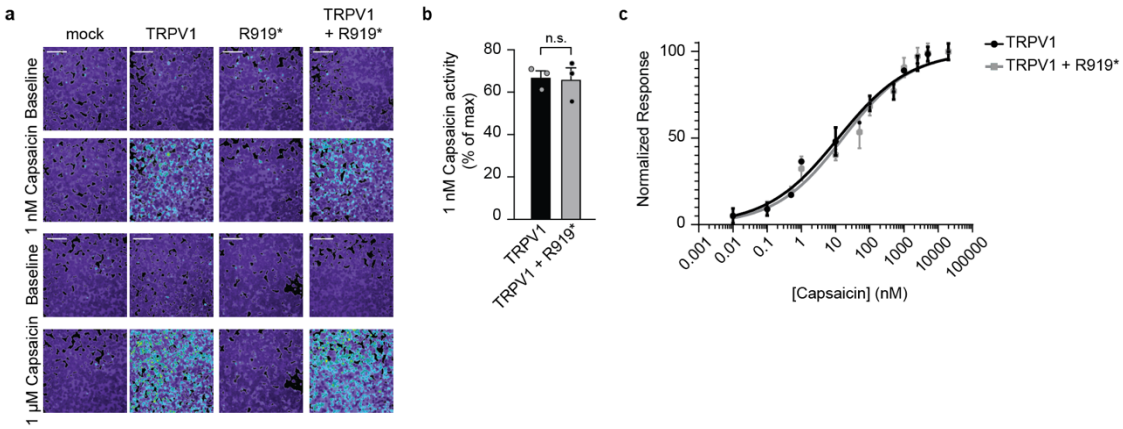

Supplementary Figure 5. The R919* mutant does not affect TRPV1 channel activity. (a) Ratiometric calcium imaging of HEK293T cells transiently transfected with empty vector (mock), hTRPV1, R919* hTRPA1, or hTRPV1 and R919* hTRPA1. Cells were stimulated with 1 nM Capsaicin (top) or 1 µM Capsaicin (bottom). Images are representatives from three independent experiments. Scale bars indicate 100 µm. (b) Quantification of 1 nM Capsaicin-evoked change in Fura-2 ratio relative to maximum response of each expression condition at 1 µM Capsaicin for cells expressing WT hTRPV1 alone (black) or with R919* hTRPA1 (grey). Data represent mean ± SEM. n.s., not significant. n = 3 independent experiments, n ≥ 90 cells per transfection condition per experiment, two-tailed Student's t-test. (c) Dose-response curve of Capsaicin-evoked calcium responses for HEK293T cells transiently transfected with hTRPV1 (black) or hTRPV1 and R919* hTRPA1 (grey). Calcium responses normalized to maximum calcium response at 20 µM Capsaicin. Traces represent the average ± SEM of normalized calcium responses from 3 independent experiments, n = 30 cells per agonist concentration per experiment. Data were fit to a non-linear regression. EC_{50} (95% CI) values are 12.1 nM for hTRPV1 (95% CI: 7.3-19.7 nM) and 16.5 nM for hTRPV1 and R919* hTRPA1 (95% CI: 9.3-28.6 nM).

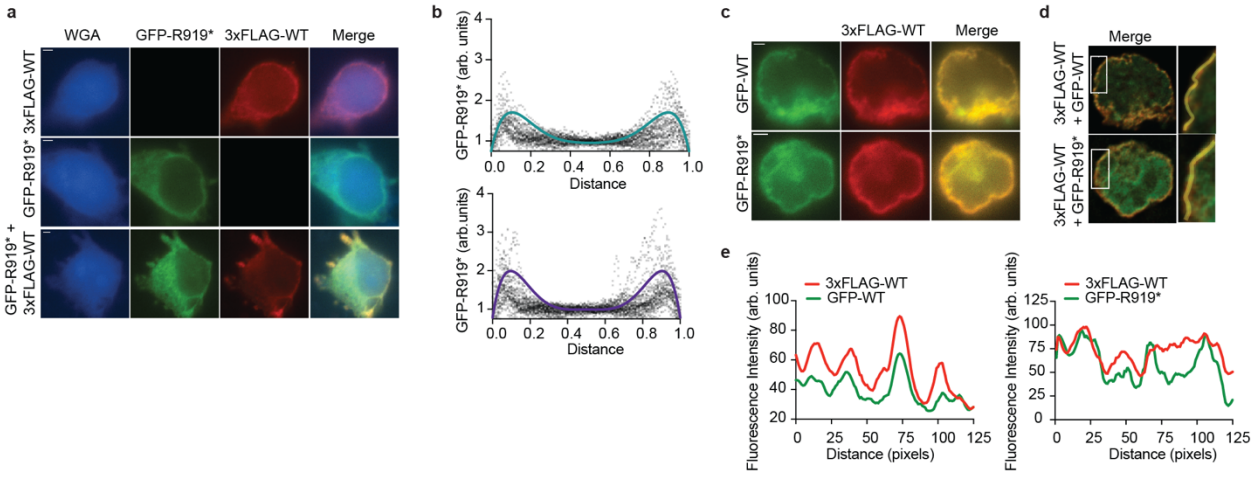

Supplementary Figure 6. Representative immunofluorescence imaging data. (a) Representative raw immunofluorescence images of HEK293T cells transiently transfected with GFP-R919* hTRPA1, 3xFLAG-WT hTRPA1, or GFP-R919* hTRPA1 and 3xFLAG-WT hTRPA1. Cells were stained with anti-GFP (green) and anti-FLAG (red) antibodies. Plasma membrane was labeled with wheat germ agglutinin (blue). Scale bar indicates 2 μm. Images are representative of 3 independent experiments. (b) Combined line scans of HEK293T cell cross-sections with transient transfection of GFP-R919* hTRPA1 (left) or co-transfection of GFP-R919* hTRPA1 and 3xFLAG-WT hTRPA1 (right). Distance and GFP-R919* hTRPA1 fluorescence are normalized relative to total cell width and internal intensity. Representative polynomial lines are overlayed in teal (left) or purple (right). n=30 cells. Arbitrary units, arb. units. (c) Raw images of transiently transfected HEK293T cells used for fluorescence correlation in Fig. 4e. Cells were transiently transfected with 3xFLAG-WT hTRPA1 and GFP-WT hTRPA1 or GFP-R919* hTRPA1, then stained with anti-GFP (green) and anti-FLAG (red) antibodies. Scale bar indicates 2 μm. Images are representative of 3 independent experiments. (d) Deconvolved images of HEK293T cells depicted in (c). Segments of plasma membrane used are magnified (right) for line-scan analysis of red and green signal intensity. Images are representative of 3 independent experiments. (e) Line scans of plasma membrane segments indicated in (d). Arbitrary units, arb. units.

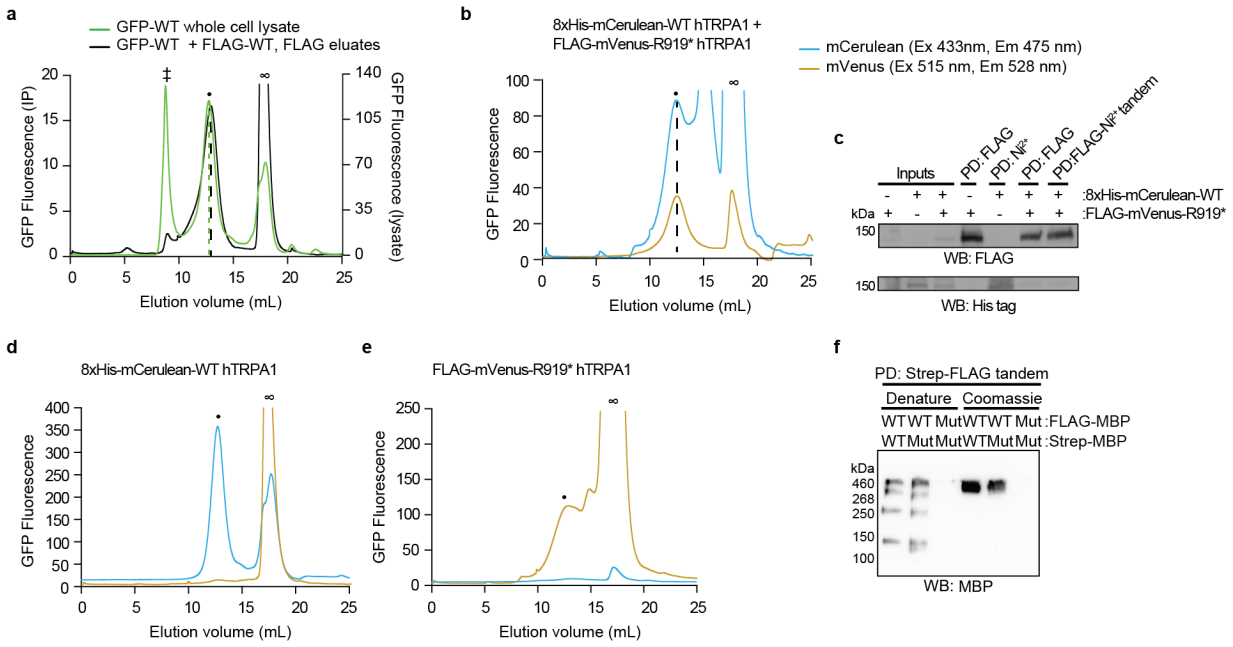

Supplementary Figure 7. FSEC analysis and Native Blue PAGE of WT and WT-R919* TRPA1 complexes. (a) FSEC chromatograms of whole cell lysate from HEK293T cells transiently transfected with GFP-WT hTRPA1 (green trace) or FLAG immunoprecipitated eluates from HEK293T cells transiently co-transfected with GFP-WT hTRPA1 and 3xFLAG-WT hTRPA1 (black trace). Peaks corresponding to void (double cross), tetrameric WT hTRPA1 channels (black dot) and free GFP (infinity symbol) are indicated. Dashed lines denote the center elution volume of each TRPA1 peak. (b) Two-color FSEC chromatogram and (c) Western blot analysis of His-FLAG tandem purified complexes from lysates of HEK293T cells co-expressing 8xHis-mCerulean-WT hTRPA1 and FLAG-mVenus-R919* hTRPA1. Tandem purified eluates were split in two and analyzed at the mCerulean (blue trace) and mVenus (yellow trace) wavelengths. Peaks corresponding to tetrameric hTRPA1 channels (black dot) and free FLAG peptide in elution buffer (infinity symbol) are indicated. Dashed lines denote the center elution volume of each TRPA1 peak. Samples were also analyzed by Western blot (c) using HRP-conjugated anti-FLAG antibody and HRP-conjugated His probe. (d and e) FSEC chromatograms of whole cell lysates from HEK293T cells transiently transfected with 8xHis-mCerulean-WT hTRPA1 (d) or FLAG-mVenus-R919* hTRPA1 (e) analyzed at the mCerulean (blue traces) and mVenus (yellow traces) wavelengths. Peaks corresponding to tetrameric hTRPA1 channels (black dot) and free fluorescent protein (infinity symbol) are indicated. No spectral contamination was observed between mCerulean and mVenus. (a, b, d, and e) Chromatograms are representative of three independent trials. (f) Immunoblotting analysis of tandem-purified WT/WT, WT/R919*, and R919*/R919* hTRPA1 complexes. The indicated FLAG-MBP-tagged and Strep-MBP-tagged constructs were transiently transfected in HEK293T cells. Lysates were tandem purified for Strep- then FLAG-tagged proteins. Eluents were run on a Blue Native PAGE gel after full (left) or partial (right) denaturation. MBP-tagged proteins of tandem purification eluents were probed using anti-MBP antibody. Data representative of 2 independent experiments. (c and f) Full blots are included in Supplementary Fig. 16.

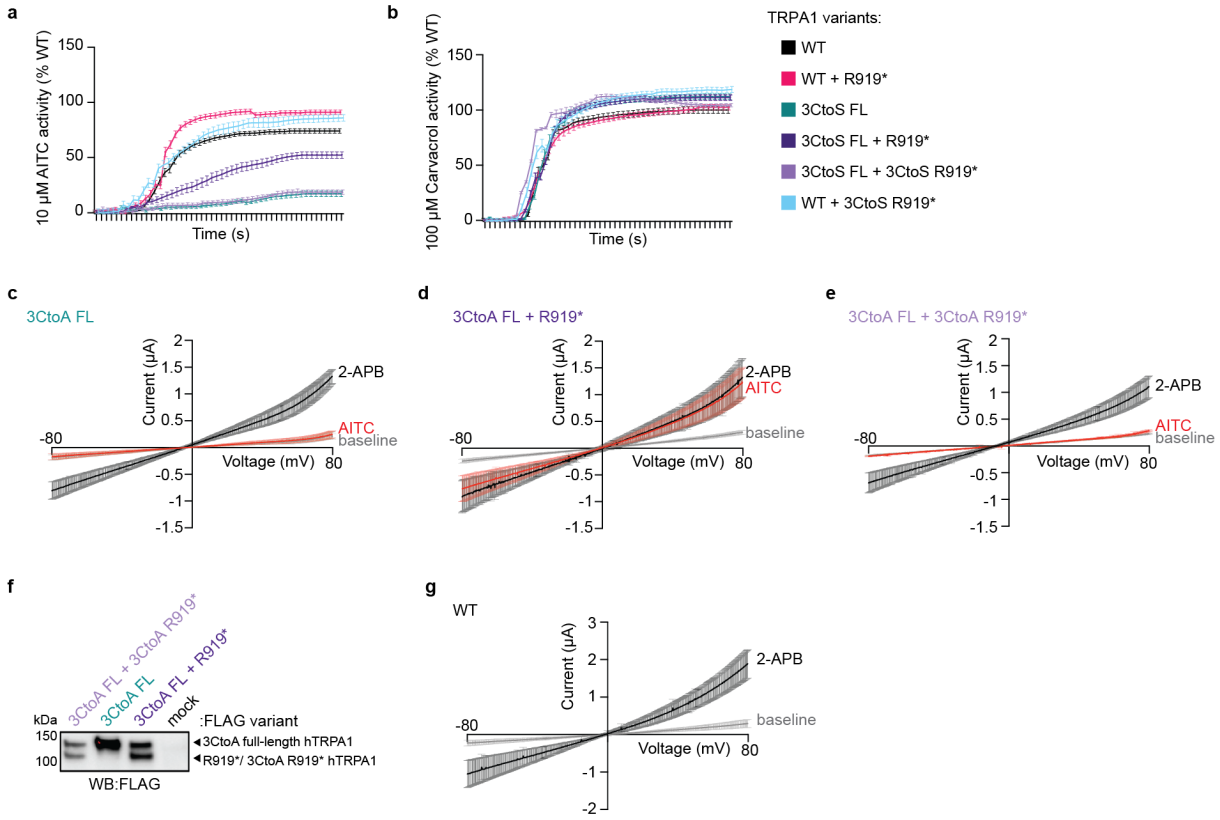

Supplementary Figure 8. R919* TRPA1 subunits directly contribute to functional channels. (a-b) Ratiometric calcium imaging traces of HEK293T cells transiently transfected with WT hTRPA1 (black), 3CtoS FL hTRPA1 (green), WT and R919* hTRPA1 (pink), 3CtoS FL and R919* hTRPA1 (deep purple), 3CtoS FL and 3CtoS R919* hTRPA1 (light purple), or WT and 3CtoS R919* hTRPA1 (blue) from data quantified in Fig. 6b. Cells were stimulated with 10 µM AITC (a) or 100 µM Carvacrol (b). Traces are averages ± SEM of one representative experiment (n = 30 cells) per condition. Data further normalized to WT hTRPA1 response. (c-e) Average I-V relationships from *Xenopus* oocytes presented in Fig. 6c-e expressing 3CtoA hTRPA1 (c, n=7), 3CtoA FL and R919* hTRPA1 (d, n=8), or 3CtoA FL and 3CtoA R919* hTRPA1 (e, n=7) showing baseline currents (grey) and sequentially activated with 150 µM AITC (red) followed by 500 µM 2-APB (black) in the same oocytes. Data represent mean ± SEM. (f) Western blot of lysates from representative oocytes used for recordings in Fig. 6c-e. Lysates were probed using HRP-conjugated anti-FLAG antibody. Blot is representative of one oocyte per injection type (3CtoA hTRPA1 (n=7), 3CtoA FL and R919* hTRPA1 (n=8), 3CtoA FL and 3CtoA R919* hTRPA1 (n=7), or mock (n=7)). Full blot is included in Supplementary Fig. 17. (g) Average I-V relationships from *Xenopus* oocytes expressing WT hTRPA1 showing baseline currents (grey) and those evoked by 500 µM 2-APB (black) in the same oocytes. Data represent mean ± SEM, n=3 independent oocytes. (c-e and g) Extracellular solution contained no calcium.

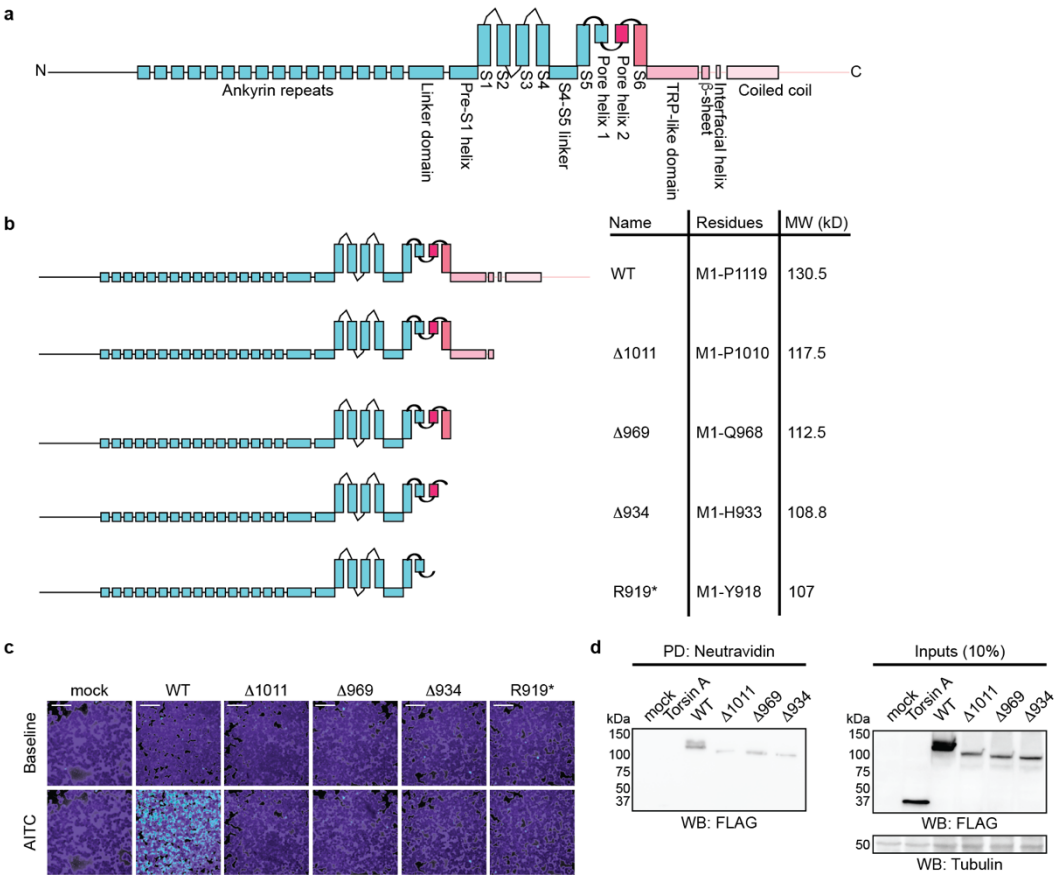

Supplementary Figure 9. Design, activity, expression, and surface localization of C-terminal TRPA1 truncation constructs. (a) Linear diagram depicting major structural domains in a WT hTRPA1 monomer. Colors as indicated in Fig. 7a. (b) Schematic representation and summary of composition of C-terminal TRPA1 truncation mutants assayed in Fig. 7b and c. (c) Ratiometric calcium imaging of HEK293T cells transiently transfected with empty vector (mock) or the indicated 3xFLAG-tagged hTRPA1 constructs. Cells were stimulated with AITC (100 μM, n=60 cells per transfection condition). Scale bars indicate 100 μm. Images representative of three independent experiments. (d) Immunoblotting analysis of 3xFLAG-tagged hTRPA1 constructs or FLAG-Torsin A protein expression in biotin-labeled plasma membranes from transiently transfected HEK293T cells. Biotinylated proteins were precipitated by Neutravidin resin pulldown and probed using HRP-conjugated anti-FLAG antibody. Tubulin from whole cell lysates (10%, inputs) was the loading control. Torsin A was the negative control for plasma membrane localization. Data is representative of three independent experiments. Full blots are included in Supplementary Fig. 17.

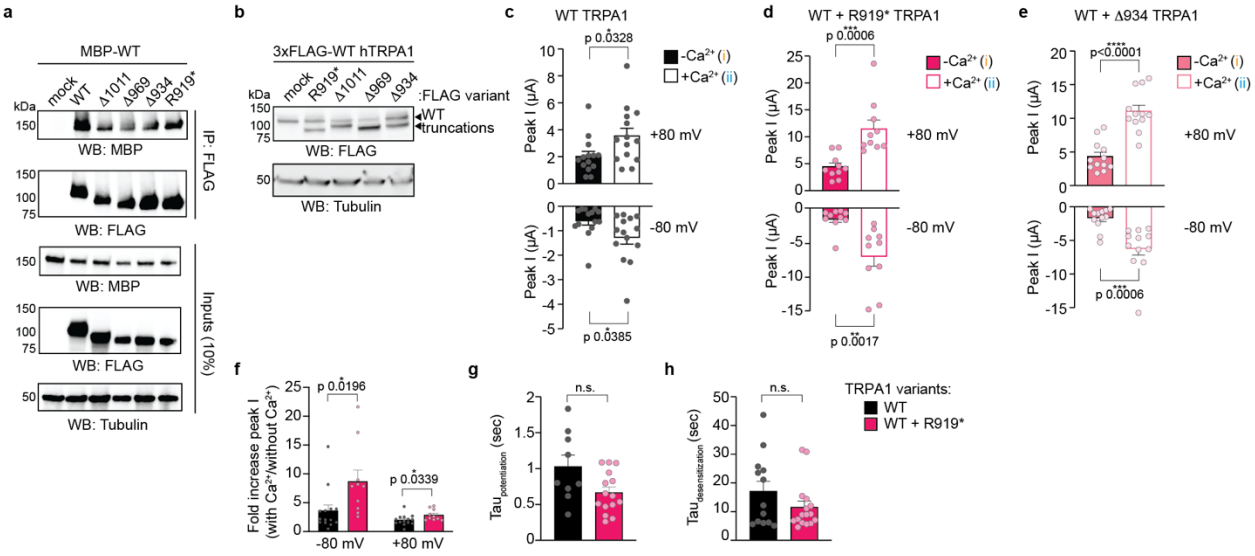

Supplementary Figure 10. Mechanistic dissection of R919*-associated TRPA1 mutant-conferred channel hyperactivity. (a) Immunoblotting analysis of MBP-WT hTRPA1 protein after FLAG immunoprecipitation from lysates of cells co-transfected with empty vector (mock) or 3xFLAG-WT, R919*, or the indicated hTRPA1 C-terminal truncations. Samples were probed using anti-MBP antibody or HRP-conjugated anti-FLAG antibody. Tubulin from whole cell lysates was the loading control. Data is representative of 4 independent experiments. (b) Western blot of lysates from transiently transfected HEK293T cells expressing 3xFLAG-tagged hTRPA1 variants from Fig. 7b, probed using HRP-conjugated anti-FLAG antibody. Tubulin was the loading control. (a-b) Full blots are included in Supplementary Fig. 17. (c-e) Internal analysis of quantified data from Fig. 8d comparing changes to peak current amplitudes at -80 or +80 mV holding potentials in the absence (filled) and presence (open) of 1.8 mM extracellular calcium for WT hTRPA1 (c, black, n=14 independent oocytes), WT and R919* hTRPA1 (d, deep pink, n=10 independent oocytes), or WT and Δ934-1119 hTRPA1 (e, pink, n=12 independent oocytes). Data represent mean ± SEM. ****p<0.0001, ***p<0.001, **p<0.01,*p<0.05. Two-tailed Student's t-test. (f) Quantified degree of potentiation from data in (c) and (d) calculated as -fold increase in the current at -80 or +80 mV after calcium introduction. Data represent mean ± SEM. *p<0.05. n as indicated in c-d, two-tailed Student's t-test. (g-h) Calculated time constants of potentiation (g) and desensitization (h) from fitting data from Fig. 8a and b to a single-exponential function. Data represent mean ± SEM. n.s. not significant. n= 9 (WT) or 15 (WT and R919*) independent oocytes per condition, two-tailed Student's t-test. (f-h) Colors indicate analyses from oocytes expressing WT (black) or WT and R919* (deep pink) hTRPA1.

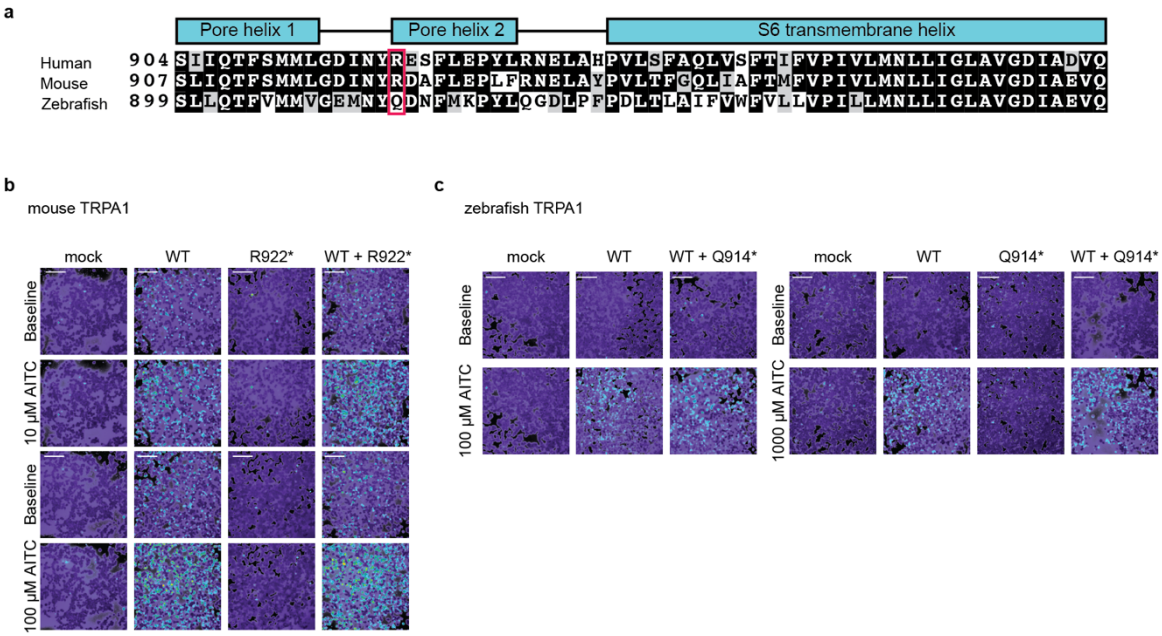

Supplementary Figure 11. Evolutionary conservation of CRAMPT-associated TRPA1 mutant-conferred channel hyperactivity in TRPA1 species orthologues. (a) Alignment of mouse TRPA1 and zebrafish TRPA1 isoform a (zTRPA1a) with the human TRPA1 protein with protein topology indicated above. Amino acid residues are highlighted in black when present in at least two proteins with a similar residue in the third. The human R919 residue is indicated with a pink box. Alignment was built with T-Coffee[92] and BOXSHADE. (b) Representative ratiometric calcium imaging of HEK293T cells transiently transfected with empty vector (mock), WT mTRPA1, R922* mTRPA1, or WT and R922* mTRPA1 from data quantified in Fig. 9a. Cells were stimulated with 10 µM (top) or 100 µM (bottom) AITC. n ≥ 90 cells per concentration. Images representative of four independent experiments. (c) Representative ratiometric calcium imaging of HEK293T cells transiently transfected with empty vector (mock), WT zTRPA1a, Q914* zTRPA1a, or WT and Q914* zTRPA1a from data quantified in Fig. 9b. Cells were stimulated with 100 µM (left) or 1000 µM (right) AITC. n ≥ 90 cells per concentration. Images representative of four independent experiments. (b and c) Scale bars indicate 100 µm.

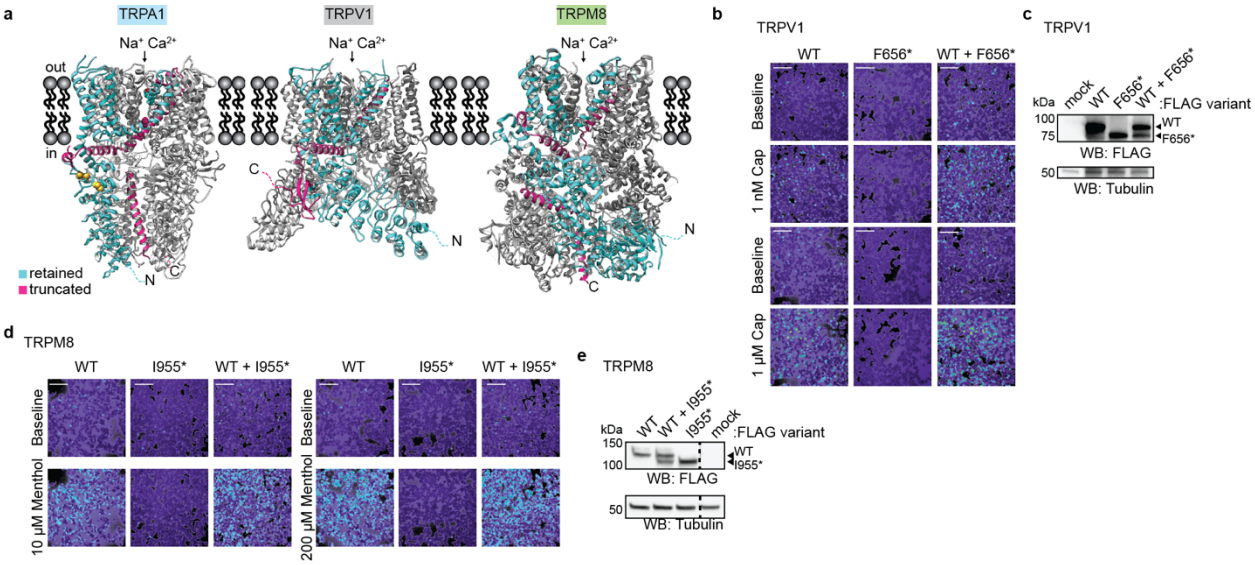

Supplementary Figure 12. A TRPV1 mutant, but not a TRPM8 mutant, lacking the S6 transmembrane helix and cytoplasmic C-terminus confers channel hyperactivity with WT protein. (a) Ribbon diagrams of TRPA1, TRPV1, and TRPM8. Regions retained in R919* hTRPA1, and the S6 and cytoplasmic C-terminus truncations for TRPV1 and TRPM8 are indicated in teal. Regions truncated in these mutants are indicated in pink. Only one subunit is colored for clarity. Models built with the human TRPA1 (PDB: 6V9W), rat TRPV1 (PDB: 7LP9), and *Parus major* TRPM8 (6O6A) Cryo-EM structures in UCSF Chimera. (b) Ratiometric calcium imaging of HEK293T cells transiently transfected with empty vector (mock), 3xFLAG-WT human TRPV1, 3xFLAG-F656* human TRPV1, or 3xFLAG-WT and F656* human TRPV1 from data quantified in Fig. 9c. Cells were stimulated with 1 nM (left) or 1 μM (right) Capsaicin. n ≥ 90 cells per condition. Images are representative of three independent experiments. (c) Western blot of lysates from transiently transfected HEK293T cells from (b), probed using HRP-conjugated anti-FLAG antibody. Tubulin was the loading control. Blot is representative of three independent experiments. (d) Ratiometric calcium imaging of HEK293T cells transiently transfected with empty vector (mock), 3xFLAG-WT rat TRPM8, 3xFLAG-I955* rat TRPM8, or 3xFLAG-WT and I955* rat TRPM8 from data quantified in Fig. 9d. Cells were stimulated with 10 μM (left) or 200 μM (right) Menthol. n ≥ 90 cells per condition. Images are representative of three independent experiments. (e) Western blot of lysates from transiently transfected HEK293T cells from (d), probed using HRP-conjugated anti-FLAG antibody. Tubulin was the loading control. Blot is representative of three independent experiments. (b and d) Scale bars indicate 100 μm. (c and e) Full blots are included in Supplementary Fig. 17.

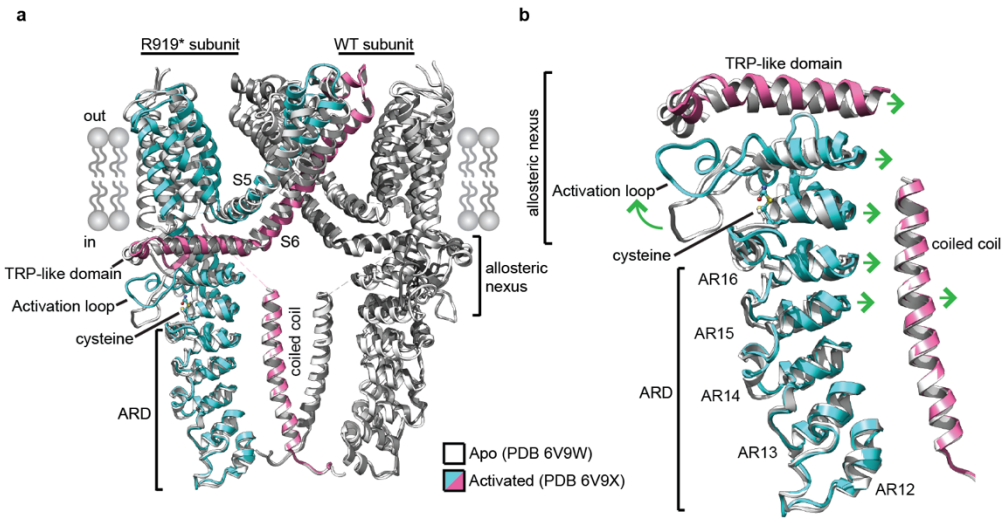

Supplementary Figure 13. Conformational changes associated with TRPA1 activation. (a) Overlay of ribbon diagrams of opposing WT TRPA1 subunits in the closed (Apo, PDB 6V9W, white) and activated (PDB 6V9X, blue/pink or dark gray) states, respectively. The subunit on the left is colored to indicate regions retained in R919* hTRPA1 (teal) and those truncated in this mutant (pink). The subunit on the right (dark grey) is colored to indicate an associated WT TRPA1 subunit. Only two opposing subunits are shown for clarity. Models built with the indicated TRPA1 Cryo-EM structures in UCSF Chimera. (b) Overlay of ribbon diagrams of the TRPA1 allosteric nexus, membrane-proximal ankyrin repeat domain (ARD), and coiled coil colored as in (a). Green arrows indicate regions and direction of gating associated conformational chang

Chapter 3: The TRPA1 C-terminus: A Hotspot for Regulation

Portions of this chapter, especially work presented in Results section v, are part of a manuscript submitted for publication as of November 2023 (Sanders J, Adekanye G, Bali A, Zhang Y, and Paulsen C, **Calmodulin binding is required for calcium mediated TRPA1 desensitization**). See Figure Legend for individual data contributions – unless otherwise indicated, I collected all data presented in this chapter.

3.1 Introduction

As discussed in Chapter 2, TRPA1 is a homotetrameric Ca^{2+}-permeable non-selective cation channel that is expressed at the plasma membrane in a subset of peripheral sensory neurons as well as several non-neuronal tissues. [1,2,3]. Within these tissues, mammalian TRPA1 acts as a ligand-gated chemosensor that can be activated by a plethora of environmental and endogenous chemical agonists. These agonists are known to bind TRPA1 directly to facilitate channel gating – either via covalent modification of conserved cytoplasmic cysteine residues, or by binding within the hydrophobic transmembrane region [4,5]. Existing cryo-EM structures have captured ligands bound to TRPA1, and reveal conformational changes facilitating gating and opening of the channel [6,7].

However, the true spatiotemporal profile of TRPA1 activity in its native cellular environment arises from a more complex and dynamic interplay between not only agonist binding, but also activity-modulating domains and protein-protein interactions. These auxiliary regulatory elements contribute to channel sensitization and desensitization, and can tune TRPA1 activity within a broader physiological context. Incidentally, many of these key regulatory elements in TRPA1 exist within flexible, highly mobile regions that are not resolved in current structures, and remain unidentified.

One of the most abundant and physiologically relevant regulators of TRPA1 activity is calcium, which enters through the channel or may originate from internal stores. Ca^{2+} dynamically regulates TRPA1 activation; initially, Ca^{2+} entry enhances channel activity (*e.g.*, potentiation), which is then followed by rapid inactivation (*e.g.*, desensitization) as cytoplasmic Ca^{2+} levels rise[8]. In this way, Ca^{2+} tightly limits the TRPA1 functional window to prevent spurious initiation of Ca^{2+} signaling pathways and cytotoxicity. In peptidergic nociceptive C fibers expressing TRPA1, Ca^{2+} influx triggers pain signals and the exocytotic release of neuropeptides that initiate neurogenic inflammation and neuronal hypersensitivity [9,10].Hence, determining the regulatory mechanisms of Ca^{2+} influx control can inform rational drug design to alleviate these symptoms. However, the mechanism underlying Ca^{2+} regulation of TRPA1 is poorly understood. Previous work suggests TRPA1 potentiation and desensitization are independent regulatory events that may engage distinct channel elements[8,11]. Direct Ca^{2+} binding sites have been proposed in TRPA1 cytoplasmic and transmembrane domains to control potentiation and/or desensitization. Other studies show TRPA1 binds calmodulin (CaM), a universal Ca^{2+}-sensing protein regulator, near the cytoplasmic TRP domain [12]. However, deep mechanistic insight is lacking to explain whether and how these sites affect Ca^{2+}-regulation and many of these sites remain controversial [6,11,13]. Moreover, some of these proposed Ca^{2+} or CaM binding sites reside within or near TRPA1 key structural domains that contribute to channel gating raising the possibility that their genetic perturbation compromises intrinsic channel structure or function, further complicating interpretation of their effects on Ca^{2+} regulation.

Another mode of TRPA1 regulation is its trafficking to and from the plasma membrane, which directly influences its surface levels and therefore its overall activity. Ion channels in the nervous system, including TRP channels, often undergo heavy trafficking regulation to the plasma membrane, and can be subsequently internalized and/or recycled between the plasma membrane and intracellular compartments [14-16]. The dynamic balance of anterograde and retrograde trafficking of ion channels can become disrupted under certain physiological or disease

conditions, highlighting the importance of understanding how these pathways work in native tissues. For example, during tissue injury, the proinflammatory mediator NGF triggers downstream Src kinase phosphorylation of TRPV1, resulting in enhanced insertion of TRPV1 at the plasma membrane [17]. This leads to the commonly felt symptom of hyperalgesia, or sensitization in areas around the site of injury, where the threshold for sensing pain becomes much lower [18]. In the case of TRPA1, acute activation with covalent agonists have been shown to enhance its plasma membrane localization in a PKA and PLC-dependent manner [19]. Interestingly, this mode of sensitization is dependent on calcium influx through TRPA1 (and not a general elevation of intracellular calcium), suggesting that calcium may mechanistically participate in TRPA1 trafficking pathways. A recent study identified a large multi-domain scaffold protein IQGAP1 as a direct protein partner of TRPA1, as part of a macro-complex capable of facilitating PKA- and calcium-triggered TRPA1 trafficking [20]. However, not much else is known about the specific proteins involved in these pathways, and their effect on TRPA1 function. Identifying protein partners and mechanisms of TRPA1 trafficking will be crucial to understanding channel sensitization and the development of acute and chronic pain and inflammation.

In this Chapter, I will describe how we uncovered a potential hotspot within TRPA1 responsible for multiple regulatory roles. This region is located on the distal disordered C-terminus (DDC) of TRPA1, a previously structurally unresolved region comprised of the final 41 amino acids of the channel. Our data show that the TRPA1 DDC is critical for intrinsic channel gating, contributes to calcium-mediated regulation, channel trafficking, and can bind CaM and other potential protein partners. This work illuminates the importance of a relatively under-studied region of TRPA1, and lays a foundation towards understanding the complex regulation of TRPA1.

3.2 Results

i. The distal disordered C-terminus is required for channel activity

Our attention was first drawn to the distal disordered C-terminus during experiments aimed at understanding the contributions of C-terminal structured elements in the disease mechanism of the truncated R919* mutant (see Chapter 2, section 2.2, viii). For these experiments, we generated a suite of C-terminal truncation mutants in which structured domains of the C-terminus were sequentially deleted (**Figure 1A**; see Chapter 2, Figure 7 and Supplementary Figure 9). My previous studies with these truncations and with the disease mutant R919* supported oligomerization with WT into functional channels (See Chapter 2; Supplementary Figure 9). The smallest truncation within this suite was Δ1079–1119, which lacks the final 41 structurally unresolved amino acids in the protein (3.7% of the total human TRPA1). The goal of these experiments was to determine the elements of the C-terminus that contribute most to hyperactivation, however in doing so we made an unexpected observation. While all the larger deletions conferred increased activity to WT, presumably due to loss of structural tension during channel gating, we noticed that co-expression of Δ1079–1119 conferred a distinct loss of function to WT (**Figure 1B**). This suggested that the Δ1079–1119 construct was missing important regions for channel function, but still possessed all the structural elements that increase the energy barrier to gating. To investigate the intrinsic activity of the Δ1079–1119 construct, I performed calcium imaging experiments with cells only expressing Δ1079–1119, and found no activity, further demonstrating the importance of the final 41 amino acids for channel function (**Figure 1C**)

To functionally dissect the DDC, we made smaller truncations within the Δ1079–1119 at 10-amino acid intervals (**Figure 1A;** green labels). By performing calcium imaging on this refined suite of TRPA1 constructs, I determined that the channel loses activity somewhere between Δ1099 and Δ1109. I then generated truncations within this window, and found TRPA1 only tolerates the loss of its final ~18 residues (Δ1102) before activity is completely lost (**Figure 1C**). Interestingly, the most minimal construct, Δ1109, which is lacking the final 11 amino acids,

exhibits higher basal activity and peak activation than WT, suggesting these last few residues play some sort of inhibitory role in channel function (**Figure 1C**).

ii. Structural context and sequence of the DDC

To better understand the functional role of the DDC, we analyzed its sequence and structural properties. While existing cryo-EM structures do not include the DDC due to its conformational flexibility, we know that within the full tetrameric channel, each of the four TRPA1 monomers contributes a DDC, which originates from the coiled-coil at the cytosol-accessible base of the channel. From the coiled coil, each DDC likely flexibly splays outward, possibly allowing interactions with other cytosolic structured domains of the channel, or cytoplasmic interactor proteins (**Figure 2A**).

In existing TRPA1 structures, resolution of the C-terminus is lost after T1078 [6,21]. The remainder of the DDC is intrinsically disordered, and thus 3D-structure prediction programs such as AlphaFold provide low-confidence structural information. Nonetheless, AlphaFold and other modeling strategies [13] generally agree on the existence of 2 transient helices within the DDC (**Figure 2B**). The first helix is predicted to form at residues Q1088-N1110, and the second at R1102-H1115 (**Figure 2B**).

We performed a WebLogo sequence alignment of 9 TRPA1 orthologs aligned to residues 1073 -1112 of TRPA1. The sequence alignment reveals several highly conserved residues, distributed throughout both flexible and putative structured portions of the DDC (**Figure 2 B,C)**. Conserved residues loosely cluster in 4 different regions (**Figure 2C**), which we designated as follows, based on amino acid composition and predicted structure: Region 1 (ie: ‘acidic cluster’), Region 2 (ie: ‘pre-helix 1’), Region 3 (ie: ‘helix 1’), and finally Region 4 (ie: ‘helix 2’) which is the only conserved region that is dispensable for channel activity (**Figure 1C**)

To empirically assess the secondary structure of the DDC, I performed circular dichroism experiments on a purified TRPA1 DDC peptide containing residues 1079-1119. The resulting spectra indicates alpha helical character in 30% of the total DDC sequence (**Figure 2D**), in

agreement with predicted structures. This provides the first experimental evidence outside of predictive modeling that the DDC contains alpha helices.

iii. A conserved acidic cluster in the TRPA1 DDC is important for channel activity, trafficking and processing

I sought to dissect the functional roles of these conserved regions within the DDC, starting with the acidic cluster in Region 1. The acidic cluster begins at the C-terminal coiled coil and contains a strongly conserved string of acidic, negatively charged residues. In the tetrameric structure, 4 of these acidic cluster sequences are positioned in close proximity, resulting in a particularly dense region of negative charge at the base of the coiled coil (**Figure 2A,B**). To determine how acidic residues affected channel function, I generated a suite of 3xFLAG-tagged human TRPA1 variants that partially or fully neutralized the acidic residues in Region 1 to the polar residue serine (**Figure 3A**). The isoelectric points (pI) of aspartic acid and glutamic acid are 2.77 and 3.22, respectively[22]. Thus I also generated a hyper-acidic variant (DTDDDD), in which glutamic acid residues are changed to aspartic acids, as well as ETEEEE to test the importance of the degree of acidity in Region 1 on channel function.

To examine the functional effects of the acidic cluster on channel activity, I assayed channel activity using Fura-2 ratiometric calcium imaging on HEK293T cells expressing acidic cluster variants (**Figure 3B**). Strikingly, neither ETSDSD nor STSSSS showed any channel activity in response to AITC. Single-point neutralization constructs ETSDED and ETEDSD showed very minimal channel activity compared to WT TRPA1. Both of the charge-maintaining DTDDDD and ETEEEE variants showed activity, with notably higher activity in the hyper-acidic DTDDDD variant compared to WT (**Figure 3B**).

When expressed in heterologous HEK293T cells, both partially (ETSDSD) and fully (STSSSS) neutralized acidic cluster variant show expression in a Western blot, as does the hyperacidic DTDDDD variant (**Figure 3C**). Notably, both WT and DTDDDD TRPA1 appear as doublets in Western blots, corresponding to mature (upper band) and immature (lower band) N-

glycosylation of the channel as it progresses through the secretory pathway *enroute* to the plasma membrane [23]. Indeed, a TRPA1 mutant in which the N747 and N753 glycosylation residues are mutated to Gln (NN>QQ) shows no complex mature glycan bands (**Figure 3C**). ETSDSD and STSSSS exhibit a lack of complex glycosylation, suggesting that they undergo differential intracellular processing (**Figure 3C**). This suggests that the acidic cluster may play a role in channel sorting and trafficking.

In other proteins, including membrane proteins such as TRPP2, mGluR5, Serinc3, and K^+ channels, cytosolic acidic motifs can serve as linear sorting signals for channel trafficking and internalization [24-26]. To verify whether the acidic cluster affects plasma membrane localization of TRPA1, I performed surface biotinylation on HEK293T cells expressing acidic cluster variants. Strikingly, partial or full neutralization of the acidic cluster resulted in a significant decrease in surface population (**Figure 3D**). I also performed immunofluorescence imaging on Neuro2A cells transiently transfected with WT, ETSDSD, and DTDDDD TRPA1 variants. While both WT and DTDDDD TRPA1 primarily localized at the plasma membrane, the ETSDSD variant exhibited distinct intracellular localization (**Figure 3E**). Together, these results indicate that loss of charge at the acidic cluster perturbs normal processing and trafficking of TRPA1, supporting a putative role of the acidic cluster in regulation of TRPA1 plasma membrane levels.

iv. More than a sorting signal? Acidic cluster location and charge is vital for TRPA1 activity

It is possible that the observed loss of activity and surface localization in acidic cluster neutralization variants is due to the acidic cluster acting as a signal for forward trafficking or sorting in the Golgi (**Figure 3**). Generally, trafficking motifs in flexible protein regions can still facilitate sorting if their location is moved to other cytosol-accessible regions of the protein, or even onto an entirely different protein [27,28]. To test this, I used site-directed mutagenesis to delete the native acidic cluster (ΔAC) and transfer its sequence to various cytosol-accessible flexible regions of TRPA1, including the disordered N-terminus (ΔAC; disN-AC), flexible ankyrin 11 (Δ AC; Ank11-

AC), and disordered portions of the C-terminal DDC (ΔAC;1090-AC, ΔAC;1100-AC and ΔAC;1115-AC). In all cases, the channel did not tolerate re-positioning of the acidic cluster, and was completely inactive (**Figure 4A**), indicating that while the acidic cluster does play a role in channel trafficking, it is likely not just a trafficking motif, and may have an important structural or conformational contribution to channel activity.

One possibility is that all four acidic clusters at the base of the tetrameric TRPA1 channel, being in close proximity near their respective coiled coils, exert electrostatic repulsion on each other, driving each DDC outwards from the center of the channel (**Figure 2A,B**). Perhaps this splayed distribution of the DDCs is required for proper TRPA1 activity. To test this model, I mutagenized the acidic cluster aspartic and glutamic acids into arginine and lysine, respectively. This variant was also inactive, hinting that simple electrostatic repulsion alone does not account for the structural contribution of the acidic cluster to activation (**Figure 4B**). Taken together, these results strongly suggest that the location, charge, and structural context of the acidic cluster within the DDC of TRPA1 is vital to channel function.

v. Both the acidic cluster and calmodulin binding site regulate calcium-mediated desensitization

Besides having a putative role as a trafficking or sorting motif, previous *in silico* analysis of the TRPA1 acidic cluster predict a Ca^{2+} binding site, largely facilitated by its aspartic acid residues [13]. From my own Ca^{2+} imaging experiments, we observed that the hyper-acidic DTDDDD variant exhibited notably higher activity compared to WT TRPA1 (**Figure 3B**), opening up the possibility that the acidic cluster could bind Ca^{2+} and in a manner that alters channel Ca^{2+} handling.

To examine Ca^{2+} handling of acidic cluster variants, I injected WT and DTDDDD TRPA1 cRNA into *Xenopus laevis* oocytes and assayed channel activity by whole-cell TEVC recordings. In the TEVC protocol, channels were activated with AITC in the absence of Ca^{2+}, followed by addition of 1.8mM Ca^{2+} to the extracellular buffer to induce potentiation and desensitization [8].

Remarkably, the hyper-acidic DTDDDD exhibits ~5x slower Ca^{2+}-mediated desensitization, as well as ~3x increases in peak inward Ca^{2+} current amplitude (**Figure 5A,B,I**). In the absence of Ca^{2+}, DTDDDD TRPA1 does not exhibit any significant differences in channel activity (**Figure 5A, B**). This data suggests that the acidic cluster does indeed contribute to intrinsic TRPA1 Ca^{2+} handling properties.

The mechanisms by which Ca^{2+} regulates TRPA1 activity likely involve multiple sites in the channel. Recent work by other members in our lab has revealed that different regions within the DDC may work in concert to promote Ca^{2+} handling. Conserved Region 4 residues on the C-terminal end of the DDC (**Figure 2B,C**) participate in direct binding to calmodulin (CaM), as evidenced by *in vitro* CaM-agarose pulldown assays on TRPA1 DDC truncation constructs (**Figure 5C**). This interaction has been confirmed in our lab by isothermal calorimetry and size-exclusion chromatography (not shown- see Sanders et al). *In silico* AlphaFold modeling predicts association of Region 4 of the DDC with the CaM C-lobe as an alpha helix (**Figure 5D**). This putative interaction is facilitated by conserved hyrdrophobic residues W1103A, V1106, L1107, and V1110, and by flanking positively charged residues R1099 and R1102, and K1111 (**Figure 5D**). To show that TPRA1 and CaM interact in cells, I performed immunofluorescence imaging on Neuro2A cells co-expressing V5-tagged CaM and 3xFLAG-tagged WT or Δ1109 TRPA1. While WT TRPA1 and CaM co-localize at the cell surface, Region 4 deletion mutant Δ1109 TRPA1 lacks the full conserved sequence needed for CaM binding, and therefore does not exhibit clear co-localization with CaM (**Figure 5E**). Importantly, CaM binding suppresses TRPA1 activity, and our data shows that loss of the CaM binding site via deletion (Δ1109) or single point mutation (W1103A) results in hyperactivity due to prolonged Ca^{2+}-mediated desensitization, similar to functional profiles observed with the hyper-acidic DTDDDD variant (**Figure 1C and 5F,I**).

Given that DTDDDD activity profiles mimic the loss of CaM binding, we then asked whether mutations in the acidic cluster were somehow preventing CaM binding at the DDC. CaM-agarose pulldown assays on acidic cluster variants showed that they still retain CaM binding

(**Figure 5G**), suggesting that the acidic cluster is not likely to allosterically interfere with CaM binding to TRPA1. To determine whether both the acidic cluster and CaM binding motifs are part of the same mechanism of prolonged Ca^{2+}-mediated desensitization, I simultaneously mutagenized both the acidic cluster and CaM binding site in TRPA1 (DTDDDD+W1103A), and analyzed this variant with TEVC. DTDDDD+W1103A did not exhibit an additively slower desensitization rate compared to DTDDDD or W1103A individually (**Figure 5H,I**), suggesting that both the CaM binding site and the acidic cluster participate in the same molecular mechanism for Ca^{2+}-mediated desensitization. Taken together, our data indicates cross-talk between different regions of the DDC to facilitate Ca^{2+} handling, and that conformational changes at the DDC can propagate upwards into structured domains of the channel to influence gating and global channel properties.

vi. Other conserved regions in the DDC are essential for TRPA1 function

In conjunction with my studies on the acidic cluster and CaM binding site, I sought to determine the roles of remaining regions of interest in the DDC: Regions 2 and 3. Region 2 (ie: 'pre-helix 1') contains a highly conserved F1087 and Q1088, and initiates the first predicted DDC alpha helix (**Figure 2B,C**). Region 3 (ie: 'helix 1') is largely comprised of helix-forming residues, where positive and negative charges are well-conserved across multiple orthologs (**Figure 2B,C**).

I began by generating a suite of single-point variants targeting residues in Region 2 (Q1088) and Region 3 (K1092, K1093, E1094, and E1097) in human TRPA1, and screening their activity with Fura-2 ratiometric Ca^{2+} imaging (**Figure 6A, B**). I also tested a TRPA1 variant in which residues 1089-1099 were replaced with a flexible Gly-Ser linker to remove helical secondary structure within Region 3, but preserve the overall length of the DDC.

Any perturbation to Region 3 charged residues resulted in complete or near-complete loss of channel activity (**Figure 6B**). Circular dichroism experiments I conducted on a purified DDC peptide with all four of the Region 3 charged residues fully neutralized showed that while the WT sequence has approximately 30% helicity, neutralization of the charged Region 3 residues

decreases helical content to 18%. (**Figure 6C**) This provides the first experimental evidence outside of predictive modeling that Region 3 forms a helix, and that this helix can be perturbed by mutagenesis of conserved residues in Region 3. Together, these results show that the secondary structure at Region 3 has an important role to play in channel activity. Intriguingly, substitution of Q1088 in Region 2 with uncharged, charged, polar, or bulky hydrophobic residues had an opposite effect - all resulted in some degree of channel hyperactivity with the following trend: Q (WT) ≤ A < S/L < F (**Figure 6B**).

To assess whether Regions 2 and 3 also contribute to channel trafficking, I performed surface biotinylation on all Region 3 variants, as well as Q1088L and Q1088F (the most active of the Region 2 variants) (**Figure 6D**). For comparative purposes, I also included the trafficking-deficient STSSSS acidic cluster variant. While the Q1088 mutations did not seem to influence plasma membrane levels, the Region 3 helix-perturbing mutations exhibit reduced surface localization and complex glycosylation, though not to the same extent as the STSSSSS variant. Region 3 helix-forming residues may therefore contribute to channel trafficking.

To further assess Ca^{2+} handling of the hyperactive Q1088 variants, I performed whole-cell TEVC in Xenopus oocytes on variants exhibiting the weakest (Q1088A) and strongest (Q1088F) hyperactivation. TEVC revealed significant increases in peak calcium current amplitudes, especially for Q1088F (**Figure 6E**), as well as moderately elongated desensitization (**Figure 6F**). These changes, however, are not as drastic as other hyperactivating mutations in the DDC, such as DTDDDD or W1103A (**Figure 5**). This data indicates that the Q1088 residue, which leads into the first DDC helix, serves a distinct functional purpose from its subsequent helix-forming residues and may contribute to allosteric mechanisms involving the Region 1 acidic cluster and Region 4 CaM binding site.

3.3 Discussion

In all existing cryo-EM structures of human TRPA1, many flexible and disordered domains remain unresolved and their function is poorly understood. Our data provides strong evidence that the structurally unresolved distal disordered C-terminus is a regulatory hotspot chock-full of conserved regions that are indispensable for proper channel function. We initially identified 4 regions of interest within the DDC based on sequence conservation: Region 1 (acidic cluster), Region 2 (pre-helix 1), Region 3 (helix 1), and Region 4 ('helix 2'). Mutagenic perturbation of any of these regions individually has drastic consequences for channel activity.

TRPA1 variants neutralizing the Region 1 acidic cluster lead to inactive channels that also exhibit decreased trafficking to the plasma membrane. Even when the acidic cluster is transferred to other flexible domains of TRPA1, the channel remains inactive. Neutralization of Region 3 putative helix residues also silences channel activity and reduces plasma membrane levels, but to a lesser extent than acidic cluster neutralization does. These results support a model in which the acidic cluster is a linchpin within the DDC, with potential contributions from the Region 3 transient helix. The position of the acidic cluster at the beginning of the flexible and disordered portion of the C-terminus perhaps may govern the overall dynamics and orientation of the DDC within the channel, or may be crucial for propagating conformational changes at the DDC to the coiled-coil and structured C-terminal elements.

However, it is currently unclear how exactly perturbations within the DDC also influence trafficking. One possibility is that disrupting residues in Region 1 and 3 of the DDC can cause misfolding of TRPA1, thus resulting in intracellular retention and inactive channels. Another possibility is that the acidic cluster serves a dual purpose as a both a trafficking signal in addition to a structural role. In other proteins, acidic cluster sorting sequences may be flanked by a phosphorylated serine residue [25,26] . These particular motifs have been shown to bind clathrin adaptor protein (AP) complexes either by direct interaction, or more commonly via intermediary adaptors named phosphofurin acidic cluster sorting protein (PACS) 1 and 2. Interestingly, the

TRPA1 acidic cluster sequence is preceded by a strongly conserved serine residue that is a predicted target of casein kinase (CK2) [13,29], in line with a potential ability of the acidic cluster to "moonlight" as a sorting signal via PACS binding in addition to its structural role.

On the other hand, the DTDDDD hyper-acidic variant of TRPA1 raises a different set of interesting questions. TEVC recordings show that DTDDDD TRPA1 is hyper active profile due to severely prolonged calcium-mediated desensitization. The substitution of E1077 and E1079 with aspartic acid residues would result in 1) reduced side-chain size, which may have effects on the steric and conformational sampling of the DDC and 2) increased local acidity, which could affect electrostatic interactions at the acidic cluster.

Since the functional difference between WT and DTDDDD TRPA1 is calcium-specific, a possible explanation could be that the acidic cluster participates in direct coordination of calcium, which would be altered (presumably even strengthened) by the addition of aspartic acids. Indeed, strings of conserved negatively charged residues within soluble intrinsically disordered protein regions have been reported as calcium-binding motifs, with aspartic acid residues possessing a higher affinity for calcium coordination than glutamic acid [30]. Prior to the existence of solved TRPA1 structures, Sura et al performed *in silico* modeling of the TRPA1 acidic cluster, using a calcium-binding bowl from BK channels as a structural template [13]. These data predicted calcium binding at the acidic cluster driven by its aspartic acid residues, which are predicted to form a transient helix upon calcium binding. Other studies suggest that it is entirely possible the acidic residues can still bind calcium without eliciting any major secondary structure changes [30]. What remains a mystery within this model is whether calcium binding at the acidic cluster, if it indeed occurs, would contribute to channel activation or inhibition, and whether aspartic acid substitutions at E1077 and E1079 cause hyperactivity by enhancing calcium binding at a potentiation site or by disrupting calcium coordination and reducing structural packing at a desensitization site.

Indeed, the long-sought mechanism of calcium regulation in TRPA1 is likely polymodal and complex. Combined work done by myself and other lab colleagues shows that Region 4 of

the DDC contains a previously unidentified, high-affinity binding site for CaM, which we have named the CaMBS. CaM is a universal calcium sensor that regulates the activity of hundreds of effector proteins including many ion channels. We have determined that CaM stably associates with TRPA1 at basal conditions in cells. CaM binding to TRPA1 inhibits channel activity, and disruption of the CaM-TRPA1 interaction via CaMBS mutations results in hyperactive channels exhibiting a drastic deceleration of calcium-mediated desensitization. Remarkably, the CaMBS mutant activity profile matches that of DTDDDD TRPA1, and introducing both CaMBS and DTDDDD mutations onto TRPA1 does not additively extend calcium-mediated desensitization, suggesting a shared mechanism. While the acidic cluster site does not appear to have any bearing on CaM binding at the CaMBS (**Figure 5G**), it is possible that CaM binding at the CaMBS may induce an allosteric conformational change that positions or modulates the acidic cluster as part of channel inhibition. The allosteric effects imposed by CaM binding may then be propagated through the acidic cluster upwards to the coiled-coil, and further still to modulate global conformational change in the channel. Future structural and functional work are needed to identify and characterize TRPA1 calcium binding sites, to determine how calcium binding triggers TRPA1 potentiation/desensitization, and to uncover how CaM influences this process. Future studies must also examine whether other regions of the DDC may also be part of this signal propagation, as some of my findings seem to suggest (**Figure 6**).

Overall, this work forms a foundation towards understanding the role of the TRPA1 DDC in channel regulation. In particular, we have begun to determine specific functional roles of the conserved acidic cluster and CaMBS. Taken together, our findings illuminate how a small, structurally unresolved region of TRPA1 can so drastically influence multiple channel properties in unexpected ways. We believe that continued study of the TRPA1 DDC will be crucial to elucidating poorly understood TRPA1 regulatory mechanisms such as Ca^{2+}-mediated potentiation/desensitization and channel trafficking.

3.4 Materials and Methods

Cloning and Protein Expression

All mutants including TRPA1 truncation constructs, acidic cluster variants, and CaM binding site mutants were generated using QuikChange Lightning site-directed mutagenesis. For calcium imaging experiments, 3xFLAG-tagged TRPA1 in p3xFLAG-eYFP-CMV-7.1 vector were used. For expression in *Xenopus laevis* oocytes, 3xFLAG-hTRPA1 variant genes were subcloned into the combined mammalian/oocyte expression vector pMO (modified from pcDNA3 - obtained from David Julius) prior to generating cRNAs. 8xHis-MBP pFastBac1 modified with a CMV promoter human $TRPA1^{1077\text{-}1119}$ used for purification and CD spectroscopy was created by introducing a BamHI site at the -1 position of the codon encoding $TRPA1^{1089}$ and digesting the plasmid with BamHI restriction enzyme followed by gel purification. The linearized vector segment was then transformed into XL-10 Gold cells resulting in a repaired vector. Lightning site-directed mutagenesis kits from Agilent. All DNA primers were ordered from ThermoFisher and all constructs were sequence-verified using the Yale School of Medicine Keck DNA Sequencing Facility.

Human embryonic kidney cells (HEK293T, ATCC CRL-3216) were cultured in Dulbecco's modified Eagle's medium (DMEM; Invitrogen) supplemented with 10% calf serum for all experiments, and 1x Penicillin-Streptomycin (Invitrogen) at 37°C and 5% CO_2. Cells were grown to ~85-95% confluence before splitting for experiments or propagation. For immunofluorescence assays, Neuro2A cells were cultured in Dulbecco's modified Eagle's medium (DMEM; Invitrogen) supplemented with 10% FBS, 1x Penicillin-Streptomycin (Invitrogen), and 1x MEM non-essential amino acids (Gibco) at 37°C and 5% CO_2 Plasmids were transfected into cultured cells with jetPRIME (Polyplus) according to manufacturer protocols and cells were used for all experiments within 48 hours of transfection.

Ratiometric Calcium Imaging

After 40-48 hours transient transfection, HEK293T cells were loaded with 10 µg/mL Fura-2-acetoxymethylester (Thermo Fisher) in physiological Ringer's buffer (in mM: 120 NaCl, 5 KCl, 2 $CaCl_2$, 25 $NaHCO_3$, 1 $MgCl_2$, 5.5 HEPES, 1 D-glucose, pH 7.4; Boston BioProducts) for ratiometric calcium imaging. Activity of TRPA1 was monitored using a Zeiss Axio Observer 7 inverted microscope with a Hamamatsu Flash sCMOS camera at 20x objective. Dual images (340 and 380 nm excitation, 510 nm emission) were collected and pseudocolour ratiometric images were monitored during the experiment (Metafluor software). Following agonist application, cells were imaged for 45-100 s.

AITC and other TRPA1 agonists were all purchased from Sigma and were freshly prepared as stocks at 4x the desired concentration in 1% DMSO and Ringer's solution. 5 µL 4x agonist was added to wells containing 15 µL Ringer's solution to give the final 1x desired concentration.

Oocyte Electrophysiology

pMO vectors carrying 3xFLAG-tagged hTRPA1 constructs were linearized with PmeI, cRNAs were generated by *in vitro* transcription with the mMessage mMachine T7 transcription kit (Thermo) according to the manufacturer's protocol and were purified with a RNeasy kit (Qiagen). cRNA transcripts were microinjected into surgically extracted *Xenopus laevis* oocytes (Ecocyte) with a Nanoject III (Harvard Apparatus). Oocytes were injected with 0.1 ng of cRNA per cell, and whole-cell currents were measured 24-48 hours post-injection using two-electrode voltage clamp (TEVC). Currents were measured using an OC-725D amplifier (Warner Instruments) delivering a ramp protocol from -100mV to +100mV applied every second. Microelectrodes were pulled from borosilicate glass capillary tubes and filled with 3M KCl. Microelectrode resistances of 0.7-1.2 MΩ were used for all experiments. Bath solution contained (in mM) 93.5 NaCl, 2 KCl, 2 $MgCl_2$, 0.1 $BaCl_2$, and 5 HEPES (pH 7.5) . For experiments in the presence of calcium, $BaCl_2$ was replaced

with 1.8 mM $CaCl_2$. All recordings were performed at room temperature. Data were subsequently analyzed using pClamp software (Molecular Devices). Internal background currents were subtracted from all recordings unless otherwise indicated. Oocytes were individually collected after recordings, lysed in 50 µL TRPA1 lysis buffer, and subjected to anti-FLAG immunoblot analysis to confirm construct expression as detailed below.

Bacterial Protein Expression, Purification, and Circular Dichroism Spectroscopy

Bacterial expression vectors were transformed into BL21(DE3) cells and plated on Kanamycin (Kan) LB agar plates. Individual colonies were selected to inoculate LB Kan overnight starter cultures from which 10 mL was used to inoculate 1 L of TB Kan. Once the inoculated TB Kan reached an OD of 0.8-1.0, protein expression was induced using 1 mM IPTG. After 4 hours post-induction, bacteria were harvested, snap frozen with liquid nitrogen, and stored in a -80°C freezer. Bacteria were cultured at 37°C with gentle rotation for each step.

Bacterial pellets were thawed at 4°C and resuspended in bacterial lysis buffer (50 mM Tris pH 8.0, 500 mM NaCl, 2 mM $CaCl_2$, 5 mM β-ME, 1 mM PMSF, 10% glycerol, and 5 mg bovine DNase I). Bacteria were lysed on ice using a Fisherbrand Model 120 Sonic Dismembrator (Fisher Scientific). The sonicator was set to 50% amplitude and cycled between 1 minute on and 1 minute off for a total of 20 minutes. Bacterial debris were pelleted using an Eppendorf centrifuge 5810 R cooled to 4°C at 3900 RPM for 30 minutes. All constructs contained an 8x histidine tag and were purified by gravity-flow IMAC using lysis buffer equilibrated HisPur Ni-NTA resin (ThermoFisher). To remove non-specifically bound proteins, the resin was washed with low-molar imidazole wash buffer (50 mM Tris pH 8.0, 150 mM NaCl, 5 mM β-ME, 0.1 mM PMSF, and 20 mM imidazole). Bound protein was eluted in 2 mL fractions with high-molar imidazole elution buffer (50 mM Tris pH 8,0, 150 mM NaCl, 2 mM $CaCl_2$, 5 mM β-ME, 0.1 mM PMSF, and 300 mM imidazole) and an A280 measurement was taken for each fraction using a NanoDrop One (ThermoFisher). Protein

containing fractions were pooled, exchanged into storage buffer (50 mM Tris pH 8.0 150 mM NaCl, 2 mM $CaCl_2$, and 0.1 mM PMSF) and concentrated using Amicon Ultra centrifugal filter with a 10,000 Da molecular weight cutoff (Millipore). MBP-tagged TRPA1 DDC peptide was incubated with TEV protease overnight at 4°C to cleave the MBP tag. After TEV protease digestion, DDC peptide was isolated from MBP using an Amicon Ultra centrifugal filter with a 30,000 Da molecular weight cutoff, followed by size-exclusion chromatography using a Superdex 75 Increase 10/300 GL (Cytiva). SDS-Page and Coomassie staining was used for post-hoc analysis of each step of the purifications.

Prior to CD analysis, I exchanged peptide into CD buffer (10mM Tris, 50mM NaCl). Samples were prepared with 0.1mg/ml of DDC peptide, as determined using NanoDrop One, and loaded into a glass cuvette (Hellma Analytics, 2mm light path). CD data was collected on a Chirascan (Applied Photophyscis) at Yale University's Keck Biophysics Resource Center. Data analysis was performed using Chirascan Pro-Data software and the online BeStSel fold recognition tool (ELTE Eötvös Loránd University, Budapest, Hungary).

Immunofluorescence Imaging

Neuro2A cells transiently transfected with jetPRIME (Polyplus) according to manufacturer protocols were transferred to poly-L-lysine-coated cover slips and incubated for 16-20 hours prior to immunostaining. Cells were fixed on coverslips with 4% paraformaldehyde for 20 minutes, then permeabilized with 0.1% Triton in PBS for 10 min. Cells were then blocked in 4% BSA in PBS. For CaM colocalization experiments, cells were subsequently incubated in primary anti-V5 monoclonal antibody (mouse, 1:500, Invitrogen) in 4% BSA in PBS at room temperature for 45 min. Cells were then washed with PBS and incubated with goat Alexa-Fluor488-conjugated secondary anti-mouse antibody in 4% BSA in PBS at room temperature for 45 min (1:700, Invitrogen), followed by PBS washes. To visualize 3xFLAG TRPA1, cells were incubated in Cy3-conjugated anti-FLAG monoclonal antibody (mouse, 1:500, Sigma) in 4% BSA in PBS at room

temperature for 45 min. For acidic cluster experiments, primary incubation was performed with anti-FLAG monoclonal antibody (1:500, Sigma) , and secondary incubation was performed with goat Alexa-Fluor488-conjugated secondary anti-mouse (1:700, Invitrogen). Images were acquired on a Zeiss Axio Observer Z1 inverted microscope using a Plan-Apochromat 63x/1.40 NA oil objective. Images were collected with ZEN 2.1 software.

CaM Agarose and Surface Biotinylation Pulldown Assays

16-24 hours post-transfection, HEK293T cells were washed with PBS (calcium and magnesium free) and lysed in 75-150 μL of TRPA1 lysis buffer (40 mM Tris pH 8.0, 150 mM NaCl, 5 mM DDM, 500 μM EGTA, EDTA-free cOmplete protease cocktail inhibitor tablet) at 4°C while gently nutating. Cell debris were pelleted from the resulting lysates by centriguation at 15,000 RPM for 10 minutes at 4°C. Total protein concentration in lysates were quantified using a BCA assay (Pierce). Equal concentrations of protein lysate (100 μg) from each experimental condition were added to resins as specified below. 10% of loaded protein amount was reserved as a whole-cell lysate loading control. Buffers were supplemented with free Ca^{2+} as indicated in each figure. Concentrations of $CaCl_2$ required for each free Ca^{2+} concentration were calculated using Ca-EGTA calculator v1.3 using constants from Theo Schoenmakers' Chelator on the MaxChelator website.

CaM-agarose Pulldown: Lysates were incubated with 10 μL of lysis buffer-equilibrated Calmodulin-agarose (Sigma-Aldrich) for 1 hour at 4°C with gentle nutation. Resin beads were washed 3-5 times with lysis buffer prior to elution; resin was pelleted, and bound proteins were eluted in TRPA1 lysis buffer supplemented with 5 mM EGTA for 30 minutes at 4°C with gentle nutation.

Neutravidin Pulldown: Cell lysates that were generated following surface labeling experiments were incubated with 15 μL of lysis buffer equilibrated Neutravidin resin (Pierce) for 2

hours at 4°C with gentle nutation. The resin was then washed with lysis buffer three times, followed by a harsher wash with 1x PBS + 100 mM DTT. Resin was then washed once each with lysis buffer and 1x PBS. Biotinylated protein was eluted from the resin with a multi-step protocol to prevent TRPA1 aggregation while maximizing protein elution from the resin. First, resin was incubated with 10 µL of biotin elution buffer (TRPA1 lysis buffer, 100 mM Glycine, 10 mM Biotin, 1% SDS) on ice for 10 min, followed by addition of 1 µL ß-mercaptoethanol (BME; Sigma) to each sample and incubation on ice for 5 minutes, and finally by addition of 4 µL 4x Laemmli buffer + 10% BME with incubation at 65°C for 10 minutes. The resin was centrifuged, supernatant was removed and combined with additional 4 µL Laemmli buffer + 10% BME for SDS-PAGE analysis.

SDS-PAGE and Immunoblot

Samples were combined with 4x Laemmli Sample buffer supplemented with 10% BME, separated on pre-cast 4-20% SDS-PAGE gels (BioRad), and transferred onto PVDF membranes (BioRad) by semi-dry transfer. Blots were blocked in 3% BSA prior to antibody probing. The following primary antibodies were used in 1x PBST buffer (Boston Bioproducts): MBP (mouse, 1:30,000, New England Biolabs E8032), FLAG (mouse, 1:30,000, Sigma A8592), tubulin (mouse, 1:5,000 in BSA, Sigma T6199), and V5 probe (1:5,000 in BSA, Invitrogen). HRP-conjugated IgG secondary anti-mouse antibody was used as needed (rabbit, 1:25,000, Thermo 61-6520). Membranes were developed using Clarity Western ECL substrate (Bio-Rad) and imaged using a Chemidoc Imaging System (BioRad).

Statistical Analysis

All data quantification was performed in Microsoft Excel. Quantified data presentation and statistical analyses were performed in GraphPad Prism. Data represent mean ± SEM. Each experiment was performed a minimum of three independent times. Comparison between two groups was analyzed by Student's t test, and comparison between multiple groups was analyzed

by one-way ANOVA with Bonferroni or Tukey's *post hoc* analysis, as indicated. Criterion for statistical significance for all tests was $p<0.05$.

3.5 Figures

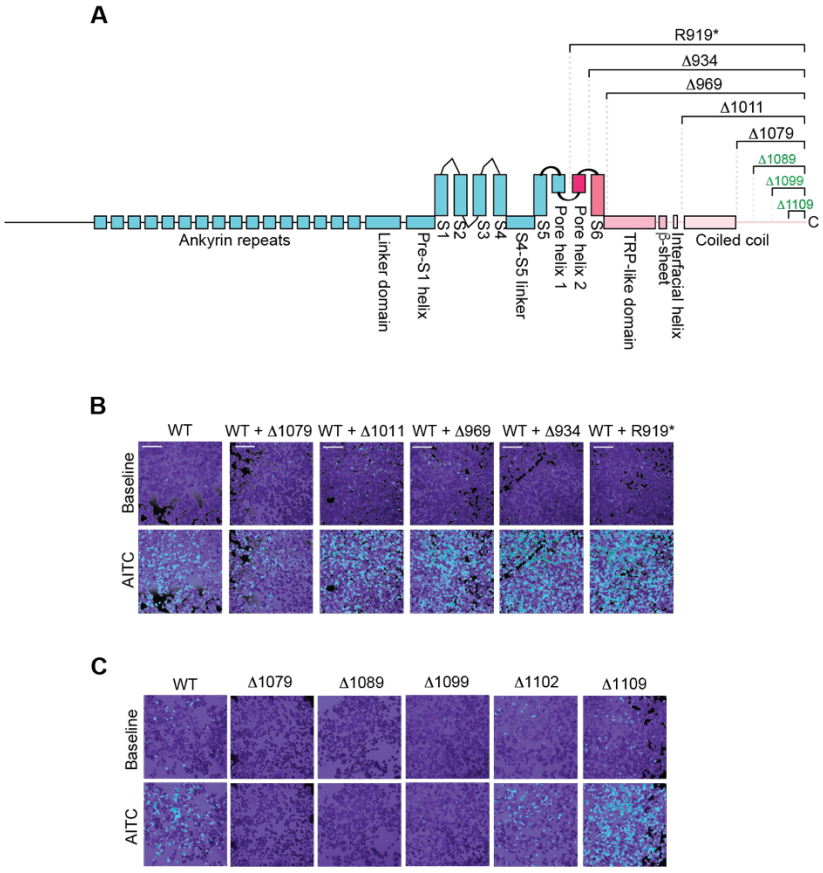

Figure 1. The distal disordered C-terminus (E1079-P1119) is vital for TRPA1 function (**A**) Linear cartoon schematic of a full-length hTRPA1 monomeric subunit with relevant structural features. Regions retained in R919* hTRPA1 are indicated in teal and regions truncated are indicated in pink. Green-labels indicated truncations within the DDC (**B**) Ratiometric calcium imaging of HEK293T cells transiently transfected with the indicated 3xFLAG-tagged hTRPA1 constructs. Cells were stimulated with AITC (100 μM, n=60 cells per transfection condition). (**C**) Ratiometric Ca^{2+} imaging of HEK293T cells singly transfected with 3xFLAG-tagged hTRPA1 constructs. Cells were stimulated with 100 μM AITC (10 or 100 μM). Images are representative of three independent experiments. Scale bars indicate 100 μm. All images representative of three independent experiments.

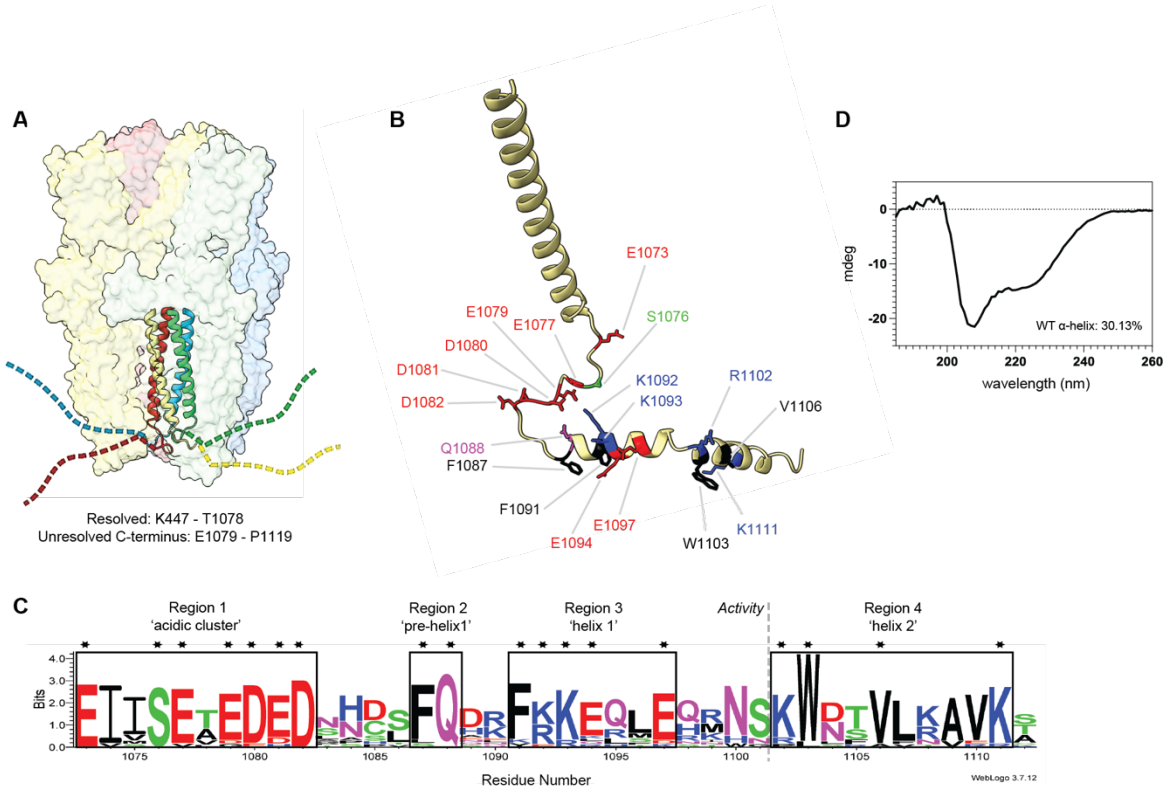

Figure 2. Structure and sequence conservation within the DDC (**A**) Depiction of a WT hTRPA1 atomic model for residues S448-T1078 from the homotetrameric channel (PDB: 6V9X). Each subunit is colored differently for clarity. Ribbons depict C-terminal coiled-coils and dotted lines represent unresolved distal disordered C-terminus. (**B**) Ribbon diagram of the disordered TRPA1 C-terminus (1073-1119) as predicted by AlphaFold2 (**C**) Sequence alignment of 16 TRPA1 orthologues aligned to residues 1073-1112 of hTRPA1, with regions of conservation boxed. Sidechains of starred residues are shown in B. Alignment generated with WebLogo 3.7.12. (**D**) CD spectroscopy of a TRPA1 1079-1119 peptide, showing signature alpha-helical negative peaks near 208 and 222nm and positive peaks near 193nm. Helical content predication obtained from spectral analysis in BeStSel

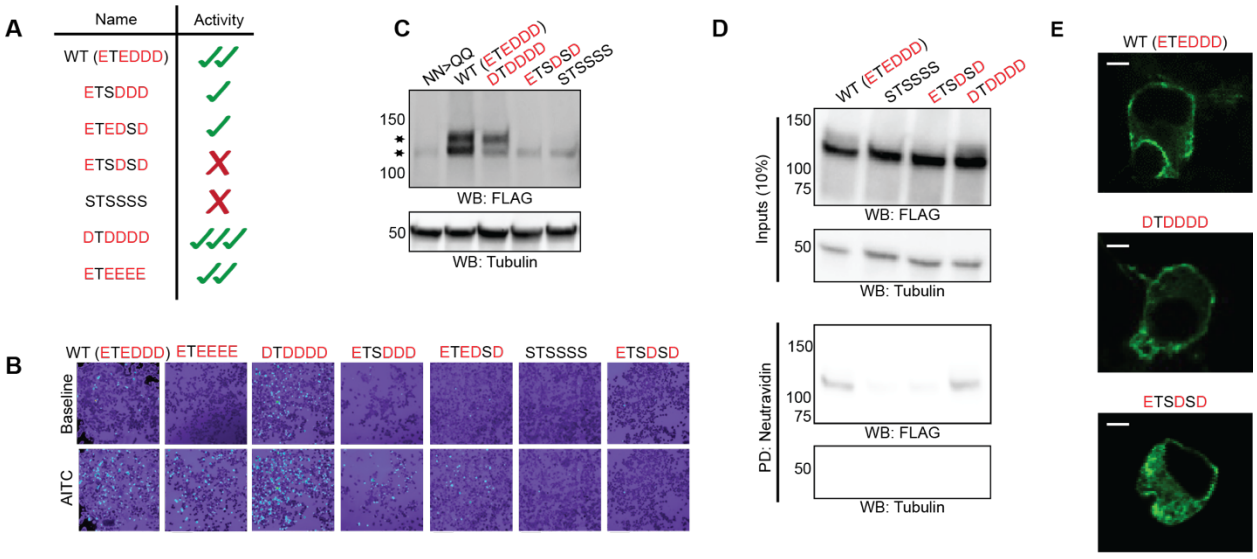

Figure 3. The acidic cluster is vital for TRPA1 activity and trafficking (**A**) Table summarizing acidic cluster variant suite and their activity profiles, as assessed in B. Residues 1077-1082 were considered for variant generation. (**B**) Ratiometric calcium imaging of HEK293T cells transiently transfected with the indicated 3xFLAG-tagged hTRPA1 constructs. Cells were stimulated with AITC (10 μM, n=90 cells per transfection condition). Images are representative of three independent experiments. (**C**) Western blot analysis of HEK293T cell lysates transiently transfected with 3xFLAG-tagged acidic cluster variants and glycosylation-site mutant. Stars indicate mature (upper) and immature (lower) glycosylation bands (**D**) Immunoblotting analysis of 3xFLAG-tagged hTRPA1 constructs in biotin-labeled plasma membranes from transiently transfected HEK293T cells. Biotinylated proteins were precipitated by Neutravidin resin pulldown and probed using HRP-conjugated anti-FLAG antibody. Tubulin from whole cell lysates (10%, inputs) was the loading control. Data is representative of three independent experiments. (**E**) Representative immunofluorescence images of Neuro2A cells transiently co-transfected with 3xFLAG-tagged hTRPA1 variant. Cells were stained with anti-FLAG (green) antibodies. Scale bar indicates 5 μm. Images are representative of three independent experiments.

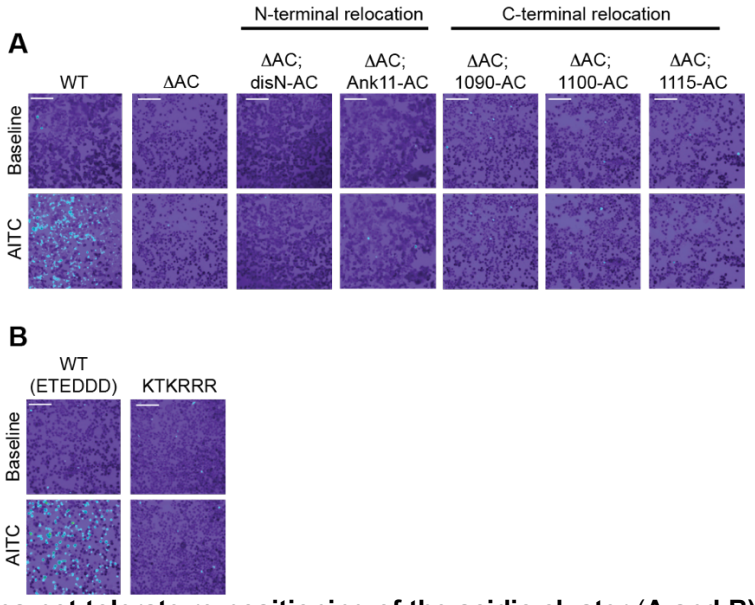

Figure 4. TRPA1 does not tolerate re-positioning of the acidic cluster (**A and B)** Ratiometric calcium imaging of HEK293T cells transiently transfected with the indicated 3xFLAG-tagged hTRPA1 constructs. Residues 1077-1082 were deleted to generate ΔAC. Cells were stimulated with AITC (100 μM, n=90 cells per transfection condition).

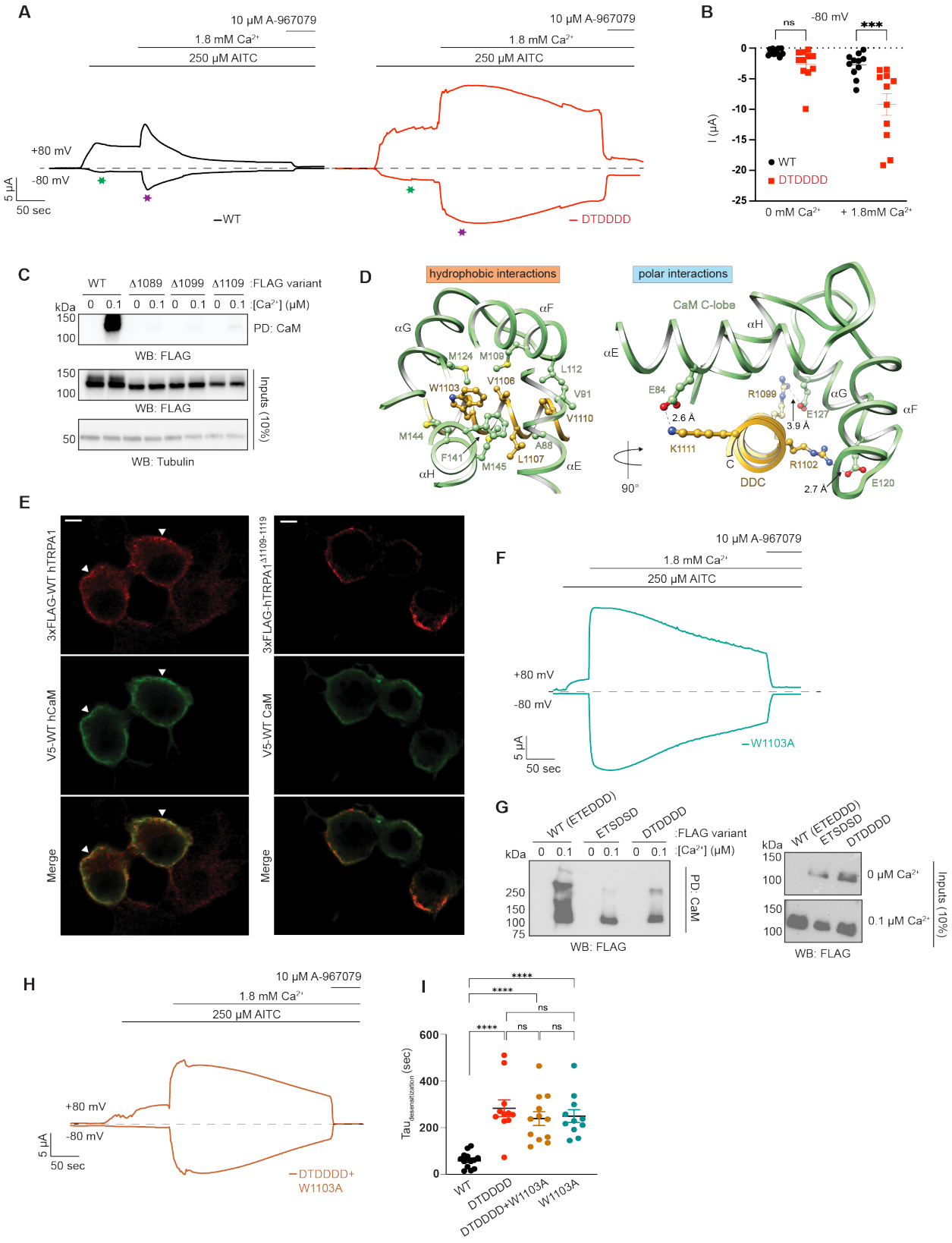
A
10 μM A-967079
1.8 mM Ca2+
250 μM AITC
+80 mV
-80 mV
5 μA
50 sec
WT
DTDDDD
B
ns
-80 mV
***
I (μA)
WT
DTDDDD
0 mM Ca2+
+ 1.8mM Ca2+
C
WT
Δ1089
Δ1099
Δ1109
:FLAG variant
kDa
:[Ca2+] (μM)
PD: CaM
WB: FLAG
Inputs (10%)
WB: Tubulin
D
hydrophobic interactions
polar interactions
CaM C-lobe
αF
αG
αH
αE
M124
M109
L112
W1103
V1106
V91
V1110
M144
F141
M145
L1107
A88
E84
R1099
E127
2.6 Å
3.9 Å
K1111
C
DDC
R1102
2.7 Å
E120
90°
E
3xFLAG-WT hTRPA1
V5-WT hCaM
Merge
3xFLAG-hTRPA1Δ1109-1119
V5-WT CaM
F
10 μM A-967079
1.8 mM Ca2+
250 μM AITC
+80 mV
-80 mV
5 μA
50 sec
W1103A
G
WT (ETEDDD)
ETSDSD
DTDDDD
:FLAG variant
kDa
:[Ca2+] (μM)
PD: CaM
WB: FLAG
0 μM Ca2+
0.1 μM Ca2+
Inputs (10%)
H
10 μM A-967079
1.8 mM Ca2+
250 μM AITC
+80 mV
-80 mV
5 μA
50 sec
DTDDDD+
W1103A
I
****
ns
Tau desensitization (sec)
WT
DTDDDD
DTDDDD+W1103A
W1103A

Figure 5. The DDC regulates calcium-mediated desensitization via the acidic cluster and a novel CaM binding site (**A**) Representative TEVC time-traces at -80 and +80 mV holding potentials from oocytes expressing WT (black) or hyper-acidic DTDDDD (red). Current evoked with 250 μM AITC in the absence and presence of 1.8 mM extracellular Ca^{2+}. Channels were blocked with 10 μM A-967079. Dashed line denotes 0 μA current. Protocol of condition application indicated above trace. (**B**) Quantification of peak current amplitudes at -80 mV before (green star in A), and after (purple star in A), Ca^{2+} addition. Data represent mean ± SEM. ***p=0.0002, n.s. not significant (p>0.05). (**C**) Immunoblotting analysis of the indicated 3xFLAG-hTRPA1 constructs after CaM-agarose pulldown at the indicated Ca^{2+} concentrations from lysates of HEK293T cells transfected with 3xFLAG-WT, D1089-1119, D1099-1119, or D1109-1119 hTRPA1. Samples were probed using an HRP-conjugated anti-FLAG antibody. Tubulin from whole cell lysates (10%, inputs) was the loading control. (**D**) Ribbon diagram of the hCaM C-lobe atomic model (green, residues 79-148) in complex with part of the TRPA1 DDC (yellow, residues R1102-K1111) as predicted by AlphaFold2 Multimer. Residues mediating polar (right) and hydrophobic (left) interactions depicted as balls and sticks. (**E**) Representative immunofluorescence images of Neuro2A cells transiently co-transfected with 3xFLAG-WT hTRPA1 and V5-WT hCaM. Cells were stained with anti-FLAG (red) and anti-V5 (green) antibodies. Regions of co-localization appear as yellow in the merged images. White arrowheads denote cells exhibiting co-localization. Scale bar indicates 5 μm. Images are representative of three independent experiments. (**F**) Representative TEVC time-trace at -80 and +80 mV holding potentials from oocytes expressing W1103A hTRPA1 variant. See A for condition application protocol. (**G**) Immunoblotting analysis of the indicated 3xFLAG-hTRPA1 constructs after CaM-agarose pulldown at the indicated Ca^{2+} concentrations from lysates of HEK293T cells transfected with 3xFLAG-WT, ETSDSD, or DTDDDD hTRPA1. Immunoblot was probed using an HRP-conjugated anti-FLAG antibody. (**H**) Representative TEVC time-trace at -80 and +80 mV holding potentials from oocytes expressing double-mutant DTDDDD+ W1103A hTRPA1. See A for condition application protocol. (**I**) Calculated time constants of desensitization from fitting data as in A, F, and H to a single-exponential decay function. Data represent mean ± SEM. ****p<0.0001, n.s. not significant (p>0.05).
(**Data contributions: Panel C:** J Sanders/C Paulsen**, Panel D:** Y Zhang, **Panel F:** J Sanders, **Panel G:** KM Taiwo)

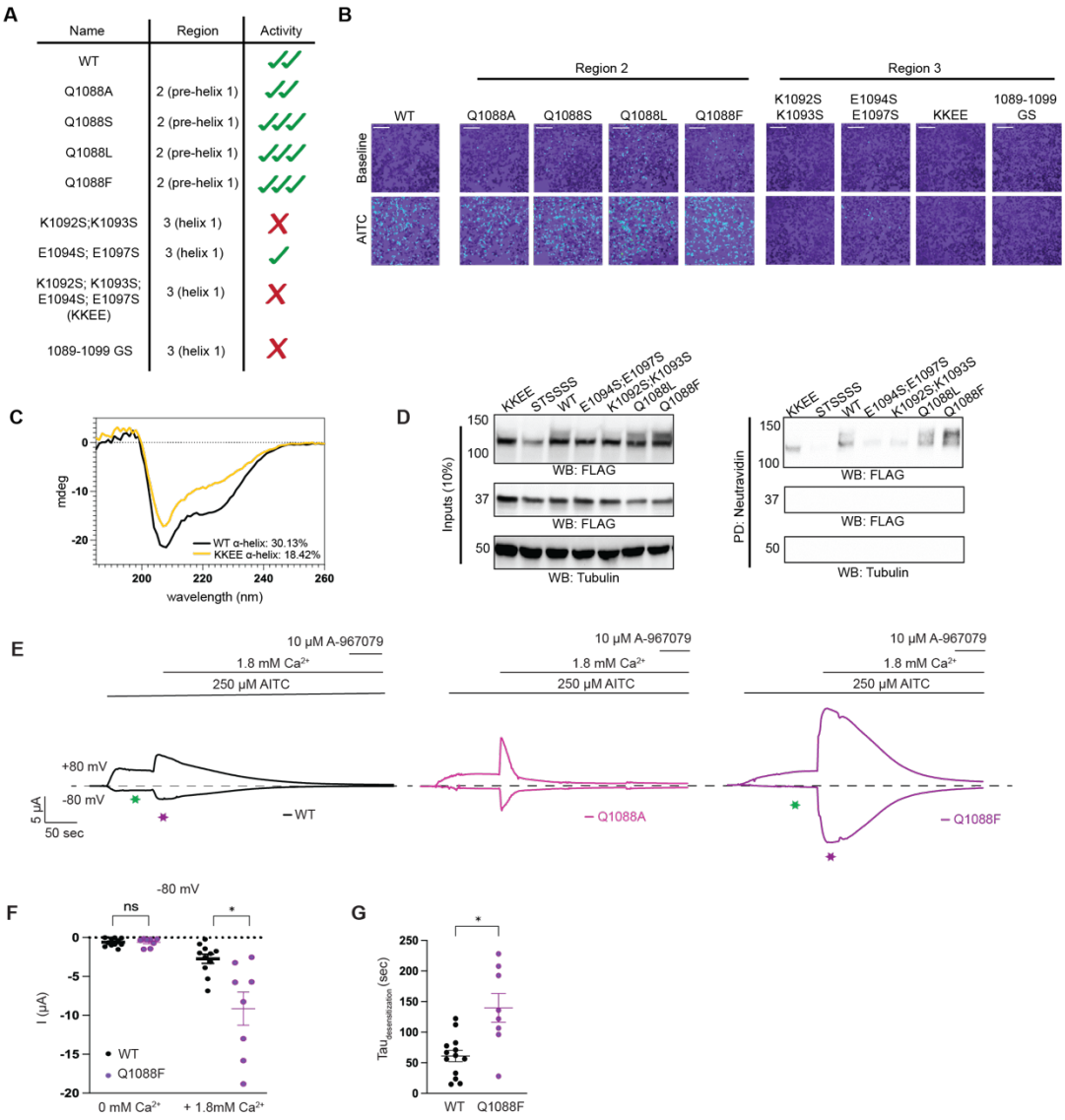

Figure 6. Regions 2 and 3 of the DDC are important for channel function (**A**) Table summarizing hTRPA1 variants and their activity profiles, as assessed in B. Regions 2 and 3 defined as in Figure 2. (**B**) Ratiometric calcium imaging of HEK293T cells transiently transfected with 3xFLAG-tagged hTRPA1 carrying mutations in Region 2 (top) and Region 3 (bottom). Cells were stimulated with AITC (100 μM, n=90 cells per transfection condition). Images are representative of three independent experiments. Scale bars indicate 100 μm (**C**) CD spectroscopy of a TRPA1 1079-1119 peptide containing the WT sequence (black) or mutations K1092S; K1093S; E1094S; E1097S (yellow). Helical content predications obtained from spectral analysis in BeStSel (**D**) Immunoblotting analysis of 3xFLAG-tagged hTRPA1 constructs or FLAG-Torsin A protein expression in biotin-labeled plasma membranes from transiently transfected HEK293T cells. Biotinylated proteins were precipitated by Neutravidin resin pulldown and probed using HRP-conjugated anti-FLAG antibody. Tubulin from whole cell lysates (10%, inputs) was the loading control. Torsin A was the negative control for plasma membrane localization. (**E**) Representative TEVC time-traces at -80 and +80 mV holding potentials from oocytes expressing WT (black), Q1088A (pink), or Q1088F (purple). Current evoked with 250 μM AITC in the absence and presence of 1.8 mM extracellular Ca^{2+}. Channels were blocked with 10 μM A-967079. Dashed line denotes 0 μA current. Protocol of condition application indicated above trace. (**F**) Quantification of peak current amplitudes at -80 mV before (green star in D), and after (purple star in D) Ca^{2+} addition. Data represent mean ± SEM. *p<0.05, n.s. not significant (p>0.05). (**G**) Calculated time constants of desensitization from fitting data from

oocytes expressing WT and Q1088F to a single-exponential decay function. Data represent mean ± SEM. *p<0.05. Welch's t-test

3.6 References

1. Talavera, K. et al. Mammalian Transient Receptor Potential TRPA1 Channels: From Structure to Disease. *Physiol Rev* **100**, 725-803 (2020).
2. Chen, J. & Hackos, D.H. TRPA1 as a drug target--promise and challenges. *Naunyn Schmiedebergs Arch Pharmacol* **388**, 451-63 (2015).
3. Grace, M.S., Baxter, M., Dubuis, E., Birrell, M.A. & Belvisi, M.G. Transient receptor potential (TRP) channels in the airway: role in airway disease. *Br J Pharmacol* **171**, 2593-607 (2014).
4. Hinman, A., Chuang, H.H., Bautista, D.M. & Julius, D. TRP channel activation by reversible covalent modification. *Proc Natl Acad Sci U S A* **103**, 19564-8 (2006).
5. Liu, C. et al. A Non-covalent Ligand Reveals Biased Agonism of the TRPA1 Ion Channel. *Neuron* **109**, 273-284 e4 (2021).
6. Zhao, J., Lin King, J.V., Paulsen, C.E., Cheng, Y. & Julius, D. Irritant-evoked activation and calcium modulation of the TRPA1 receptor. *Nature* **585**, 141-145 (2020).
7. Suo, Y. et al. Structural Insights into Electrophile Irritant Sensing by the Human TRPA1 Channel. *Neuron* **105**, 882-894 e5 (2020).
8. Wang, Y.Y., Chang, R.B., Waters, H.N., McKemy, D.D. & Liman, E.R. The nociceptor ion channel TRPA1 is potentiated and inactivated by permeating calcium ions. *J Biol Chem* **283**, 32691-703 (2008).
9. Matsuda, M., Huh, Y. & Ji, R.R. Roles of inflammation, neurogenic inflammation, and neuroinflammation in pain. *J Anesth* **33**, 131-139 (2019).
10. Ji, R.R., Nackley, A., Huh, Y., Terrando, N. & Maixner, W. Neuroinflammation and Central Sensitization in Chronic and Widespread Pain. *Anesthesiology* **129**, 343-366 (2018).
11. Zurborg, S., Yurgionas, B., Jira, J.A., Caspani, O. & Heppenstall, P.A. Direct activation of the ion channel TRPA1 by Ca2+. *Nat Neurosci* **10**, 277-9 (2007).
12. Hasan, R., Leeson-Payne, A.T., Jaggar, J.H. & Zhang, X. Calmodulin is responsible for Ca(2+)-dependent regulation of TRPA1 Channels. *Sci Rep* **7**, 45098 (2017).
13. Sura, L. et al. C-terminal acidic cluster is involved in Ca2+-induced regulation of human transient receptor potential ankyrin 1 channel. *J Biol Chem* **287**, 18067-77 (2012).
14. Shepherd, J.D. & Huganir, R.L. The cell biology of synaptic plasticity: AMPA receptor trafficking. *Annu Rev Cell Dev Biol* **23**, 613-43 (2007).
15. Higerd-Rusli, G.P. et al. The fates of internalized Na(V)1.7 channels in sensory neurons: Retrograde cotransport with other ion channels, axon-specific recycling, and degradation. *J Biol Chem* **299**, 102816 (2023).
16. Tian, Q. et al. Recovery from tachyphylaxis of TRPV1 coincides with recycling to the surface membrane. *Proc Natl Acad Sci U S A* **116**, 5170-5175 (2019).
17. Zhang, X., Huang, J. & McNaughton, P.A. NGF rapidly increases membrane expression of TRPV1 heat-gated ion channels. *EMBO J* **24**, 4211-23 (2005).
18. Cheng, J.K. & Ji, R.R. Intracellular signaling in primary sensory neurons and persistent pain. *Neurochem Res* **33**, 1970-8 (2008).
19. Schmidt, M., Dubin, A.E., Petrus, M.J., Earley, T.J. & Patapoutian, A. Nociceptive signals induce trafficking of TRPA1 to the plasma membrane. *Neuron* **64**, 498-509 (2009).
20. Khan, S. et al. IQGAP1 promotes chronic pain by regulating the trafficking and sensitization of TRPA1 channels. *Brain* **146**, 2595-2611 (2023).
21. Paulsen, C.E., Armache, J.P., Gao, Y., Cheng, Y. & Julius, D. Structure of the TRPA1 ion channel suggests regulatory mechanisms. *Nature* **520**, 511-7 (2015).
22. Carey, F. & Giuliano, R. Amino acids, peptides and proteins. in *Organic Chemistry* 8 edn Vol. 25 1126 (McGraw Hill, 2011).
23. Egan, T.J., Acuna, M.A., Zenobi-Wong, M., Zeilhofer, H.U. & Urech, D. Effects of N-Glycosylation of the human cation channel TRPA1 on agonist-sensitivity. *Biosci Rep* **36**(2016).
24. Mikosch, M., Hurst, A.C., Hertel, B. & Homann, U. Diacidic motif is required for efficient transport of the K+ channel KAT1 to the plasma membrane. *Plant Physiol* **142**, 923-30 (2006).
25. Kottgen, M. et al. Trafficking of TRPP2 by PACS proteins represents a novel mechanism of ion channel regulation. *EMBO J* **24**, 705-16 (2005).

26. Singh, R. et al. Phosphoserine acidic cluster motifs bind distinct basic regions on the mu subunits of clathrin adaptor protein complexes. *J Biol Chem* **293**, 15678-15690 (2018).
27. Chaumont, S., Jiang, L.H., Penna, A., North, R.A. & Rassendren, F. Identification of a trafficking motif involved in the stabilization and polarization of P2X receptors. *J Biol Chem* **279**, 29628-38 (2004).
28. Beers, M.F. et al. A novel conserved targeting motif found in ABCA transporters mediates trafficking to early post-Golgi compartments. *J Lipid Res* **52**, 1471-82 (2011).
29. Crump, C.M. et al. PACS-1 binding to adaptors is required for acidic cluster motif-mediated protein traffic. *EMBO J* **20**, 2191-201 (2001).
30. Newcombe, E.A. et al. Insight into Calcium-Binding Motifs of Intrinsically Disordered Proteins. *Biomolecules* **11**(2021).

Chapter 4: Outlooks and Future Directions

In this chapter, I summarize and contextualize findings from my doctoral work and address unanswered questions that compel further exploration. Here I propose potential strategies for future projects in our research group and present some additional preliminary data I have collected in support of these new endeavors.

4.1 Future Directions

i. Towards understanding TRPA1 function and physiology via channelopathies

My work as presented in Chapter 2 was largely aimed at uncovering how a drastic CRAMPT-associated nonsense mutation R919* could facilitate gain-of-function phenotypes in patients. Remarkably, we found that the R919* mutant conferred gain-of-function when co-expressed with WT TRPA1 subunits (See Chapter 2; Figures 2, 3 and 10). Our data collectively suggests that WT and R919* TRPA1 subunits co-assemble to form hyperactive heteromeric ion channels characterized by enhanced sensitivity to multiple agonist types and by altered pore architecture and increased inward calcium permeation (see Chapter 2; Figure 10).

While my work has revealed a novel and interesting mechanism of TRPA1 gain-of-function, there remain multiple open questions which merit further investigation. First and foremost, how exactly do WT-R919* heteromeric channels assemble, and what is the structural basis of their hyperactivity? Based on our tandem pulldown assays, R919* and WT subunits can seemingly co-assemble into channels with multiple stoichiometries (**Figure 1A**, See Chapter 2; Figure 5E-F). Which of these stoichiometries are most prevalent and relevant to the CRAMPT disease phenotype has yet to be elucidated. In my functional assessments of the R919* TRPA1 mutant, WT homotetrameric channels would have been produced alongside WT-R919* heteromeric channels. This heterogeneity technically complicates characterizing WT-R919* TRPA1 heteromers using single-channel methods from patches pulled from cell membranes.

Thus, future work will require establishing a homogenous population of WT-R919* TRPA1 complexes with defined subunit stoichiometry that can be studied in isolation.

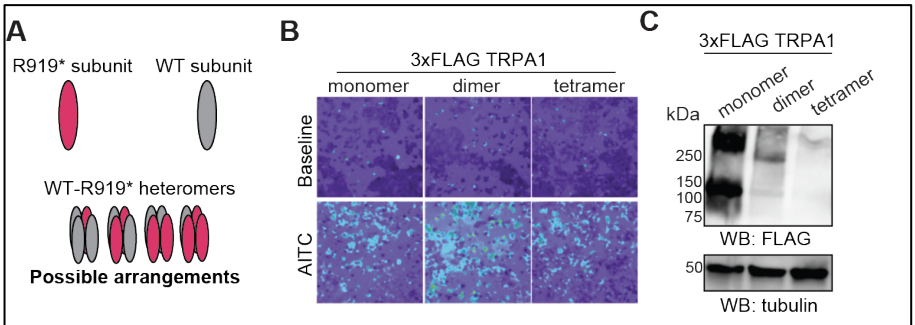

Figure 1: Proof of concept for utilizing concatemers to determine heteromer stoichiometry. A) WT and R919* hTRPA1 subunits may co-assemble into hyperactive heterotetrameric channels of four possible subunit stoichiometries and arrangements. **B-C)** Ratiometric calcium imaging (B) and immunoblot analysis (C) of HEK293T cells transiently transfected with 3x-FLAG tagged TRPA1 as a single gene copy (monomer) or as a concatemer with two (dimer) or four (tetramer) tandem-linked genes. Channels were activated with AITC (100 μM). Images are representatives from four independent experiments.

A potential strategy for investigating subunit stoichiometry within heteromeric channels is the use of TRPA1 concatemers in which multiple gene copies are linked in tandem[1]. Concatemers allow expression of channels with defined subunit composition and would therefore facilitate precise functional measurements of specific stoichiometric arrangements of WT and R919* subunits. Indeed, I have been able to pilot expression of a codon-optimized concatemeric WT TRPA1 tetramer and dimer in HEK293T cells, and have demonstrated that these concatemers are able to form functional channels (**Figure 1B-C**). Future studies will involve modification of concatemeric dimers and tetramers to include R919* in order to functionally isolate specific WT-R919* heteromer stoichiometries. If successful, WT-R919* concatemers will eventually allow us to perform single-channel patch clamp to characterize WT-R919* heteromer channel properties.

Homogeneous concatemers of specific WT-R919* stoichiometries will also facilitate structural determination of heteromeric channels that could directly reveal how R919* subunits alter channel architecture to promote sensitization. My work demonstrates that WT-R919* heteromeric channels can be purified in small-batch preparations (See Chapter 2; Figure 5). However, tandem-purification of heteromeric channels results in very low protein yield that is detectable by Western blot (as shown in Chapter 2), but not always by Coomassie stain (not

shown). To obtain high-resolution cryo-EM structures, large-scale purification of WT-R919* heteromers with sufficiently high yield will be necessary. Generation of TRPA1 baculoviruses for large-scale expression in High Five insect cells is currently underway in our lab; however, structural work targeting TRP heteromeric channels can involve a multitude of technical hurdles[2,3]. Exceedingly large amounts of cell cultures may be needed to generate enough protein for cryo-EM analysis [2], after which stoichiometric heterogeneity can complicate 2D classification and 3D modeling. In this regard, WT-R919* concatemers with fixed subunit ratios will be eminently useful.

While TRPA1 cryo-EM structures have been solved before[4-6], the related TRPV1 channel is smaller in size and much more biochemically stable [7,8]. A fortuitous discovery I made during my studies on R919* TRPA1 was that an analogous nonsense mutation (F656*) in TRPV1 also confers hyperactivation to its WT counterpart, suggesting the structural mechanism of TRPA1 hyperactivation in CRAMPT is evolutionarily conserved (see Chapter 2; Figure 9 and Supplementary Figure 12). Unlike TRPA1, TRPV1 retains channel function after purification and reconstitution into lipid bilayers, thus allowing patch clamp analysis on purified WT/F656* heteromers. TRPV1 can therefore be a valuable proxy for TRPA1 in our structural and functional studies, which may alleviate some challenges in protein purification and boosting protein yields.

Our findings in Chapter 2 contribute to a growing body of evidence that aberrant TRPA1 function can have drastic impacts on human physiology. Two TRPA1 channelopathies – FEPS and CRAMPT – arise from mutations that lead to channel gain-of-function through very distinct mechanisms. The FEPS-associated N855S missense mutation lies on the S4-S5 linker of TRPA1 and increases inward current by 5-fold while exhibiting no changes to agonist sensitivity [9] (See Chapter 2 Figure 1 and 2). However, exactly how the N855S mutation influences channel gating is not well understood. Existing structures and *in silico* modeling suggest residues neighboring N855 form inter-subunit salt bridges between adjacent S4-S5 regions during activation [10] (See Chapter 1; Figure 6) . The authors propose that the FEPS mutation changes these inter-subunit interactions to stabilize open channels, however their MD simulations did not reveal significant

structural changes to the S4-S5 linker upon mutation of N855 to S, R, or V. Future biophysical studies of N855S are therefore warranted. Directly solving a high-resolution structure of the N855S TRPA1 mutant in an agonist-bound active state would answer questions about how the mutation may change the conformation of S4-S5 linker and its potential interactions. In parallel to structure work, single-channel patch clamp recordings on N855S TRPA1 would reveal its open/closed probability and directly test whether the open state is stabilized, or whether an increase in the unitary conductance of the channel is instead responsible for channel hyperactivation. These studies could be conducted alongside point mutations of other conserved S4/S5 residues (ie: E854 and K868) to test whether putative inter-subunit salt bridges play a role in open state stability. Collectively, this work would definitively determine the mechanism of hyperactivation in FEPS, and would also clarify the role played by the S4-S5 linker in TRPA1 gating.

CRAMPT Symptoms	CBZ Response
Muscle cramps, fasciculations and stiffness	+++ / +++
Cold-triggered hyperalgesia and parasthesias; chronic pruritis; restless leg syndrome	+++ / ++
Cardiac palpitations and paroxysmal resting tachycardia, short QT	++ / ++
Respiratory tract sensitivity, asthama, chronic cough	+++ / ++
GI acid reflux, irritable bowel syndrome , gastritis, and dysphagia to liquids	-- / ++

Nirenberg et al, *Clin Genet*, 2017

Table 1: Summary of symptoms experienced by CRAMPT patients grouped by the affected tissues. (Adapted from Nirenberg et al 2017). Right column ranks effectiveness of carbamazepine in treating symptoms. Improvements in symptom relief are indicated as mild (+), moderate (++), and marked (+++); (--) signifies moderate worsening of symptoms

On a physiological level, we have yet to determine how TRPA1 gain-of-function causes certain symptoms in patients - especially outside the pain pathway. In nociceptive sensory neurons, it is plausible that TRPA1 hyperactivation leads to pain phenotypes. Increased TRPA1-mediated Ca^{2+} influx would readily generate action potentials in nociceptor neurons and cause increased pain signaling. This is supported by the fact that treatment with the voltage-gated channel blocker carbamazepine can fully or partially relieve CRAMPT patients of pain and other symptoms[11] (**Table 1**), indicating that TRPA1 may contribute to disease phenotypes by

depolarizing cells. While our model allows us to speculate about how TRPA1 hyperactivation and enhanced Ca^{2+} influx can underlie disease symptoms (see Chapter 2 Discussion), the exact effects of TRPA1 gain-of-function in cardiac, gastrointestinal, respiratory, vascular, and muscular tissues have not been tested directly. In this regard, animal models may prove to be the best route forward for physiological studies. Introduction of FEPS and CRAMPT mutations into mouse models, coupled with rigorous histological, electrophysiological, and behavioral studies could prove immensely powerful for expanding our proposed molecular mechanism of TRPA1 hyperactivity to systems-level mechanisms of disease pathogenesis.

Finally, besides the channelopathic FEPS and CRAMPT mutations that directly underlie human disease, there are a number of TRPA1 single-nucleotide polymorphisms of unknown clinical significance that have been correlated or loosely associated with particular sensory features such as paradoxical heat sensation[12], pain perception in sickle cell disease[13], chemosensory preferences[14,15], and childhood asthma [16]. Recently, a host of novel TRPA1 rare variants were identified from a large cohort of neuropathic pain patients using next-generation sequencing and gene-wise aggregation analysis [17]. Many of these identified SNPs have not been studied at the molecular level with electrophysiology or biochemical methods. Identification and functional characterization of new genetic variants of TRPA1 would further enrich our understanding of structure-function properties, and how they relate to certain aspects of human disease and physiology.

ii. Elucidating specific regulatory mechanisms within the TRPA1 C-terminus

In Chapter 3, I describe foundational work I and other lab colleagues have performed revealing novel regulatory sites within the unresolved distal disordered C-terminus (DDC) of TRPA1. The majority of DDC residues are required for channel activity (see Chapter 3; Figure 1). In particular, I have demonstrated a crucial functional role of a highly conserved acidic cluster at the base of the structured coiled-coil (see Chapter 3; Figure 2). This acidic cluster is seemingly integral to TRPA1 activity as well as trafficking, as evidenced by loss of both channel activity and

trafficking when even partial charge-neutralizing mutations are made to the acidic cluster motif (see Chapter 3; Figure 3). Alongside my findings regarding the DDC acidic cluster, my fellow labmates have identified a novel calmodulin binding site (CaMBS) at the second putative helix within the DDC and were able to show loss of CaM binding by introducing point mutations at the CaMBS (see Chapter 3; Figure 2 and 5). Interestingly, we find that full replacement of acidic cluster residues with aspartic acid (DTDDDD) functionally mimics loss of CaM binding in TRPA1, as both exhibit prolonged Ca^{2+}-mediated desensitization (see Chapter 3; Fig 5). This finding lends support to a compelling hypothesis that perhaps a Ca^{2+} binding site exists at or near the acidic cluster which regulates channel desensitization. We additionally posit that CaM binding allosterically modulates this Ca^{2+} binding site to regulate channel activity.

Collectively, our work on the TRPA1 DDC has begun to tease apart important mechanisms of TRPA1 gating, Ca^{2+} regulation, and trafficking behaviors. However, exact details of how these distal residues can globally impact channel function are still lacking and will require rigorous future study. Naturally, resolving the conformational and dynamic states of the DDC within the context of the whole channel would be most desirable for answering open questions about channel regulation at the DDC, and could directly confirm the existence and structural influence of predicted Ca^{2+} binding sites. However, obtaining such a structure is not straightforward. The mobile and disordered nature of the DDC prevents high-resolution cryo-EM studies, and all existing TRPA1 structures are unable to resolve the DDC beyond T1078 [4-6]. While the DDC could potentially be artificially cross-linked to structured parts of the channel to facilitate resolution, important information about the dynamics and movement of the DDC would be lost.

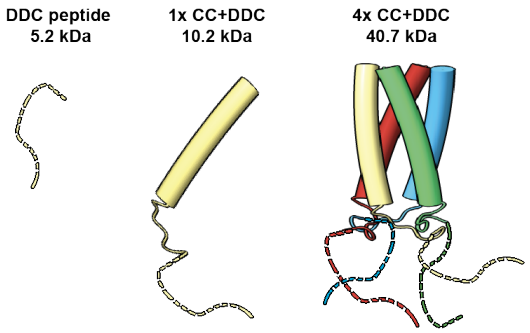

Figure 2: Cartoon depictions of C-terminal fragment constructs developed for future structural studies. DDC indicated by dashed line and strucutred coiled-coils depicted as tube helices i) DDC peptide containing only unresolved residues E1077-end ii) DDC peptide with preceding strucutred coiled-coil iii) Tetrameric assembly of CC+DDC constructs, designed with either TRPA1 or GCN4 coiled-coils

Thus, ongoing work in our lab is aimed at utilizing alternative biophysical strategies to elucidate structure and dynamics using C-terminal peptides and fragments **(Figure 2)**. I have been able to generate and purify small 5.2 kDa DDC fragments **(Figure 2)** for initial characterization of secondary structure with circular dichroism (See Chapter 3; Figure 2D and 6C). Notably, preliminary CD experiments I have performed with the DDC peptide do not exhibit major binding-associated changes to secondary structure or alpha-helical character in the presence of basal or high Ca^{2+} levels (**Figure 3A**). Moreover, DDC peptide containing channel-inactivating acidic cluster mutations at our hypothesized Ca^{2+} binding site also do not exhibit secondary structure change compared to the WT DDC (**Figure 3A**). This could mean that Ca^{2+} binding occurs without inducing helix formation, contrary to prior *in silico* predictions[18], but still entirely possible within a

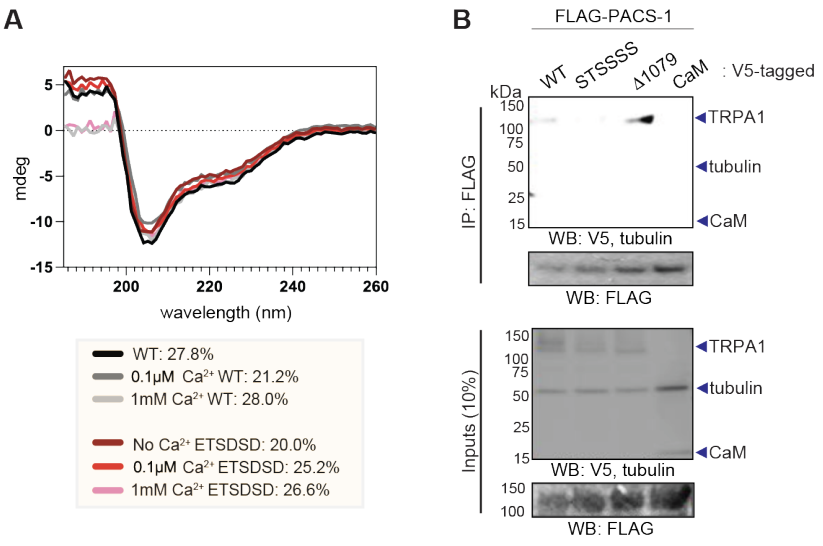

Figure 3: Probing hypothesized interactions at the C-terminal acidic cluster. A) CD spectroscopy of TRPA1 DDC peptide containing the WT sequence (black/grey/light grey) or ETSDSD (maroon/red/pink) under specified calcium conditions. Helical content predications obtained from spectral analysis in BeStSel. **B)** Immunoblotting analysis of the indicated V5-tagged constructs after FLAG immunoprecipitation from lysates of HEK293T cells co-transfected with FLAG-PACS-1.Tubulin from whole cell lysates (10%, inputs) was the loading control. V5-CaM was used as a negative control for PACS-1 binding

disordered domain [19]. An alternative explanation is that Ca^{2+} binding may involve coordination from multiple DDCs, and thus requires tetrameric geometry. To address this possibility, we have designed and are currently optimizing a C-terminal construct containing all 4 tetrameric coiled-coils and their respective DDC domains to mimic the tethering and tetrameric geometry experienced by the TRPA1 DDC in its native context (**Figure 2**). This construct, termed 4x CC+DDC, will be a valuable tool for structural determination methods such as X-ray crystallography and nuclear magnetic resonance to provide a more accurate picture of DDC dynamics and conformational changes upon Ca^{2+} binding. We may also be able to utilize 4x CC+DDC to obtain a CaM-bound structure and illuminate how CaM binding modulates DDC structure and dynamics. Short of rigorous structure work, Ca^{2+} binding of this construct could be tested with isothermal calorimetry, or even a simple absorbance-based O-Cresolphthalein binding assay. Together, this proposed work will hopefully elucidate details of the interplay we observe between the acidic cluster and the CaM binding site and uncover long-sought mechanisms of Ca^{2+}-mediated desensitization of TRPA1.

The 4x CC+DDC construct may also serve as a valuable tool in determining how certain DDC variants exhibit reduced plasma membrane localization and altered processing. My work has demonstrated that removal or mutagenesis of the acidic cluster or putative helix 1 within the DDC results in reduced plasma membrane localization and complex glycosylation of TRPA1 (See Chapter 3; Figures 3 and 6). We posit that these observed defects in trafficking could occur either due to misfolding and ER-retention of the channel or loss of key signaling motifs for recruiting trafficking machinery. Structural probing of 4x CC+DDC constructs carrying neutralizing mutations in the acidic cluster and/or transient helix 1 would help dissect which of these mechanisms is responsible for trafficking defects. If we do not observe clear evidence of misfolding in our variants, our existing DDC peptide and 4x CC+DDC construct could then serve as bait for proteomic studies aimed at discovering novel protein-protein interactions that may be involved in channel processing and trafficking. To preliminarily assess the ability of the acidic cluster to serve

as a sorting signal, I have performed pilot co-immunoprecipitation assays with the trafficking adaptor PACS-1. Literature suggests PACS-1 is a strong candidate for binding TRPA1 based on its consensus-sequence (See Chapter 3; Discussion). Encouragingly, these co-IP data indicate that TRPA1 is capable of binding PACS-1, and that neutralization of the acidic cluster ablates this interaction (**Figure 3B**). However, pulldowns also show that removal of resides after E1079 does not negatively impact PACS-1 binding. Perhaps contributions of acidic residues from multiple DDCs within the tetrameric arrangement may facilitate PACS-1 binding; but nonetheless this puzzling result necessitates more rigorous testing of PACS-1 binding with better positive and negative controls, as well as clear functional and IF assays to support a role of PACS-1 in TRPA1 regulation. Given that the DDC is known to bind CaM, we suspect that other binding partners such as PACS proteins or other regulators can bind within the DDC as well. Future work identifying these novel interactions will shed light on poorly understood mechanisms of TRPA1 trafficking, intracellular sorting, and modulation by protein partners

Broadly speaking, the functional profile of TRPA1 within sensory neurons is the product of multiple complex and dynamic modes of regulation working in harmony. Cells must be able to produce nociceptive channels at the cell surface that can effectively detect noxious stimuli for protective benefit without overtly triggering extraneous Ca^{2+} signaling pathways. In this regard, Ca^{2+}-mediated desensitization offers a means to tightly control Ca^{2+} influx via TRPA1. Over time, however, cells must also be able to maintain nociceptive sensitivity in the face of repeated exposure to noxious environments. One way this can be achieved is by dynamically regulating receptor trafficking and turnover at the plasma membrane in response to channel activation. However, TRPA1 trafficking behavior in sensory neurons – including anterograde trafficking to the plasma membrane as well as subsequent internalization and recycling – is a long-standing enigma. It is also unclear how intrinsic regulatory processes like Ca^{2+}-mediated potentiation and desensitization fit into population-level regulation via trafficking and turnover.

Previous studies have shown that TRPA1 activation with chemical agonists causes recruitment of more TRPA1 channels to the plasma membrane [20]. Strikingly, this activation-induced translocation of TRPA1 to the membrane requires Ca^{2+} influx through the channel, highlighting an interplay between transient changes to cytoplasmic Ca^{2+} and channel trafficking. An intriguing possibility is that the acidic cluster at the DDC serves as an integration site where changes in Ca^{2+} concentration can be sensed and coupled to channel trafficking. Indeed, such a mechanism has been proposed for the related TRPP2 (PKD2) channel, which also permeates and is regulated by Ca^{2+}. TRPP2 possesses a bona fide PACS-1 acidic cluster binding site, complete with a casein kinase phosphorylation residue S812 [21]. When this residue is mutated and phosphorylation is lost, the channel becomes less sensitive to Ca^{2+}potentiation [22]. Thus, it is postulated that the TRPP2 acidic cluster synchronizes phosphorylation, trafficking machinery recruitment, and Ca^{2+} sensing to produce a combinatorial effect of activation-induced translocation of TRPP2 to subcellular compartments [23]. Future work on the TRPA1 acidic cluster targeting the phosphorylatable S1076 residue, coupled with rigorous immunofluorescence with subcellular co-staining and electrophysiology could reveal a groundbreaking mechanism for how TRPA1 trafficking is dynamically regulated. This work could also be expanded to include other pain TRP channels such as TRPV1, which lacks an acidic cluster and is predicted to have distinct desensitization and trafficking mechanisms from TRPA1 (data not shown) [24,25]. This line of questioning goes to the heart of understanding TRP channel function in a physiological context and will be significant for developing treatments for numerous TRP-channel pathologies.

4.2 References

1. Ye, W. et al. Activation Stoichiometry and Pore Architecture of TRPA1 Probed with Channel Concatemers. *Sci Rep* **8**, 17104 (2018).
2. Su, Q. et al. Structure of the human PKD1-PKD2 complex. *Science* **361**(2018).
3. Su, Q. et al. Structural basis for Ca(2+) activation of the heteromeric PKD1L3/PKD2L1 channel. *Nat Commun* **12**, 4871 (2021).
4. Paulsen, C.E., Armache, J.P., Gao, Y., Cheng, Y. & Julius, D. Structure of the TRPA1 ion channel suggests regulatory mechanisms. *Nature* **520**, 511-7 (2015).
5. Suo, Y. et al. Structural Insights into Electrophile Irritant Sensing by the Human TRPA1 Channel. *Neuron* **105**, 882-894 e5 (2020).
6. Zhao, J., Lin King, J.V., Paulsen, C.E., Cheng, Y. & Julius, D. Irritant-evoked activation and calcium modulation of the TRPA1 receptor. *Nature* **585**, 141-145 (2020).
7. Liao, M., Cao, E., Julius, D. & Cheng, Y. Structure of the TRPV1 ion channel determined by electron cryo-microscopy. *Nature* **504**, 107-12 (2013).
8. Cao, E., Liao, M., Cheng, Y. & Julius, D. TRPV1 structures in distinct conformations reveal activation mechanisms. *Nature* **504**, 113-8 (2013).
9. Kremeyer, B. et al. A gain-of-function mutation in TRPA1 causes familial episodic pain syndrome. *Neuron* **66**, 671-80 (2010).
10. Zima, V. et al. Structural modeling and patch-clamp analysis of pain-related mutation TRPA1-N855S reveal inter-subunit salt bridges stabilizing the channel open state. *Neuropharmacology* **93**, 294-307 (2015).
11. Nirenberg, M.J., Chaouni, R., Biller, T.M., Gilbert, R.M. & Paisan-Ruiz, C. A novel TRPA1 variant is associated with carbamazepine-responsive cramp-fasciculation syndrome. *Clin Genet* **93**, 164-168 (2018).
12. Binder, A. et al. Transient receptor potential channel polymorphisms are associated with the somatosensory function in neuropathic pain patients. *PLoS One* **6**, e17387 (2011).
13. Jhun, E.H. et al. Transient receptor potential polymorphism and haplotype associate with crisis pain in sickle cell disease. *Pharmacogenomics* **19**, 401-411 (2018).
14. Uhl, G.R., Walther, D., Behm, F.M. & Rose, J.E. Menthol preference among smokers: association with TRPA1 variants. *Nicotine Tob Res* **13**, 1311-5 (2011).
15. Knaapila, A. et al. Genetic analysis of chemosensory traits in human twins. *Chem Senses* **37**, 869-81 (2012).
16. Deering-Rice, C.E. et al. Activation of Transient Receptor Potential Ankyrin-1 by Insoluble Particulate Material and Association with Asthma. *Am J Respir Cell Mol Biol* **53**, 893-901 (2015).
17. Marchi, M. et al. TRPA1 rare variants in chronic neuropathic and nociplastic pain patients. *Pain* **164**, 2048-2059 (2023).
18. Sura, L. et al. C-terminal acidic cluster is involved in Ca2+-induced regulation of human transient receptor potential ankyrin 1 channel. *J Biol Chem* **287**, 18067-77 (2012).
19. Newcombe, E.A. et al. Insight into Calcium-Binding Motifs of Intrinsically Disordered Proteins. *Biomolecules* **11**(2021).
20. Schmidt, M., Dubin, A.E., Petrus, M.J., Earley, T.J. & Patapoutian, A. Nociceptive signals induce trafficking of TRPA1 to the plasma membrane. *Neuron* **64**, 498-509 (2009).
21. Kottgen, M. et al. Trafficking of TRPP2 by PACS proteins represents a novel mechanism of ion channel regulation. *EMBO J* **24**, 705-16 (2005).
22. Cai, Y. et al. Calcium dependence of polycystin-2 channel activity is modulated by phosphorylation at Ser812. *J Biol Chem* **279**, 19987-95 (2004).
23. Liu, X., Tang, J. & Chen, X.Z. Role of PKD2 in the endoplasmic reticulum calcium homeostasis. *Front Physiol* **13**, 962571 (2022).
24. Sanz-Salvador, L., Andres-Borderia, A., Ferrer-Montiel, A. & Planells-Cases, R. Agonist- and Ca2+-dependent desensitization of TRPV1 channel targets the receptor to lysosomes for degradation. *J Biol Chem* **287**, 19462-71 (2012).
25. Sattler, K. et al. TRPV1 activation and internalization is part of the LPS-induced inflammation in human iPSC-derived cardiomyocytes. *Sci Rep* **11**, 14689 (2021).